

UNIVERSIDADE DE LISBOA
FACULDADE DE CIÊNCIAS
DEPARTAMENTO DE FÍSICA



Study of neuromorphic properties of circuits based on resonant tunneling diodes

Luís Pedro Teixeira das Neves

Mestrado Integrado em Engenharia Física

Dissertação orientada por:
Prof. José Maria Longras Figueiredo (FCUL)
Prof. David Marreiro de Castro Alves (FCUL)

Acknowledgments

First and foremost I would like to thank my parents for always believing in me and investing extensively in my education. A special thanks to my sister is also due for always making sure that above all else, my emotional and psychological well-being were the priority.

This endeavor would not have been possible without the help of my supervisor: professor José Figueiredo, without his help, patience and tools this project wouldn't even have taken off the ground so a big thank you to him as well. Thanks should also go to David Alves for teaching me how to handle and assemble the laboratory apparatus.

Thanks should also go to the Eindhoven University of Technology and the project ChipAI (Energy-efficient and high-bandwidth neuromorphic nanophotonic Chips for Artificial Intelligence systems) funded by the European Commission FETOPEN-2018–2020 program (Grant No. 828841) for providing the RTD devices that were studied in this dissertation.

Finally, I want to thank all of the companions that have walked with me through this path that we call education, without them, this wouldn't have been fun or possible.

Abstract

RTDs, with their negative differential conductance, small size, capability of high frequency of operation and excitable response have the potential to be implemented as basic components in spiking neuromorphic circuits, i.e as nodes that produce and detect spikes.

The present study addresses the neuromorphic properties of resonant tunneling diodes (RTDs), namely their spike generation and detection dynamics. The layout consists firstly on the basic requirements for neuromorphic implementations, followed by a description of the physics behind the RTDs non-linear current voltage characteristic that creates the conditions for spike generation. The mechanisms and conditions by which the RTDs create an excitable response are then put-forward. After this, a series of experimental measurements were carried out for different sized RTDs provided by the ChipAi project. First the measurements of the RTDs I-V curves, followed by a characterisation on their operation as a VCO, concluded with a study on their excitable all-or-nothing response to electrical perturbations. Finally, several experimental activities were carried out to infer the properties and requirements of these devices to work as potential neuromorphic devices. These parameters were the voltage thresholds, resting potentials and refractory times. these were then discussed for all of the different sized RTDs and operation points. On top of this experimental study, tools of simulation were also designed and constructed for these RTDs devices followed by a verification study on not only on their VCO mode but also their neuromorphic properties i.e. excitable response.

It was found that the RTDs can indeed function as spike generators when an appropriate disturbance is applied in their bias voltage. The prospect for the scaling down of these devices to work as nano-neuromorphic devices seems promising due to the fact that smaller RTDs presented higher frequencies of operation leading to shorter periods of oscillation and refractory times. The simulation tool, based on the RLC model of the RTDs, developed using Matlab Simulink/Simscape and the I-V curves of these devices, was able to emulate the oscillatory behaviour of the RTDs when biased in their NDC regions and the neuromorphic property of excitability, again it was found that the scaling down of these devices can lead to faster communication rates.

Key-words: resonant tunneling diode; negative differential resistance; excitability; spiking neural networks; neuromorphic devices

Resumo

Os sistemas de computação de alto desempenho, os sistemas ciber-físicos e de inteligência artificial, suportados por dispositivos exclusivamente eletrônicos apresentam desafios e limitações muito significativas, nomeadamente no que toca à velocidade de processamento de dados, ao consumo de energia e à dissipação térmica. Estas limitações têm levado ao aumento exponencial entre a faculdade de gerar dados/informação e a capacidade de os processar em tempo útil. Os servidores em centros de dados, por exemplo, providenciam computações e lógica em resposta a pedidos de informação enquanto as unidades de armazenamento possuem os ficheiros e dados que são necessários para dar atendimento a esses pedidos. A energia utilizada por estes dispositivos é convertida em energia térmica que, por sua vez, tem de ser retirada dos centros de dados utilizando equipamento de arrefecimento, equipamento este que também necessita de eletricidade para funcionar tornando o processo ainda menos eficiente. Respondendo a estes desafios, as tecnologias neuromórficas procuram imitar aspetos da arquitetura e da dinâmica do cérebro com o objetivo de replicar as suas características funcionais mais marcantes como as capacidades de processamento e integração de estímulos, informações, memória e aprendizagem, mantendo a elevada eficiência energética que caracteriza o cérebro, mas com frequências de operação muito mais elevadas. Sendo a eficiência energética um fator crítico para o futuro das tecnologias de processamento de informação, os processadores neuromórficos apresentam uma plataforma para sistemas de processamento que conseguem superar, em certas tarefas, os computadores atuais de alta performance.

Inspiradas pela estrutura biológica cerebral as redes neuronais artificiais são uma sucessão de neurónios e sinapses interligados entre si, enquanto que na arquitetura de von Neumann, utilizada pela maioria dos computadores atuais, a memória e o processamento ocorrem em locais separados, nos sistemas neuromórficos, tanto quanto se sabe não existe separação entre a memória e processamento. Nos dispositivos neuromórficos a informação encontra-se codificada em sequências de potenciais de ação ("spikes"). Um neurónio, caracterizado por ser um sistema excitável não consome energia exceto no momento de gerar o "spike", isto significa que se for perturbado e essa perturbação não for superior a um certo limiar este não "dispara" um "spike". Se a perturbação for superior ao limiar este dispara um "spike" e de seguida regressa ao seu estado de repouso. Neste campo, merecem particular destaque o desenvolvimento de dispositivos e circuitos neuromórficos baseados em estruturas de efeito de túnel ressonante, nomeadamente díodos de túnel ressonante (RTDs) com características excitáveis, isto é, capazes de reproduzirem esta excitabilidade neuronal. O RTD é um dispositivo de dois terminais que contém um poço quântico de dupla barreira de potencial que cria uma estrutura ressonante que, por sua vez, faz com que a característica corrente-tensão do RTD apresente uma região de condutância diferencial negativa, que se traduz em ganho elétrico. Utilizando esta região de condutância diferencial negativa é possível integrar RTDs em sistemas que possuem propriedades neuromórficas, i.e., excitabilidade. Tirando partido disto e do facto de estes dispositivos terem dimensões reduzidas e altas frequências de operação faz com que os RTDs tenham o potencial de serem implementados como os componentes básicos em processadores neuromórficos à base de "spikes".

O estudo desenvolvido nesta dissertação foca-se nestas propriedades neuromórficas que os RTDs apresentam, nomeadamente as suas dinâmicas de geração de "spikes". Primeiramente, os requisitos básicos para dispositivos neuromórficos são expostos no capítulo 2 seguidos pela apresentação das propriedades que os RTDs devem apresentar tais como o limiar de tensão, os potenciais de repouso e os tempos refratários para poderem ser considerados potenciais neurónios artificiais. No capítulo 3, uma descrição do RTD é exposta, esta contém a física por detrás destes dispositivos, começando pela dupla barreira de poço quântico de potencial e como esta lhes confere uma região de condutância diferencial negativa. Esta região de condutância diferencial negativa traduz-se em ganho elétrico que, quando combinado com elementos indutivos e capacitivos permitem a implementação de sistemas excitáveis e osciladores controlados por tensão na banda da radiofrequência.

No capítulo 4, RTDs providenciados pelo projeto ChipAI de diferentes dimensões que funcionam tanto diretamente como inversamente polarizados, foram caracterizados eletricamente. Caracterização esta que consistiu primeiramente em retirar e estudar as curvas I-V, seguindo-se uma caracterização nas suas regiões de "auto-oscilação" que pode ser considerada um oscilador controlado por tensão onde as amplitudes pico a pico, frequências de oscilação e formas de onda foram retiradas. Ainda neste capítulo apresenta-se o algoritmo de ajuste de curva para a curva I-V. Finalmente uma série de atividades experimentais que foram desenvolvidos para caracterizar a resposta excitável do RTD a uma perturbação, que é possível polarizando os dispositivos perto das suas regiões de condutância diferencial negativa (pico ou vale) e enviando um pulso que perturba esta, fazendo com que, por momentos, este oscile uma única vez produzindo um "spike". O facto de se poder polarizar os RTDs tanto no pico como nos vale inversa ou diretamente indica que existem diversos pontos de funcionamento possíveis para se observar um comportamento semelhante a um dispositivo neuromórfico, os trabalhos referidos abaixo foram efetuados para todos estes pontos de polarização. As características expostas no capítulo 2 foram exploradas para estes RTDs, nomeadamente os limiares em tensão, os potenciais de repouso e os tempos refratários. Finalmente estas foram discutidas e a plausibilidade dos RTDs poderem ser reduzidos em tamanho e ainda assim terem propriedades neuromórficas. O capítulo termina com a apresentação da simulação Matlab que utiliza o modelo RLC de um RTD.

Descobriu-se que o algoritmo de ajuste das curvas I-V experimentais é válido apresentando correntes de pico ligeiramente inferiores às registadas experimentalmente, de resto o comportamento das curvas simuladas concordante com as curvas experimentais. Os resultados obtidos para o oscilador controlado por tensão indicam que RTDs mais pequenos possuem amplitudes de oscilação menores e frequências maiores. Os resultados para os protocolos de comportamento neuromórfico indicam também que circuitos que contêm RTDs possuem de facto propriedades neuromórficas. RTDs mais pequenos apresentam resultados promissores utilizando como pontos de funcionamento os as suas tensões de pico. Os pontos de funcionamento das tensões de vale apresentaram, para todos os RTDs, problemas de estabilidade necessitando de limiares de tensão mais altos. O limiar de tensão das perturbações mostra-se invariante para pulsos com duração superior a 1 ns. Para a tensão de pico como ponto de polarização os RTDs com menor dimensão apresentam tempos refratários, períodos de oscilação e amplitudes pico a pico menores indicando que para estas condições é possível diminuir o tamanho dos dispositivos. No que toca ao modelo criado no Simulink/Simscape este simula as auto-oscilações dos RTDs quando polarizados nas suas regiões de condutância diferencial negativa. Este demonstra também a resposta excitável dos RTDs a uma perturbação na sua tensão de polarização, seja esta a tensão de pico como ponto de funcionamento ou a tensão de vale, podendo esta ser interpretada como um "spike".

Resumindo, os RTDs conseguem de facto funcionar como geradores de "spikes" quando as condições certas lhes são aplicadas, a tensão de pico apesar de ser um ponto de funcionamento com maior consumo

de energia que o vale é mais estável e necessita de perturbações com menor amplitude. A amplitude e período dos "spikes" relacionam-se com as características das ondas geradas pela oscilação dos RTDs quando polarizados nas suas regiões de condutância diferencial negativa. As características das ondas geradas nesta região encontram-se por sua vez relacionadas com as características das curvas I-V tal como as razões das correntes de pico/vale que indicam a amplitude da oscilação. Os protocolos desenvolvidos no capítulo dos métodos são uma referência para a utilização destes dispositivos como geradores de "spike" excitáveis, utilizando o estudo das tensões de polarização é possível adaptar os RTDs para produzirem "spikes", o utilizador necessita de escolher a amplitude do limiar de tensão e a duração da perturbação e obtém a tensão a que se deve polarizar os RTDs para estes produzirem "spikes".

Palavras-chave: díodo de túnel ressonante; resistência diferencial negativa; excitabilidade; redes neuronais de spikes; dispositivos neuromórficos

Contents

List of Figures	xi
List of Tables	xix
1 Introduction	1
1.1 Context and Motivation	1
1.2 Objectives and Tools Used	2
1.3 Dissertation Overview	2
2 Introduction to Neuromorphic Devices	5
2.1 Neuromorphic Devices	5
2.1.1 Neurons	5
2.1.2 Spiking Neural Networks	7
2.1.3 Information Representation in the Brain	8
3 Resonant Tunneling Diode	11
3.1 Resonant Tunneling Diode	11
3.2 Double Barrier Quantum Well	11
3.3 Current Voltage Characteristic	14
3.4 RTD Model	16
3.5 RTD Excitable Response	19
4 Methods	21
4.1 Characterization of the RTDs	21
4.1.1 RTD samples	21
4.1.2 Electrical Characterization of the Devices	23
4.1.2.1 Experimental Setup	23
4.1.3 Curve Fitting Software for the characterization of the RTDs	25
4.1.4 Voltage Controlled Oscillator	25
4.1.4.1 Experimental Setup	25
4.2 Spiking using RTDs	26
4.2.1 Experimental Setup	27
4.2.2 Generated Spikes Analysis	28
4.2.3 Voltage Threshold	29
4.2.4 Bias Voltage Analysis	30
4.2.5 Refractory Time	30
4.3 Simulation using MatLab's Simulink and Simscape	31

CONTENTS

- 5 Results and Discussion 35**
 - 5.1 Characterization of the Devices 35
 - 5.1.1 Curve Fitting Software for the Characterization of the RTDs 39
 - 5.2 Voltage Controlled Oscillator 43
 - 5.2.1 Oscillation Waveforms 43
 - 5.2.2 Frequency Analysis 43
 - 5.2.3 Peak to Peak Amplitude Analysis 45
 - 5.3 Spiking 47
 - 5.3.1 Generated Spike Characteristics 47
 - 5.3.1.1 Elapsed Time 50
 - 5.3.2 Voltage Threshold 51
 - 5.3.3 Influence of the Bias Points on the Generated Spike 54
 - 5.3.4 Bias Voltage Analysis 56
 - 5.3.5 Refractory Time 59
 - 5.4 Simulation using MatLab’s Simulink/Simscape 62
 - 5.4.1 I-V Characteristics 63
 - 5.4.2 Simulation Parameters 65
 - 5.4.3 Waveforms 66
 - 5.4.4 Excitability 74
- 6 Conclusions and Future Work 79**
- Bibliography 81**
- A Curve Fitting Results Plots 83**
- B Curve Fitting Model Peak and Valley Currents and Voltages 89**
- C VCO Waveforms 91**
- D Spiking 95**

List of Figures

2.1	Diagram of a biological neuron. Adapted from: (Biological Neuron Diagram)	5
2.2	Internal state of a post synaptic neuron (spike), and some of its characteristics such as: resting potential, action potential and refractory period. Adapted from: (Ghosh-Dastidar and Adeli (2009))	6
2.3	Illustration of the all-or-none law/principle Adapted from: (All-or-none law)	6
2.4	Four major spiking modes Adapted from: (Zhu et al. (2020))	7
2.5	Schematic representation of a FCN. Adapted from (Bouvier et al. (2019))	8
3.1	Schematic of a RTD with InGaAs in the well, AlAs as the barriers (red) and a InP substrate. The emitter and the collector contact layers are displayed in yellow.	11
3.2	Illustration of the hetero-structure and energy-band diagrams for an InGaAs/AlAs DBQW. Resonant energy levels E_1 and E_2 are also shown.	11
3.3	Schematic of the conduction band profile for a generic DBQW. E_B designates the energy of the potential barrier, E_R the energy of the resonant level and Γ the resonance width. Adapted from: (Ironsides et al. (2009))	12
3.4	Band diagram of a DBQW heterostructure under an applied bias (A) with the corresponding transmission probability (B). The electron distribution before and after crossing the DBQW is also presented. Adapted from: (DBQW under bias)	12
3.5	Conduction band profiles for different bias voltages. (a) $V = 0$; (b) $V = V_{Peak}$; (c) $V = V_{Valley}$. (d) Schematic of the current voltage characteristic. Adapted from: (Ironsides et al. (2009))	13
3.6	Current transport mechanisms in the DBQW RTD. a) Resonant tunneling; b) Tunneling through higher levels; c) Thermionic emission; d) Field assisted tunneling; e) tunneling through evanescent states; f) inelastic tunneling; g) leakage current. Adapted from: (Current transport mechanisms)	14
3.7	Current density as a function of voltage in an RTD (Blue); Conductance as a function of the voltage (Orange). Parameters used: $A = 1.4 \times 10^4 \text{ A} \cdot \text{cm}^{-2}$; $B = 0.0461 \text{ V}$; $C = 0.1417 \text{ V}$; $D = 0.0373 \text{ V}$; $H = 0.04803 \text{ A} \cdot \text{cm}^{-2}$; $n_1 = 0.1325$; $n_2 = 0.1346$	16
3.8	Basic AC signal equivalent circuit for a RTD, R and L represent the parasitic components and C and $F(V) = M \cdot J(V)$ a voltage dependent current source. Adapted from (Ironsides et al. (2009))	17
3.9	Orbit of the oscillation in the current voltage characteristic for a high $\sqrt{\frac{C}{L}} (\sim 1)$. Adapted from (Ortega-Piwonka et al. (2021))	18
3.10	Corresponding waveform for a high $\sqrt{\frac{C}{L}} (\sim 1)$. Adapted from (Ortega-Piwonka et al. (2021))	18

LIST OF FIGURES

3.11	Orbit of the oscillation in the current voltage characteristic for a low $\sqrt{\frac{C}{L}}$ (0.001). Adapted from (Ortega-Piwonka et al. (2021))	18
3.12	Corresponding waveform for a low $\sqrt{\frac{C}{L}}$ (0.001). Adapted from (Ortega-Piwonka et al. (2021))	18
3.13	System response to several perturbations out of its natural equilibrium parameters. Adapted from (Ortega-Piwonka et al. (2021))	19
4.1	Epilayers structure of the RTDs provided by the ChipAi project.	22
4.2	One element RTD illustration.	22
4.3	RTDs under the microscope.	22
4.4	I-V characteristics provided by the ChipAi project in forward and reverse bias for the 4.5 μm , 5 μm , 5.5 μm radius RTDs.	23
4.5	Schematic of the experimental setup used to measure the I-V characteristic of the RTDs.	24
4.6	Experimental setup used in this dissertation.	24
4.7	Experimental setup used to characterize the oscillating region of the RTDs.	26
4.8	Concept behind spike generation using the non-linear nature of the current voltage characteristic of the RTDs in the forward bias.	27
4.9	Concept behind spike generation using the non-linear nature of the current voltage characteristic of the RTDs in the reverse bias.	27
4.10	Experimental setup used to study the spiking properties of the RTDs.	27
4.11	Illustration of the measured variables in the oscilloscope: the reaction time and the spike period and peak to peak amplitude.	28
4.12	System being perturbed by a pulse with an amplitude bellow the voltage threshold. No spike is generated.	29
4.13	System being pertubed by a pulse with an amplitude hgher than the voltage threshold of the bias point. A spike is produced.	29
4.14	Illustration of how increasing the bias voltage can cause the RTD to produce a spike.	30
4.15	Illustration of the response of the system when the disturbance pulses are too close together (bellow the refractory time).	31
4.16	Illustration of the response of the system when the two disturbance pulses are temporally far enough to each one spikes individually.	31
4.17	Parameters than can be changed in the pulse generator.	32
4.18	Simulink/Simscape simulation of the basic equivalent circuit for a DC biased RTD.	33
5.1	Current voltage characteristic print taken form the sourcemeter for the 4.5 μm radius RTD under reverse bias.	35
5.2	Current voltage characteristics for the six RTD under a forward voltage bias with a 0 to 2V sweep.	36
5.3	Current voltage characteristics for the six RTD under a forward voltage bias with a 2 to 0V sweep.	36
5.4	Current voltage characteristics for the six RTD under a reverse voltage bias with a 0 to -2V sweep.	36
5.5	Current voltage characteristics for the six RTD under a reverse voltage bias with a -2 to 0V sweep.	36
5.6	Density of current as a function of the bias voltage for all of the RTDs in the ascend.	38

LIST OF FIGURES

5.7 Density of current as a function of the bias voltage for all of the RTDs in the descend. . . 38

5.8 Density of current as a function of the bias voltage for all of the RTDs in the ascend. . . 39

5.9 Density of current as a function of the bias voltage for all of the RTDs in the descend. . . 39

5.10 Plot of the experimental data and curve fit of the 4.5 μm radius RTD current voltage curve when forward bias is applied in the ascend. The curve fitting coefficients are: $A = 1.159 \times 10^4 \text{ A} \cdot \text{cm}^{-2}$, $B = 0.04978 \text{ V}$, $C = 0.1362 \text{ V}$, $D = 0.004599 \text{ V}$, $H = 2.949 \text{ A} \cdot \text{cm}^{-2}$, $n_1 = 0.1303$, $n_2 = 0.1224$ 39

5.11 Plot of the experimental data and curve fit of the 4.5 μm radius RTD current voltage curve when a forward bias is applied in the descend. The curve fitting coefficients are: $A = 1.216 \times 10^4 \text{ A} \cdot \text{cm}^{-2}$, $B = 0.04459 \text{ V}$, $C = 0.1327 \text{ V}$, $D = 0.003917 \text{ V}$, $H = 5.205 \text{ A} \cdot \text{cm}^{-2}$, $n_1 = 0.1302$, $n_2 = 0.115$ 39

5.12 Plot of the experimental data and curve fit of the 4.5 μm radius RTD current voltage curve when a reverse bias is applied in the ascend. The curve fitting coefficients are: $A = 1.281 \times 10^4 \text{ A} \cdot \text{cm}^{-2}$, $B = 0.04576 \text{ V}$, $C = 0.1425 \text{ V}$, $D = 0.003802 \text{ V}$, $H = 0.5193 \text{ A} \cdot \text{cm}^{-2}$, $n_1 = 0.1289$, $n_2 = 0.1324$ 40

5.13 Plot of the experimental data and curve fit of the 4.5 μm radius RTD current voltage curve when a reverse bias is applied in the descend. The curve fitting coefficients are: $A = 1.34 \times 10^4 \text{ A} \cdot \text{cm}^{-2}$, $B = 0.04303 \text{ V}$, $C = 0.1396 \text{ V}$, $D = 0.003635 \text{ V}$, $H = 0.5685 \text{ A} \cdot \text{cm}^{-2}$, $n_1 = 0.265$, $n_2 = 0.1313$ 40

5.14 Density of current as a function of the bias voltage (forward) for all of the RTDs in the ascend. 41

5.15 Curve fitting curves obtained for all of the RTDs for an increasing forward bias voltage. . 41

5.16 Density of current as a function of the bias voltage (reverse) for all of the RTDs in the ascend. 41

5.17 Curve fitting curves obtained for all of the RTDs for an increasing reverse bias voltage. . 41

5.18 Density of current as a function of the bias voltage (forward) for all of the RTDs in the descend. 42

5.19 Curve fitting curves obtained for all of the RTDs for a decreasing forward bias voltage. . 42

5.20 Density of current as a function of the bias voltage (reverse) for all of the RTDs in the descend. 42

5.21 Curve fitting curves obtained for all of the RTDs for a decreasing reverse bias voltage. . . 42

5.22 Frequency of oscillation of the RTDs as a function of the applied voltage in the ascend under a forward bias. 44

5.23 Frequency of oscillation of the RTDs as a function of the applied voltage in the descend under a forward bias. 44

5.24 Waveform of the 5.5 μm RTD in the descend. 44

5.25 Frequency of oscillation of the RTDs as a function of the applied voltage in the ascend under a reverse bias. 45

5.26 Frequency of oscillation of the RTDs as a function of the applied voltage in the descend under a reverse bias. 45

5.27 Peak to peak amplitude of oscillation of the RTDs as a function of the applied voltage in the ascend under a forward bias. 46

5.28 Peak to peak amplitude of oscillation of the RTDs as a function of the applied voltage in the descend under a forward bias. 46

LIST OF FIGURES

5.29	Peak to peak amplitude of oscillation of the RTDs as a function of the applied voltage in the ascend under a reverse bias. P2P vs Voltage reverse bias ascend.	46
5.30	Peak to peak amplitude of oscillation of the RTDs as a function of the applied voltage in the descend under a reverse bias.	46
5.31	Waveform of the spike generated by the 2.5 μm RTD.	47
5.32	Waveform of the spike generated by the 2.5 μm RTD.	48
5.33	Experimental setup used to study the spiking properties of the RTDs with the lengths of the cables that are connecting the components	50
5.34	Response of the system to a pulse disturbance under its voltage threshold. The pulse width is 1 ns and its amplitude is 64 mV. The DC bias voltage applied was 0.96 V.	51
5.35	Response of the system to a pulse disturbance over its voltage threshold. The pulse width is 1 ns and its amplitude is 65 mV. The DC bias voltage applied was 0.96 mV.	52
5.36	Oscilloscope trace for the generated spike of the 4.5 μm RTD, when disturbed in its forward peak voltage. The bias voltage was of 0.96 V and the pulse amplitude was of 75 mV and 1 ns width.	55
5.37	Oscilloscope trace for the generated spike of the 4.5 μm RTD, when disturbed in its forward valley voltage. The bias voltage was of 1.43 V and the pulse amplitude was of -350 mV and 1 ns width.	55
5.38	Response of the 4.5 μm RTD to a 100mV pulse with 1 ns of width. The bias voltage applied was $V_{DC} = 0.9$ V.	56
5.39	Response of the system to the same disturbance (100mV pulse with 1 ns of width) but with a higher bias voltage of $V_{DC} = 0.911$ V.	57
5.40	Minimum Bias voltage to be applied to the forward bias (peak) RTD as a function of the pulse width. The pulse amplitude used was of 50 mV.	57
5.41	Minimum Bias voltage to be applied to the reverse bias (peak) RTD as a function of the pulse width. The pulse amplitude used was of -50 mV. Only the absolute value of the bias voltage was considered for the plots for an easier analysis.	57
5.42	Minimum Bias voltage to be applied to the forward bias (peak) RTD as a function of the pulse width. The pulse amplitude used was of 100 mV.	58
5.43	Minimum Bias voltage to be applied to the reverse bias (peak) RTD as a function of the pulse width. The pulse amplitude used was of -100 mV. Only the absolute value of the bias voltage was considered for the plots for an easier analysis.	58
5.44	Minimum Bias voltage to be applied to the forward bias (valley) RTD as a function of the pulse width. The pulse amplitude used was of -350 mV.	59
5.45	Minimum Bias voltage to be applied to the forward bias (valley) RTD as a function of the pulse width. The pulse amplitude used was of 350 mV. Only the absolute value of the bias voltage was considered for the plots for an easier analysis.	59
5.46	Oscilloscope trace for the 2.5 μm RTD responding to two pulses (50 mV) separated by 2 ns. The RTD was biased in its positive peak voltage.	61
5.47	Oscilloscope trace for the 5.5 μm RTD responding to two pulses (50 mV) separated by 13 ns. The RTD was biased in its positive peak voltage.	61
5.48	Oscilloscope trace for the 4.5 μm RTD responding to two pulses (-350 mV) separated by 6 ns. The RTD was biased in its positive peak voltage.	62
5.49	I-V curve of the 2.5 μm RTD in the ascend with load line at $V_{DC} = 0.95$ V.	63
5.50	I-V curve of the 3.5 μm RTD in the ascend with load line at $V_{DC} = 0.97$ V.	63

LIST OF FIGURES

5.51	I-V curve of the 4 μm RTD in the ascend with load line at $V_{DC} = 1.03$ and $R = 1 \Omega$	64
5.52	I-V curve of the 4.5 μm RTD in the ascend with load line at $V_{DC} = 1.07$ and $R = 1 \Omega$. . .	64
5.53	I-V curve of the 5 μm RTD in the ascend with load line at $V_{DC} = 1.1$ and $R = 1 \Omega$	65
5.54	I-V curve of the 5.5 μm RTD in the ascend with load line at $V_{DC} = 1.13$ and $R = 1 \Omega$. . .	65
5.55	Voltage across the 2.5 μm radius RTD for a bias voltage of $V_{DC} = 0.95$ V.	67
5.56	Current going though the resistor and the inductor for a bias voltage of $V_{DC} = 0.95$ V. The current across the capacitor is also presented. This figure is concerning the 2.5 μm radius RTD.	67
5.57	Spectrum analyser result for the simulation presented above of the 2.5 μm RTD.	67
5.58	Voltage across the 3.5 μm radius RTD for a bias voltage of $V_{DC} = 0.97$ V.	68
5.59	Current going though the resistor and the inductor for a bias voltage of $V_{DC} = 0.97$ V. the current going through the capacitor is also presented. This figure is concerning the 3.5 μm radius	68
5.60	Spectrum analyser result for the simulation presented above of the 3.5 μm RTD.	69
5.61	Voltage across the 4 μm radius RTD for a bias voltage of $V_{DC} = 1.03$ V.	69
5.62	Current going though the resistor and the inductor for a bias voltage of $V_{DC} = 1.03$ V. the current going through the capacitor is also presented. This figure is concerning the 4 μm radius	69
5.63	Spectrum analyser result for the simulation presented above of the 4 μm RTD.	70
5.64	Voltage across the 4.5 μm radius RTD for a bias voltage of $V_{DC} = 1.07$ V.	70
5.65	Current going though the resistor and the inductor for a bias voltage of $V_{DC} = 1.07$ V. the current going through the capacitor is also presented. This figure is concerning the 4.5 μm radius	70
5.66	Spectrum analyser result for the simulation presented above of the 4.5 μm RTD.	71
5.67	Voltage across the 5 μm radius RTD for a bias voltage of $V_{DC} = 1.1$ V.	72
5.68	Current going though the resistor and the inductor for a bias voltage of $V_{DC} = 1.1$ V. the current going through the capacitor is also presented. This figure is concerning the 5 μm radius	72
5.69	Spectrum analyser result for the simulation presented above of the 5 μm RTD.	72
5.70	Voltage across the 5.5 μm RTD for a bias voltage of $V_{DC} = 1.13$ V.	73
5.71	Current going though the resistor and the inductor for a bias voltage of $V_{DC} = 1.13$ V. the current going through the capacitor is also presented. This figure is concerning the 5.5 μm radius	73
5.72	Spectrum analyser result for the simulation presented above of the 5.5 μm RTD.	74
5.73	Voltage across the RTD for a sub-threshold disturbance in its peak.	75
5.74	Voltage across the RTD for disturbance above its treshold in its peak.	75
5.75	I-V curve of the 2.5 μm RTD used to study the excitable response of the device when disturbing it with a negative pulse in its the valley voltage.	76
5.76	Voltage across the RTD for disturbance above its treshold in its valley.	77
A.1	Plot of the experimental data and curve fit of the 2.5 μm radius RTD current voltage curve when increasing forward bias is applied. The curve fitting coefficients are: $A = 1.187 \times$ $10^4 \text{ A} \cdot \text{cm}^{-2}$; $B = 0.04337 \text{ V}$; $C = 0.1418 \text{ V}$; $D = 0.004704 \text{ V}$; $H = 4.263 \text{ A} \cdot \text{cm}^{-2}$; $n_1 = 0.1515$; $n_2 = 0.1168$	83

LIST OF FIGURES

A.2	Plot of the experimental data and curve fit of the 2.5 μm radius RTD current voltage curve when decreasing forward bias is applied. The curve fitting coefficients are: $A = 1.161 \times 10^4 \text{ A} \cdot \text{cm}^{-2}$; $B = 0.04263 \text{ V}$; $C = 0.1419 \text{ V}$; $D = 0.005081 \text{ V}$; $H = 3.514 \text{ A} \cdot \text{cm}^{-2}$; $n_1 = 0.155$; $n_2 = 0.1193$	83
A.3	Plot of the experimental data and curve fit of the 2.5 μm radius RTD current voltage curve when increasing reverse bias is applied. The curve fitting coefficients are: $A = 1.538 \times 10^4 \text{ A} \cdot \text{cm}^{-2}$; $B = 0.03642 \text{ V}$; $C = 0.1492 \text{ V}$; $D = 0.00506 \text{ V}$; $H = 0.1277 \text{ A} \cdot \text{cm}^{-2}$; $n_1 = 0.15$; $n_2 = 0.1478$	84
A.4	Plot of the experimental data and curve fit of the 2.5 μm radius RTD current voltage curve when decreasing reverse bias is applied. The curve fitting coefficients are: $A = 1.557 \times 10^4 \text{ A} \cdot \text{cm}^{-2}$; $B = 0.03334 \text{ V}$; $C = 0.1461 \text{ V}$; $D = 0.005011 \text{ V}$; $H = 0.05918 \text{ A} \cdot \text{cm}^{-2}$; $n_1 = 0.1495$; $n_2 = 0.1583$	84
A.5	Plot of the experimental data and curve fit of the 3.5 μm radius RTD current voltage curve when increasing forward bias is applied. The curve fitting coefficients are: $A = 1.309 \times 10^4 \text{ A} \cdot \text{cm}^{-2}$; $B = 0.04106 \text{ V}$; $C = 0.1382 \text{ V}$; $D = 0.004566 \text{ V}$; $H = 5.209 \text{ A} \cdot \text{cm}^{-2}$; $n_1 = 0.1448$; $n_2 = 1154$	84
A.6	Plot of the experimental data and curve fit of the 3.5 μm radius RTD current voltage curve when decreasing forward bias is applied. The curve fitting coefficients are: $A = 1.284 \times 10^4 \text{ A} \cdot \text{cm}^{-2}$; $B = 0.04379 \text{ V}$; $C = 0.1412 \text{ V}$; $D = 0.005513 \text{ V}$; $H = 3.264 \text{ A} \cdot \text{cm}^{-2}$; $n_1 = 0.1471$; $n_2 = 0.1214$	84
A.7	Plot of the experimental data and curve fit of the 3.5 μm radius RTD current voltage curve when increasing reverse bias is applied. The curve fitting coefficients are: $A = 1.133 \times 10^4 \text{ A} \cdot \text{cm}^{-2}$; $B = 0.04902 \text{ V}$; $C = 0.1491 \text{ V}$; $D = 0.003558 \text{ V}$; $H = 1.675 \text{ A} \cdot \text{cm}^{-2}$; $n_1 = 0.1406$; $n_2 = 0.116$	85
A.8	Plot of the experimental data and curve fit of the 3.5 μm radius RTD current voltage curve when decreasing reverse bias is applied. The curve fitting coefficients are: $A = 1.326 \times 10^4 \text{ A} \cdot \text{cm}^{-2}$; $B = 0.04122 \text{ V}$; $C = 0.1425 \text{ V}$; $D = 0.003583 \text{ V}$; $H = 0.9916 \text{ A} \cdot \text{cm}^{-2}$; $n_1 = 0.1344$; $n_2 = 0.1229$	85
A.9	Plot of the experimental data and curve fit of the 4 μm radius RTD current voltage curve when increasing forward bias is applied. The curve fitting coefficients are: $A = 1.171 \times 10^4 \text{ A} \cdot \text{cm}^{-2}$; $B = 0.04873 \text{ V}$; $C = 0.1369 \text{ V}$; $D = 0.003928 \text{ V}$; $H = 4.548 \text{ A} \cdot \text{cm}^{-2}$; $n_1 = 0.1343$; $n_2 = 0.1171$	85
A.10	Plot of the experimental data and curve fit of the 4 μm radius RTD current voltage curve when decreasing forward bias is applied. The curve fitting coefficients are: $A = 1.267 \times 10^4 \text{ A} \cdot \text{cm}^{-2}$; $B = 0.04209 \text{ V}$; $C = 0.1387 \text{ V}$; $D = 0.005668 \text{ V}$; $H = 2.296 \text{ A} \cdot \text{cm}^{-2}$; $n_1 = 0.1447$; $n_2 = 0.1257$	85
A.11	Plot of the experimental data and curve fit of the 4 μm radius RTD current voltage curve when increasing reverse bias is applied. The curve fitting coefficients are: $A = 1.395 \times 10^4 \text{ A} \cdot \text{cm}^{-2}$; $B = 0.04061 \text{ V}$; $C = 0.1417 \text{ V}$; $D = 0.00373 \text{ V}$; $H = 0.4804 \text{ A} \cdot \text{cm}^{-2}$; $n_1 = 0.1329$; $n_2 = 0.1331$	86
A.12	Plot of the experimental data and curve fit of the 4 μm radius RTD current voltage curve when decreasing reverse bias is applied. The curve fitting coefficients are: $A = 1.398 \times 10^4 \text{ A} \cdot \text{cm}^{-2}$; $B = 0.04068 \text{ V}$; $C = 0.1415 \text{ V}$; $D = 0.003798 \text{ V}$; $H = 0.4274 \text{ A} \cdot \text{cm}^{-2}$; $n_1 = 0.1325$; $n_2 = 0.1346$	86

LIST OF FIGURES

A.13 Plot of the experimental data and curve fit of the 5 μm radius RTD current voltage curve when increasing forward bias is applied. The curve fitting coefficients are: $A = 1.323 \times 10^4 \text{ A} \cdot \text{cm}^{-2}$; $B = 0.04193 \text{ V}$; $C = 1281 \text{ V}$; $D = 0.004248 \text{ V}$; $H = 2.297 \text{ A} \cdot \text{cm}^{-2}$; $n_1 = 0.12$; $n_2 = 0.122$ 86

A.14 Plot of the experimental data and curve fit of the 5 μm radius RTD current voltage curve when decreasing forward bias is applied. The curve fitting coefficients are: $A = 1.165 \times 10^4 \text{ A} \cdot \text{cm}^{-2}$; $B = 0.04776 \text{ V}$; $C = 0.1322 \text{ V}$; $D = 0.004076 \text{ V}$; $H = 4.577 \text{ A} \cdot \text{cm}^{-2}$; $n_1 = 0.1244$; $n_2 = 0.1163$ 86

A.15 Plot of the experimental data and curve fit of the 5 μm radius RTD current voltage curve when increasing reverse bias is applied. The curve fitting coefficients are: $A = 1.437 \times 10^4 \text{ A} \cdot \text{cm}^{-2}$; $B = 0.04014 \text{ V}$; $C = 0.1351 \text{ V}$; $D = 0.003739 \text{ V}$; $H = 0.2883 \text{ A} \cdot \text{cm}^{-2}$; $n_1 = 0.118$; $n_2 = 0.1395$ 87

A.16 Plot of the experimental data and curve fit of the 5 μm radius RTD current voltage curve when decreasing reverse bias is applied. The curve fitting coefficients are: $A = 1.384 \times 10^4 \text{ A} \cdot \text{cm}^{-2}$; $B = 0.041 \text{ V}$; $C = 0.1351 \text{ V}$; $D = 0.003463 \text{ V}$; $H = 0.5037 \text{ A} \cdot \text{cm}^{-2}$; $n_1 = 0.1187$; $n_2 = 0.1326$ 87

A.17 Plot of the experimental data and curve fit of the 5.5 μm radius RTD current voltage curve when increasing forward bias is applied. The curve fitting coefficients are: $A = 1.238 \times 10^4 \text{ A} \cdot \text{cm}^{-2}$; $B = 0.04457 \text{ V}$; $C = 0.1278 \text{ V}$; $D = 0.004241 \text{ V}$; $H = 4.081 \text{ A} \cdot \text{cm}^{-2}$; $n_1 = 0.1164$; $n_2 = 0.117$ 87

A.18 Plot of the experimental data and curve fit of the 5.5 μm radius RTD current voltage curve when decreasing forward bias is applied. The curve fitting coefficients are: $A = 1.228 \times 10^4 \text{ A} \cdot \text{cm}^{-2}$; $B = 0.04459 \text{ V}$; $C = 0.1283 \text{ V}$; $D = 0.004258 \text{ V}$; $H = 3.968 \text{ A} \cdot \text{cm}^{-2}$; $n_1 = 0.1176$; $n_2 = 0.1175$ 87

A.19 Plot of the experimental data and curve fit of the 5.5 μm radius RTD current voltage curve when increasing reverse bias is applied. The curve fitting coefficients are: $A = 1.438 \times 10^4 \text{ A} \cdot \text{cm}^{-2}$; $B = 0.0389 \text{ V}$; $C = 0.1311 \text{ V}$; $D = 0.003384 \text{ V}$; $H = 0.6433 \text{ A} \cdot \text{cm}^{-2}$; $n_1 = 0.112$; $n_2 = 0.129$ 88

A.20 Plot of the experimental data and curve fit of the 5.5 μm radius RTD current voltage curve when decreasing reverse bias is applied. The curve fitting coefficients are: $A = 1.467 \times 10^4 \text{ A} \cdot \text{cm}^{-2}$; $B = 0.03721 \text{ V}$; $C = 0.1297 \text{ V}$; $D = 0.003309 \text{ V}$; $H = 0.5417 \text{ A} \cdot \text{cm}^{-2}$; $n_1 = 0.1114$; $n_2 = 0.1314$ 88

C.1 Waveform of the 2.5 μm RTD under a 0.96 V bias voltage. 91

C.2 Waveform of the 3.5 μm RTD under a 0.96 V bias voltage. 92

C.3 Waveform of the 4 μm RTD under a 1.04 V bias voltage. 92

C.4 Waveform of the 4.5 μm RTD under a 1.12 V bias voltage. 93

C.5 Waveform of the 5 μm RTD under a 1.13 V bias voltage. 93

C.6 Waveform of the 5.5 μm RTD under a 1.19 V bias voltage. 94

D.1 Oscilloscope trace for the generated spike of the 4.5 μm RTD, when disturbed in its reverse peak voltage. The bias voltage was of -1.028 V and the pulse amplitude was of -75 mV and 1 ns width. 95

LIST OF FIGURES

D.2 Oscilloscope trace for the generated spike of the $4.5\ \mu\text{m}$ RTD, when disturbed in its reverse valley voltage. The bias voltage was of $-1.52\ \text{V}$ and the pulse amplitude was of $350\ \text{mV}$ and $1\ \text{ns}$ width.	96
---	----

List of Tables

5.1	Peak/valley currents and voltages expressed in mA for each of the RTD's with a forward bias and respective ratio's in the ascend.	37
5.2	Peak/valley currents and voltages for each of the RTD's with a reverse bias and respective ratio's in the ascend.	37
5.3	Peak/valley currents and voltages for each of the RTD's with a forward bias and respective ratio's in the descend.	37
5.4	Peak/valley currents and voltages for each of the RTDs with a reverse bias and respective ratio's in the descend.	38
5.5	Spike analysis of the RTDs in the forward peak bias voltage. The reaction time corresponds to the elapsed time between the pulse and the generated spike. The spike period and peak to peak amplitude are the spike characteristics. These values are all for pulses with 1 ns of width and 75 mV of amplitude.	48
5.6	Temporal analysis of the RTDs in the reverse peak bias voltage. The reaction time corresponds to the elapsed time between the pulse and the generated spike. The spike wavelength and peak to peak amplitude are the spike characteristics. These values are all for pulses with 1 ns of width and -75 mV of amplitude.	49
5.7	Temporal analysis of the RTDs in the forward valley bias voltage. The reaction time corresponds to the elapsed time between the pulse and the generated spike. The spike wavelength and peak to peak amplitude are the spike characteristics. These values are all for pulses with 1 ns of width and -350 mV of amplitude.	49
5.8	Temporal analysis of the RTDs in the reverse bias voltage. The reaction time corresponds to the elapsed time between the pulse and the generated spike. The spike wavelength and peak to peak amplitude are the spike characteristics. These values are all for pulses with 1 ns of width and 350 mV of amplitude.	49
5.9	Corresponding cables lengths of the numbers presented in figure 5.33.	50
5.10	Voltage threshold of the RTDs. V_{Peak} represents the peak voltage defined in 5.1 and the bias voltage the actual voltage that was applied to the devices.	52
5.11	Voltage threshold of the RTDs. V_{Peak} represents the peak voltage defined in 5.2 and the bias voltage the actual voltage that was applied to the devices.	52
5.12	Voltage threshold of the RTDs. V_{Valley} represents the peak voltage defined in 5.3 and the bias voltage the actual voltage that was applied to the devices.	53
5.13	Voltage threshold of the RTDs. V_{Valley} represents the peak voltage defined in 5.4 and the bias voltage the actual voltage that was applied to the devices.	53
5.14	Refractory Times and respective peak bias voltages off all the RTDs, for pulses with 50 mV and 100 mV of amplitude. The pulse width was of 1 ns.	60

5.15	Refractory Times and respective peak bias voltages off all the RTDs, for pulses with -50 mV and -100 mV of amplitude. The pulse width was of 1 ns.	60
5.16	Refractory Times and respective valley bias voltages off all the RTDs, for pulses with ± 350 mV of amplitude. The pulse width was of 1 ns.	60
5.17	Orbit points (voltage and current) for the 2.5 and 3.5 μm RTDs.	63
5.18	Orbit points (voltage and current) for the 4 and 4.5 μm RTDs.	64
5.19	Orbit points (voltage and current) for the 5 and 5.5 μm RTDs.	65
5.20	Simulation parameters that remained constant for all of the RTDs.	65
5.21	Simulation parameters for the 2.5 μm , 3.5 μm and 4 μm RTD.	66
5.22	Simulation parameters for the 4.5 μm , 5 μm and 5.5 μm RTD.	66
5.23	Simulation parameters for the 2.5 μm RTD in the descending direction current voltage characteristic.	76
5.24	Orbit points (voltage and current) of the descending I-V characteristic of the 2.5 μm RTD.	77
B.1	Peak/valley currents and voltages obtained for each of the RTDs for the I-V curve obtained via curve fitting algorithm.	90

Acronyms

ANNs Artificial Neural Networks. 5, 7

AWFG Arbitrary Wave Function Generator. 24, 26–28, 30, 31

CMOS Complementary metal-oxide semiconductor. 8

CPW Co-planar Waveguide. 23

DBQW Double Barrier Quantum Well. xi, 1, 11, 12, 14, 19, 21, 44

FCN Fully Connected Network. xi, 7, 8

GSG Ground Signal Ground. 23

NDC Negative Differential Conductance. 2, 13–15, 17–19, 21, 23–27, 29, 32, 35–37, 40, 45, 49, 53–56, 58, 59, 62–64, 74, 79

NNs Neural Networks. 5

PDC Positive Differential Conductance. 13, 17–19, 35–37, 40, 53–55, 74

PSP Post-synaptic Potential. 7, 8

PVCR Peak to Valley Current Ratio. 16, 37, 38, 46, 90

RTD Resonant Tunneling Diode. ix–xx, 1, 2, 11–19, 21–33, 35–77, 79, 83–88, 90–96

VCO Voltage Controlled Oscillator. x, 17, 25, 49, 50, 53, 58, 91

Symbols

e	Elementary Charge
k_B	Boltzmann Constant
T	Absolute Temperature
V	Voltage
I	Current
G	Electrical Conductance
J	Current Density
m^*	Electron Effective Mass
\hbar	Reduced Plank Constant
Γ	Resonance Width
H	Saturation Current
f	Frequency
π	Pi
R	Resistance
L	Inductance
C	Capacitance
f	Frequency
InGaAs	Indium Gallium Arsenide
AlAs	Aluminium Arsenide
InP	Indium Phosphide

Chapter 1

Introduction

1.1 Context and Motivation

Most computers nowadays are based on the von Neumann architecture that is composed by a processing unit, a control unit, a memory, an external mass storage and the corresponding input and output mechanisms. The central processing unit is separate from the memory so the instructions that are executed by the processing unit need to be brought from the memory. This implies that an instruction fetch and a data operation cannot occur at the same time, this is referred to as the von Neumann bottleneck.

Biological systems rely on non-deterministic operation with massive parallelism of conceptually simple processing units called neurons, that with their dynamically changing synapses are the fundamental blocks of neuromorphic systems (Nawrocki et al. (2016)). Compared with conventional supercomputers that consume megawatts of power and take minutes, hours, or longer to carry out complex, nonlinear, and non-sequential calculations such as image/pattern recognition, the human brain consumes around 25W of power (Herculano-Houzel (2011)).

With energy efficiency being critical for future high performance and embedded information processing technologies, biological brains offer the archetype framework for human-engineered systems to succeed at tasks that lie beyond the reach of today's high performance computers (Nawrocki et al. (2016)). Neuromorphic systems, can be operated at various degrees of biological plausibility, directly mapping conventional artificial neural network algorithms onto hardware or capitalising on the rich dynamical behaviour of biological neurons for information processing (Hejda et al. (2021)).

Neural networks, i.e., collections of artificial neurons and synapses have been going through a strong focus not only on the development of deep neural networks using computer algorithms (Hinton and Salakhutdinov (2006)), but also in integrated neuromorphic microchips (Galluppi et al. (2014)) as the hardware that can reproduce neuro-transmission by interconnecting many artificial neuron like elements. This communication is encoded in sequences of intensity spikes, unlike the Boolean logic used in most current computers, as found in the unique information processing of the brain. Neurons are excitable systems, that is, if an external stimuli is above a certain threshold the neurons respond with an action potential, typically in the millisecond and milivolt range (Stillwell (2016)) and then return to their resting state. If the stimulus is not above the mentioned threshold the neuron does not fire the action potential, this is referred to as the all or none principle/law. After the neuron fires a spike there is a temporal window during which the neuron cannot fire another one, this is referred to as the refractory time.

The Resonant Tunneling Diode (RTD) is a two terminal device containing a nanometric Double Barrier Quantum Well (DBQW) that creates resonant energy levels which can lead to resonant tunneling transport of carriers. The DBQW acts as a filter for the electron waves controlling the transmission of

1. INTRODUCTION

carriers through the device in a non-linear manner, like an optical Fabry-Perot. These unique carrier transmission dynamics give the RTD an N-shaped current voltage (I-V) characteristic with the interesting property of having a pronounced Negative Differential Conductance (NDC) region. Due to the nanometric dimensions of the RTD active layers that can be very compact, high-speed of operation can be achieved because the quantum resonant tunneling effect through the very thin semiconductor layers is a very fast process. It is the N-shape I-V and the NDC region that the the RTD the potential to present neuromorphic properties such as electric excitability (Hänggi and Chua (2001)), (Ironsides et al. (2019)) and spike generation dynamics (Ortega-Piwonka et al. (2021)). These properties and other phenomena make the RTD a candidate for spike generation in a spiking neural network.

1.2 Objectives and Tools Used

This dissertation had as objective the study of the neuromorphic properties of circuits containing RTD devices, the main focus was the understanding of how RTDs with their non-linear current voltage characteristic can be used as spike generators.

The work started with the familiarization with the RTD operation principle, the study of the small and large signal electrical models of the RTD and with the implementation of a MATLAB tool capable of producing an I-V curve fitting according to the physics-based RTD current-voltage equation developed by Schulman et al. (Schulman et al. (1996)). After this initial work the characterization of the RTD followed, this consisted in the measurement of the RTD curves and an analysis of the RTD self oscillations when biased in their NDC regions. These two characterisations were carried out in order to obtain the parameters such as the bias voltages that work as the operation points of the RTDs for spike generation and the oscillation characteristics that define the spike that is going to be generated. After this a series of experimental measurements were performed in order to classify: the spikes generated, the operation points and respective stability's and the refractory times of the system. Finally a Simulink/Simscape model was developed in order to infer the neuromorphic property of excitability of the RTDs.

The tools used to carry out these objectives were MatLab for the analysis of the experimental data and Simulink/Simscape for the simulation of the RTD circuit. In the beginning of the work Matlab was used as a tool to perform the experimental analysis of the data such as the current-voltage characteristics and their respective curve fitted models under (Schulman et al. (1996)) I-V curve. Matlab was also the software used to create all of the plots presented in this dissertation.

The tools used in the experimental activities are presented in chapter 4.

1.3 Dissertation Overview

This dissertation is composed by six chapters. Chapter one is the introduction you just read.

In chapter two a small introduction to spiking neural networks and neuromorphic devices is put-forward, this serves as an introduction to the properties that the circuits containing RTDs need to have in order to be a promising neuromorphic technology.

In the third chapter the structure and functioning of the RTD is introduced, described and associated with the neuromorphic properties presented in chapter two.

The fourth chapter consists first on the methods developed in order to characterize the RTDs, both experimental and the developed software, followed by the experimental activities that were carried out to infer the neuromorphic properties of circuits containing RTDs. Finally the chapter is concluded by

1.3 Dissertation Overview

presenting a Simulink/Simscape model that is able to simulate the neuromorphic property of excitability of these devices.

In chapter five the results of the methods that were put forward in chapter four are presented and discussed.

Finally in chapter six the conclusions and proposals for future work are presented.

Chapter 2

Introduction to Neuromorphic Devices

2.1 Neuromorphic Devices

Neuromorphic engineering is a field that attempts to mimic the structure and behaviour of the brain in order to replicate some of its most significant characteristics such as its ability to process and integrate stimulus/information, its memory and learning capabilities and its high energetic efficiency. The root word *neuro-morphic*, means "having the shape, form or structure of the nerves/nervous system". One of the main motives behind the desire to create a machine that closely mimics the brain is due to its energetic efficiency: despite having a significantly large number of neurons and synapses, around 10^{11} and 10^{15} respectively, the human brain consumes around 25 W of power. (Herculano-Houzel (2011)) This is possible because of the massive parallel computation being performed by the vast number of cells.

Neural Networks (NNs), or Artificial Neural Networks (ANNs), are the designation given to these systems that closely mimic the structure of the brain. In general these are composed of two fundamental units, neurons and synapses, the neuron is used as the information processing and the synapse is used as the way to transmit and integrate processed signals between neurons. (Zhu et al. (2020))

2.1.1 Neurons

A typical biological neuron is composed by a cell body (soma), dendrites and a single axon, as illustrated in figure 2.1.

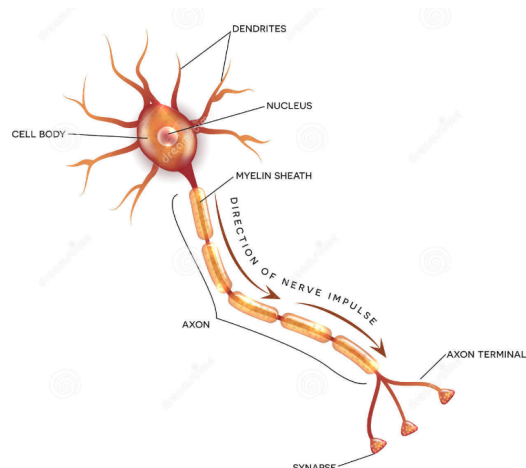


Figure 2.1: Diagram of a biological neuron. Adapted from: (Biological Neuron Diagram)

2. INTRODUCTION TO NEUROMORPHIC DEVICES

The majority of these nerve cells receive signals, encoded as spikes, through the dendrites and send out the response signal through the axon. The body cell of the neuron is able to receive and integrate information sent out from other neurons through a change of voltage potential that occurs across the neurons cell membrane. If the voltage potential reaches a given threshold the cell body generates an action potential (spike) that travels down the length of the neurons axon. Although the basic requisites for artificial neurons is to be able to achieve potential accumulation processes and spike generation functions, there are a few phenomenon that are observed biologically that can be related to the efficiency of computational power and capability of neurons.

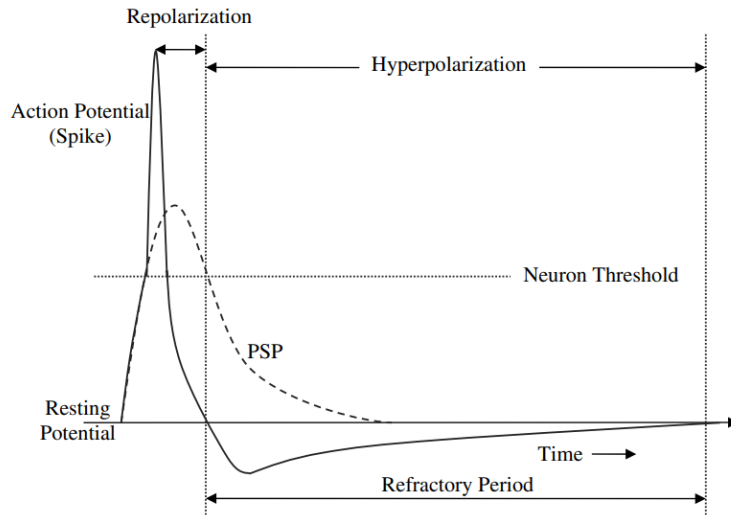


Figure 2.2: Internal state of a post synaptic neuron (spike), and some of its characteristics such as: resting potential, action potential and refractory period. Adapted from: (Ghosh-Dastidar and Adeli (2009))

The first intriguing phenomenon is related to the excitability of neurons following an "all-or-none"/"all or nothing " law, that is, when the stimulation intensity does not reach a certain threshold value, no response is given by that neuron, whereas if the stimulation intensity reaches this threshold, the action potential occurs (spike) and the maximum intensity is reached, as illustrated in figure 2.3.

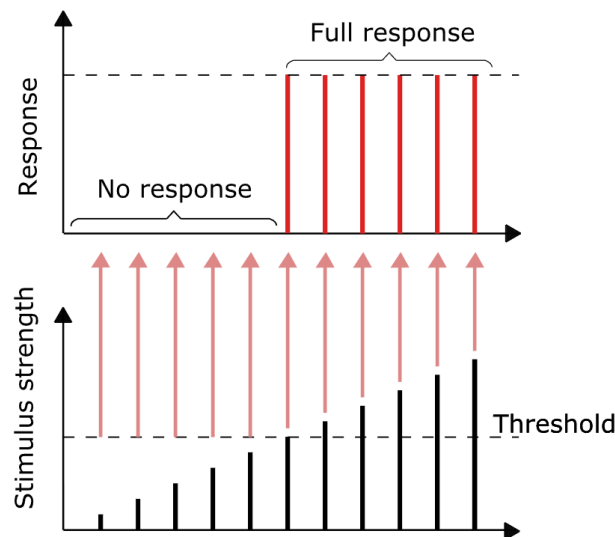


Figure 2.3: Illustration of the all-or-none law/principle Adapted from: (All-or-none law)

The refractory period, as exhibited in figure 2.2, is a temporal period during which the neuron cannot fire another spike. It refers to the amount of time it takes for a neuron to be able to respond to a second stimulus, once it returns to a resting state. The absolute refractory period refers to the depolarization and repolarization times, during this interval the neuron will not respond to a stimulus no matter how strong it is.

There are several spiking modes of communication in the brain, as illustrated in figure 2.4, this shows the complexity of the spiking behaviour of neurons, four of the major spiking modes include: regular spiking, intrinsically bursting, chattering and fast spiking. A few other requirements for artificial neurons is lateral inhibition and chaos. Lateral inhibition is the phenomenon that adjacent receptors suppress each other, and chaos comes due to the fact that neuron membranes have their own non-linear dynamics that can produce chaos.

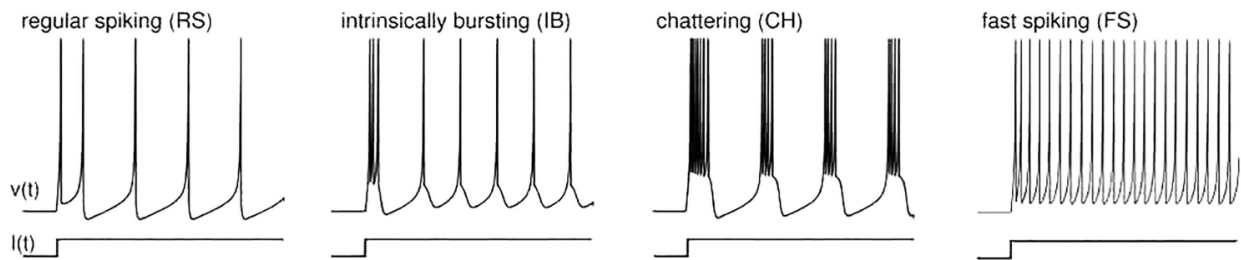


Figure 2.4: Four major spiking modes Adapted from: (Zhu et al. (2020))

2.1.2 Spiking Neural Networks

Inspired by the biological structure and functioning of the brain, Artificial Neural Networks (ANNs) are a succession of neurons and synapses, the neurons are assembled into layers and each layer is connected to the next by a set of synapses. The connection between layers can have many arrangements and weights. Presented as an example of an artificial neural network, the Fully Connected Network (FCN) illustrated in figure 2.5, consists on having all the units of a layer connected to every unit on the adjacent layer. A synapse only connects one pre and one post-synaptic neuron. The post synaptic neuron carries out the multiplication and summation of the pre synaptic incoming activation values x with their corresponding synaptic weights w (synaptic efficiency), a bias term b is added to the result giving (Bouvier et al. (2019)).:

$$y_j = \sum_i w_{i,j} + b_j \quad (2.1)$$

A spiking neural network is a special case of an artificial neural network in the sense that the communication between the neurons is made via impulses i.e spikes. The pre-synaptic neuron fires a spike that, when interacting with the post-synaptic neuron, can cause it to produce a spike or change its polarization potential slightly, this is referred to as the Post-synaptic Potential (PSP). These neurons are excitable, that is, when subject to some disturbance that causes it to cross its threshold the neuron will produce a spike.

2. INTRODUCTION TO NEUROMORPHIC DEVICES

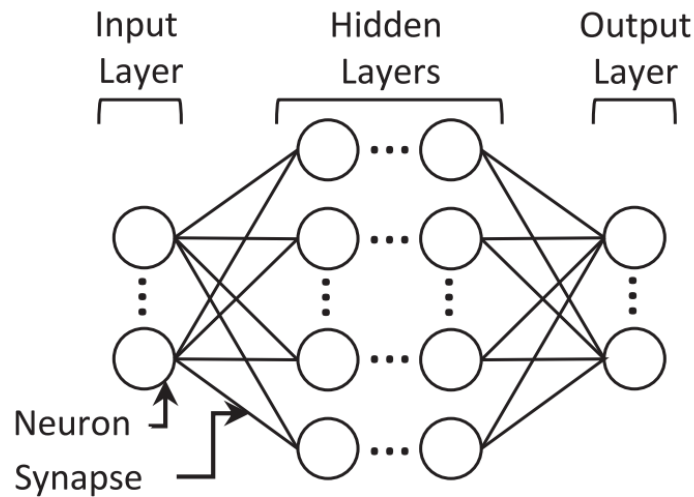


Figure 2.5: Schematic representation of a FCN. Adapted from (Bouvier et al. (2019))

The general working principle revolves around this phenomenon: a post-synaptic neuron when receiving an action potential from its pre-synaptic counterpart, will emit a PSP that stimulates its downstream neuron. When generalizing this to the whole network of multiple pre-synaptic neurons, each with multiple spikes, including multiple PSPs over time, the PSPs are temporally integrated to compute the internal state of the post-synaptic neuron over time. The post synaptic neurons fires when the integrated internal state crosses a given threshold (Ghosh-Dastidar and Adeli (2009)). Therefore spiking neurons communicate via spikes that can be described using binary representation and integration.

Several neuromorphic circuits that attempt to emulate the transmission of information in the brain have been proposed, like the IBM TrueNorth chip (Merolla et al. (2014)) and the Intel QuarK SE chip. These proposals have a Complementary metal-oxide semiconductor (CMOS) architecture and present low frequency (kHz) and much higher power consumption than the brain (Ortega-Piwonka et al. (2021)).

2.1.3 Information Representation in the Brain

The information encoding mechanism in the brain has been explained using a number of coding techniques, including rate coding, temporal coding, phase coding and burst coding.

Rate coding uses the spiking rates to represent information, that is, the frequency of the spikes is where the information is stored, it is a robust and simple mechanism and has been experimentally discovered in a lot of sensory systems such as virtual cortex and motor cortex. Nonetheless, rate coding is a scheme that presents limits such as a long processing period and slow information transmission (Srivastava et al. (2017)).

Temporal coding was proposed as a neural code that uses the precise spike timing to convey information in different forms, such as the timing of the first spike, the rank order between spikes and the relative spike latency to explain efficient and quick response mechanisms in our brain. The time to first spike coding technique offers extremely quick transmission speed by transmitting information to the destination neurons with the arrival of the first spike. Several experiments have highlighted the importance of the initial spikes in different areas of our nervous system, including the retina, auditory systems, and tactile afferents (Ponulak and Kasinski (2011)).

Phase coding, which has been experimentally in the hippocampus and olfactory system, involves encoding information in spike patterns whose phases are associated with naturally occurring background

2.1 Neuromorphic Devices

oscillation rhythms (Guo et al. (2021)).

The idea of burst coding was developed as a result of the widespread observation that neurons in numerous regions of the nervous system, including the auditory system, thalamus cortex, and hippocampus, also interact with one another by firing spikes rapidly (Zeldenrust et al. (2018)).

These four encoding mechanisms are all present in the communication in the nervous system and are all based on spikes.

Chapter 3

Resonant Tunneling Diode

3.1 Resonant Tunneling Diode

Resonant tunneling diodes are two terminal devices, thus referred as diodes, that belong to a class of semiconductor hetero-structure devices called mesoscopic devices. Mesoscopic structures are small enough so that the coherence of the wave function of the particle is preserved, in this case an electron. This implies that a classical analysis is not enough to describe the transport phenomena of electrons in the structure. At normal working temperatures the phase breaking distance of the electron (in semiconductors) is around 10 nm (Ironsides et al. (2019)).

3.2 Double Barrier Quantum Well

A DBQW RTD is formed by a low energy bandgap semiconductor layer (the well), such as InGaAs surrounded by thin layers (the barriers) of a higher energy bandgap material, such as AlAs, both sandwiched between lower energy bandgap materials, typically identical to the well material, thus forming a DBQW as illustrated in figures 3.1 and 3.2.

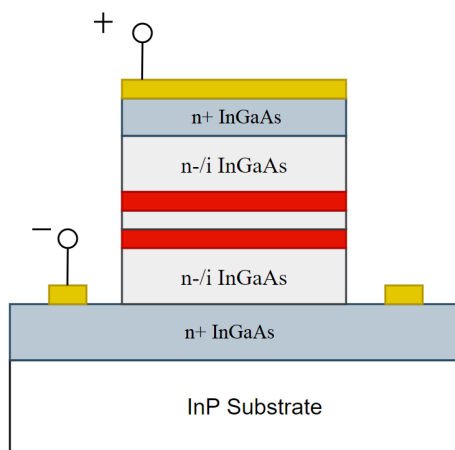


Figure 3.1: Schematic of a RTD with InGaAs in the well, AlAs as the barriers (red) and a InP substrate. The emitter and the collector contact layers are displayed in yellow.

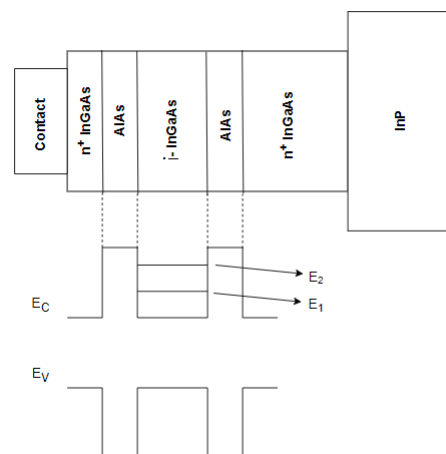


Figure 3.2: Illustration of the hetero-structure and energy-band diagrams for an InGaAs/AlAs DBQW. Resonant energy levels E_1 and E_2 are also shown.

A quantum well is formed inside of the two barriers, because of this well defined discrete quantum energy levels are created inside of it, as illustrated in figure 3.2, these can also be referred to as the

3. RESONANT TUNNELING DIODE

resonant energy levels of the DBQW.

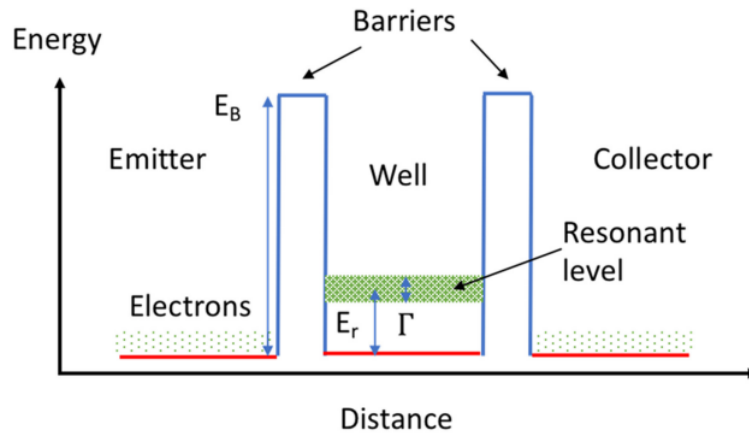


Figure 3.3: Schematic of the conduction band profile for a generic DBQW. E_B designates the energy of the potential barrier, E_r the energy of the resonant level and Γ the resonance width. Adapted from: (Ironsides et al. (2009))

Under this configuration the DBQW acts as an electron wave filter controlling the transmission of carriers through the device in a non-linear manner. When the energy of incoming carriers (electrons) is close to or equal to the energy levels of the quasi-bound states of the DBQW (resonance) that electron transmission is close to unity. When the energy of the carriers is not close to these levels (off resonance), the transmission is greatly reduced, as illustrated in figures 3.3 and 3.4.

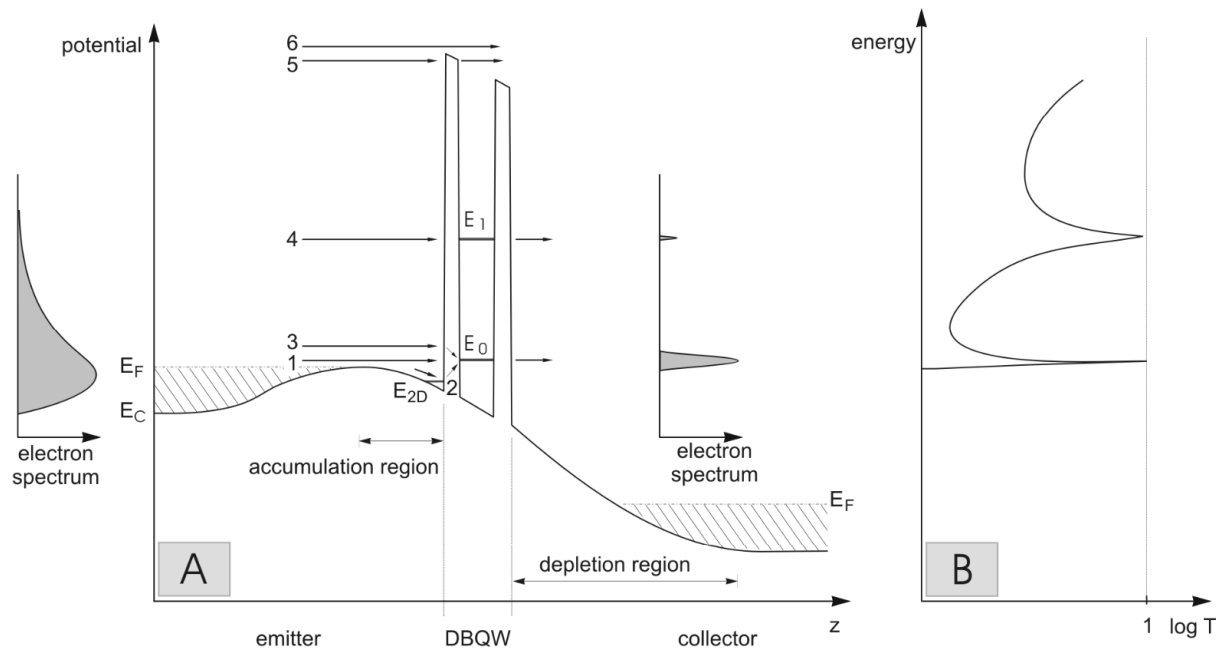


Figure 3.4: Band diagram of a DBQW heterostructure under an applied bias (A) with the corresponding transmission probability (B). The electron distribution before and after crossing the DBQW is also presented. Adapted from: (DBQW under bias)

These unique carrier transmission dynamics leads to the presence of a negative differential conductance in the RTDs current voltage characteristic.

Under an applied bias, carriers can tunnel from the emitter to the collector via energy states within the well, thus referred to as resonant tunneling. In the case of a DBQW structure, resonant tunneling occurs through the barriers via quantized states that are defined in the well, this causes the tunneling probability to exhibit peaks when the energy of the incident particle coincides with the energy of these

3.2 Double Barrier Quantum Well

quantized states. Electrons in the emitter region cannot cross the barrier to the collector side but at certain given energies, the probability of transmission of these passing through the well is very high due to the resonance energy levels found in the well.

This property gives the RTD a non-linear current voltage (I-V) characteristic, composed by two Positive Differential Conductance (PDC) regions separated by a NDC region. When DC biased to an appropriate voltage in the NDC region the device presents negative conductance, this means that as the voltage applied to the terminals is increased, the current decreases. This implies that the device has electrical gain, i.e., generates AC power rather than absorbing power. When considering electrical feedback caused by other components, for example an inductor and a capacitor in an RLC circuit, and in the situation where the electrical gain overcomes the losses the RTD, when biased to the correct voltage in the NDC region can produce a very high frequency oscillatory signal (Ironsides et al. (2009)), up to 2 THz (Izumi et al. (2017)).

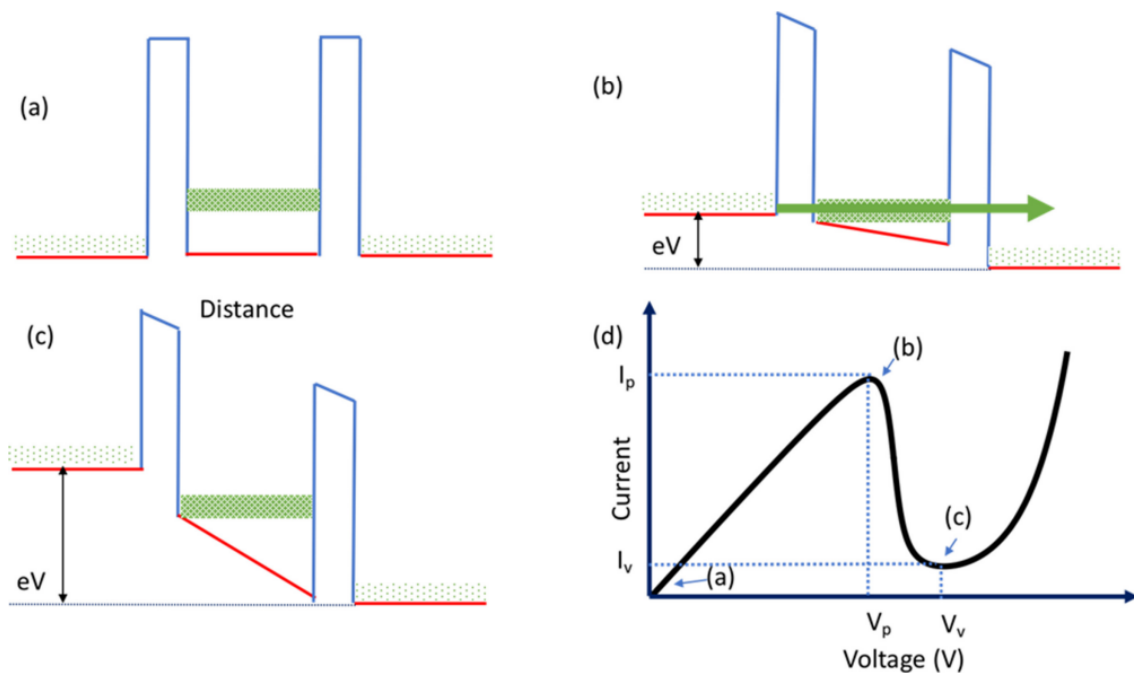


Figure 3.5: Conduction band profiles for different bias voltages. (a) $V = 0$; (b) $V = V_{peak}$; (c) $V = V_{valley}$. (d) Schematic of the current voltage characteristic. Adapted from: (Ironsides et al. (2009))

As illustrated in figure 3.5, when a positive emitter voltage is applied to the RTD the bottom of the conduction band increases in energy on the emitter region in respect to the collector. As the voltage increases, more electrons are going through the double barrier until a maximum current is reached I_{peak} . This corresponds to the electrons going through the resonance level that lead to the first PDC region when the voltage is between 0 V and V_{peak} .

When the voltage is increased beyond V_{peak} the resonance condition is lost, the current drops until it reaches a local minimum I_{valley} . The region between V_{peak} and V_{valley} is thus referred as the NDC region because a slight increase in voltage pushes the emitter conduction band a bit further away from the resonant level causing less electrons to cross the double barrier thus leading to a reduction of the current.

If the voltage is increased beyond V_{valley} the current increases again like in the first PDC, this happens due to the fact that, as the voltage increases, the emitter conduction band is high enough to make electrons cross the second resonance level and eventually over the barrier, as illustrated in figure 3.6 that shows the

3. RESONANT TUNNELING DIODE

current transport mechanisms of the DBQW RTD. Theoretically more NDC regions can come after this but they wont be explored in this dissertation.

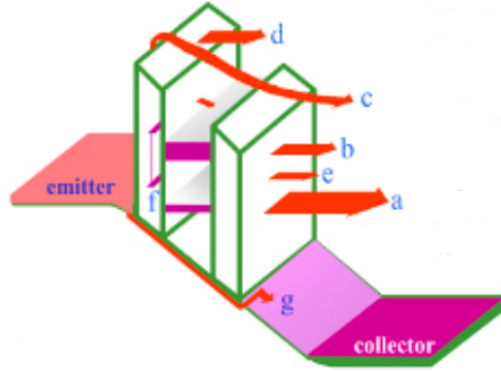


Figure 3.6: Current transport mechanisms in the DBQW RTD. a) Resonant tunneling; b) Tunneling through higher levels; c) Thermionic emission; d) Field assisted tunneling; e) tunneling through evanescent states; f) inelastic tunneling; g) leakage current. Adapted from: (Current transport mechanisms)

3.3 Current Voltage Characteristic

The relation between the electrical conductance of a quantum conductor to the transmission coefficients of the transmission channels is given by Landauer's formula:

$$G = G_0 \sum_0^{All} T_i(E, V) \quad (3.1)$$

Where G is the electrical conductance, G_0 is a constant and $T_i(E, V)$ a channel transmission coefficient. The transmission channels need to be divided into two channels, a resonant to account for the transmission through the quantum well and a non-resonant for all the other channels, i.e., transmission of high energy electrons over the barrier.

For transport through the resonance level the resonant tunneling current formula, developed by Tsu-Esaki (Esaki (1974)), is given by equation 3.2:

$$J = \frac{e}{2\pi\hbar} \int N(E)T(E)dE \quad (3.2)$$

Where e is the elementary charge of the electron, $T(E)$ the transmission coefficient and $N(E)$ the number of available electrons for tunneling (per unit area) from the emitter. Supported by the effective mass approximation (Schulman et al. (1996)) developed the expression presented on equation 3.3 for the current density $J(V)$ as a function of the applied voltage.

$$J_R(V) = \frac{em^*k_B T}{2\pi^2\hbar^3} \int_0^\infty \mathbf{T}(E, V) \ln \left[\frac{1 + e^{(E_F - E)/(k_B T)}}{1 + e^{(E_F - E - eV)/(k_B T)}} \right] dE \quad (3.3)$$

Where, m^* is the effective mass of the electrons in the semiconductor, k_B is the Boltzmann constant, T is the absolute temperature of the device, \hbar is the reduced Planck constant, V is the applied voltage, E is the energy measured from the conduction band edge and E_F the Fermi energy of the semiconductor in the emitter.

(Schulman et al. (1996)) proposed a Lorentzian approximation for the transmission coefficient thus

3.3 Current Voltage Characteristic

taking the form presented in equation 3.4.

$$T(E, V) = \frac{\left(\frac{\Gamma}{2}\right)^2}{\left[E - \left(E_r - \frac{eV}{2}\right)\right]^2 - \left(\frac{\Gamma}{2}\right)^2} \quad (3.4)$$

Where E_r corresponds to the energy of the resonant level relative to the bottom of the well at its center and Γ is the energy level resonance width (depicted in figure 3.3). This formula assumes that the barriers have equal widths and that half of the voltage drop falls from the emitter to the center of the well. For a small Γ , the transmission coefficient is negligible except when E is close to resonance, i.e., $E \cong E_r - \frac{eV}{2}$. Substituting $\left(E_r - \frac{eV}{2}\right)$ for E and taking it out of the integral allows the integral to be solved and the solution to take the form presented in in equation 3.5.

$$J_R(V) = \frac{em^*k_B T \Gamma}{4\pi^2 \hbar^3} \ln \left[\frac{1 + e^{(E_F - E)/(k_B T)}}{1 + e^{(E_F - E - eV)/(k_B T)}} \right] \cdot \left[\frac{\pi}{2} + \tan^{-1} \left(\frac{E_r - \frac{eV}{2}}{\frac{\Gamma}{2}} \right) \right] \quad (3.5)$$

This equation only takes into account the first peak and NDC of the RTD. It does not consider other non-resonant current mechanisms that contribute to the valley current such as tunneling through other energy levels or inelastic scattering or other transport phenomena that might be present (see figure 3.6).

So equation 3.6, the general equation of a diode, is added in order to account for this transmission in the non-resonant channels.

$$J_{NR}(V) = H \left(e^{n_2 V e / (k_B T)} - 1 \right) \quad (3.6)$$

Adding both equations gives the generalized current voltage characteristic for a RTD, presented in equation 5.1.

$$J(V) = A \ln \left[\frac{1 + e^{(B - C + n_1 V) e / (k_B T)}}{1 + e^{(B - C - n_1 V) e / (k_B T)}} \right] \left[\frac{\pi}{2} + \tan^{-1} \left(\frac{C - n_1 V}{D} \right) \right] + H \left(e^{n_2 V e / (k_B T)} - 1 \right) \quad (3.7)$$

Where, $H = en_i^2 \left(\frac{D_n}{N_a L_n} + \frac{D_p}{N_d L_p} \right)$, n_i is the intrinsic concentration of carriers, D_n and D_p are the diffusion coefficient of the electrons and holes respectively. L_n and L_p are the electron and hole diffusion lengths, N_a is the density of acceptors and N_d is the density of donors. A is in Acm^{-2} . B , C and D are in V . n_1 and n_2 are dimensionless and H , the saturation current density, is in Acm^{-2} . n_1 and n_2 are adjustment parameters proposed by (Schulman et al. (1996)). With this equation it is possible to fit experimental I-V curves, the fit is performed with the seven coefficients: A , B , C , D , H , n_1 and n_2 . In figure 3.7, the I-V characteristic model is presented along with its derivative with polarization voltage varying from 0 to 2 V.

3. RESONANT TUNNELING DIODE

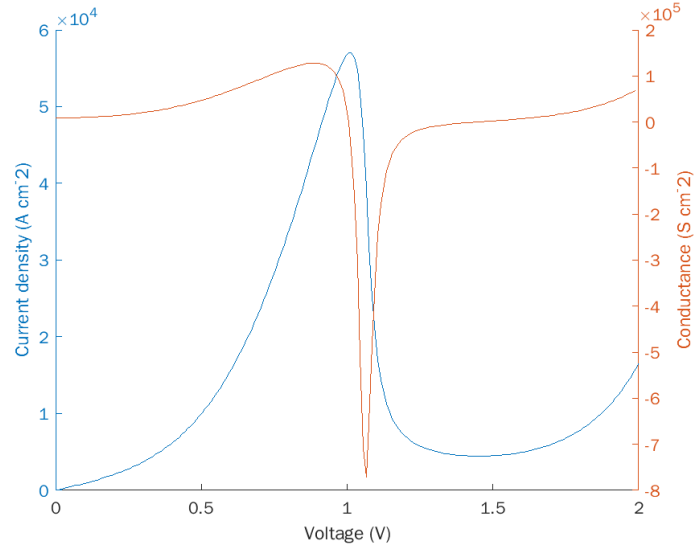


Figure 3.7: Current density as a function of voltage in an RTD (Blue); Conductance as a function of the voltage (Orange). Parameters used: $A = 1.4 \times 10^4 \text{ A} \cdot \text{cm}^{-2}$; $B = 0.0461 \text{ V}$; $C = 0.1417 \text{ V}$; $D = 0.0373 \text{ V}$; $H = 0.04803 \text{ A} \cdot \text{cm}^{-2}$; $n_1 = 0.1325$; $n_2 = 0.1346$

Important metric parameters of the RTD current voltage characteristic include the peak and valley voltages V_{Peak} and V_{Valley} ; the peak/valley currents I_{Peak} and I_{Valley} and respective densities of current J_{Peak} and J_{Valley} . The Peak to Valley Current Ratio (PVCR) is another important parameter and is given by the ratio of the peak and valley currents. Finally the value of negative differential resistance R_{NDR} that is given by the inverse of the derivative of the current voltage characteristic is the last parameter, put forward in equation 3.8.

$$R_{NDR}(V) = \frac{1}{F'(V)} \quad (3.8)$$

Where $F(V) = M \cdot J(V)$ and M is a scaling factor that takes into account the size (area) of the RTD device.

3.4 RTD Model

The basic AC signal equivalent circuit for a RTD consists of four elements: the series inductance L , the series resistance R , the diode capacitance C and a voltage dependent current source $F(V)$ that describes the DC current voltage characteristic of the device. The circuit consists of a resistance and an inductor in series that represent the parasitic components associated with the DC voltage source and the RTD is represented as a capacitor C placed in parallel with the voltage dependent current source $F(V)$, as shown in figure 3.8.

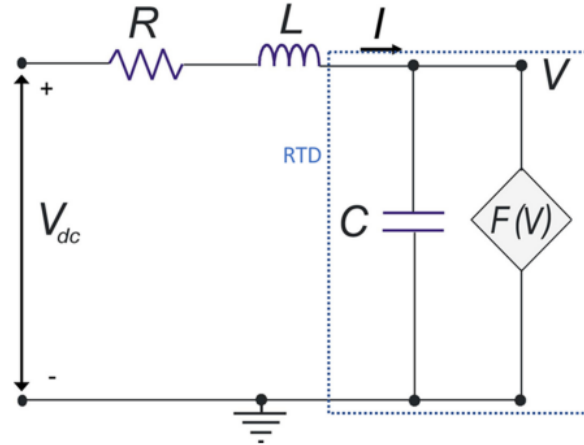


Figure 3.8: Basic AC signal equivalent circuit for a RTD, R and L represent the parasitic components and C and $F(V) = M \cdot J(V)$ a voltage dependent current source. Adapted from (Ironsides et al. (2009))

The time evolution of voltage and current are given by equations 3.9 and 3.10 respectively.

$$\dot{V} = \frac{1}{C} [I - F(V)] \quad (3.9)$$

$$\dot{I} = \frac{1}{L} [V_{DC} - RI - V] \quad (3.10)$$

With some algebraic manipulations of these equations a non-linear second order differential equation is obtained:

$$\ddot{V} + H(V)\dot{V} + G(V) = 0 \quad (3.11)$$

Where, $H(V) = \frac{R}{L} + \frac{1}{C} \frac{dF(V)}{dV}$ and $G(V) = V - V_{DC} + RF(V)$. Equation 3.11 represents a Liénard oscillator (Ironsides et al. (2009)).

Summing up, the inductive elements associated with the circuit and the RTD capacitance produce electrical feedback that cause the circuit presented in figure 3.8 to oscillate, depending on whether the gain overcomes the losses the RTD may or may not sustain the oscillation, the RTD, as discussed, presents this gain in its NDC region. When biased in the NDC region the circuit in figure 3.8 acts as a relaxation oscillator. The condition for operation is that the series resistance is less than a critical value, given by the absolute value of the reciprocal of the minimal conductance, that is, $R < |R_C|$ where

$$R_C = -\frac{1}{\min \{F'(V)\}} \quad (3.12)$$

The functioning of the RTD as a Voltage Controlled Oscillator (VCO) can be explained in the following way: when biased in its NDC region we are polarizing the device on an "unstable" region. This causes the device to transition to a "stable" ohmic region, making the RTD move to an adjacent PDC region changing the value of the voltage on its terminals. The values of voltage will then revolve around the the bias voltage that was applied to the device.

The possible operation points of the RTD are determined by the intersection of the load line with the nonlinear current voltage characteristic. The load line is a linear equation of the form

$$y = -\frac{1}{R}x + \frac{V_{DC}}{R} \quad (3.13)$$

3. RESONANT TUNNELING DIODE

this implies that a change in voltage causes the load line to move in parallel along the horizontal axis, a change in resistance causes the load line to change its slope.

Solving the system of equations 3.9 and 3.10 implies that the stable fixed points (bias voltages) need to obey $f'(V) > 0$ (Ortega-Piwonka et al. (2021)), with this information it is clear that being either in the first or second PDC regions is enough for a fixed point to be stable while the fixed points in the NDC region are unstable.

The effect of the change in $\sqrt{\frac{C}{L}}$ is also important in the analysis of the oscillation. If $\sqrt{\frac{C}{L}} \sim 1$ the values at which the voltage will oscillate will be well-rounded orbits with $V(t)$ smoothly evolving over time as presented in figures 3.9 and 3.10.

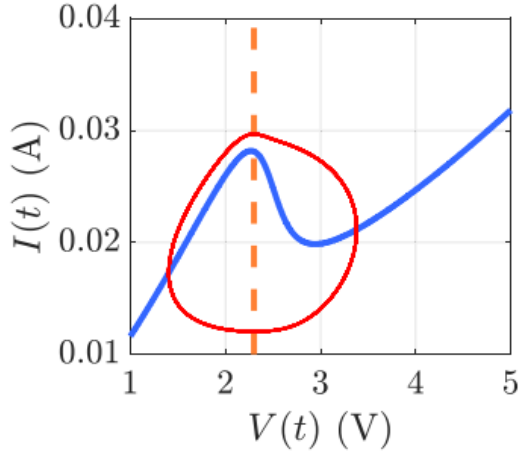


Figure 3.9: Orbit of the oscillation in the current voltage characteristic for a high $\sqrt{\frac{C}{L}} (\sim 1)$. Adapted from (Ortega-Piwonka et al. (2021))

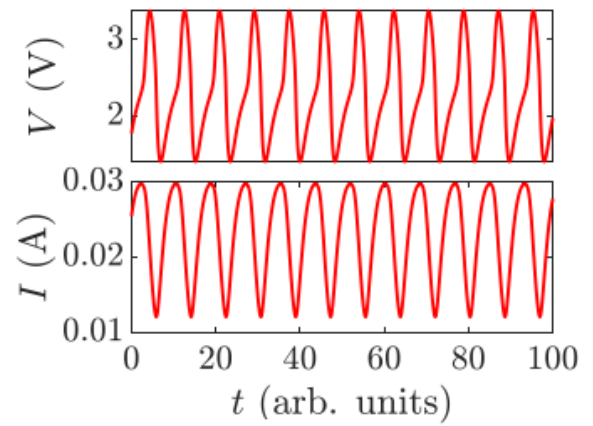


Figure 3.10: Corresponding waveform for a high $\sqrt{\frac{C}{L}} (\sim 1)$. Adapted from (Ortega-Piwonka et al. (2021))

Nevertheless, as $\sqrt{\frac{C}{L}}$ is decreased the orbits will become stiffer, if $\sqrt{\frac{C}{L}}$ is sufficiently small four stages can be recognized in each period of oscillation, two slow stages and two fast stages, as illustrated in figures 3.11 3.12. This is referred as slow-fast dynamics.

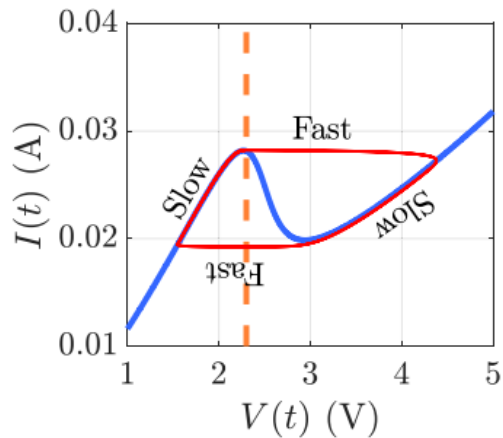


Figure 3.11: Orbit of the oscillation in the current voltage characteristic for a low $\sqrt{\frac{C}{L}} (0.001)$. Adapted from (Ortega-Piwonka et al. (2021))

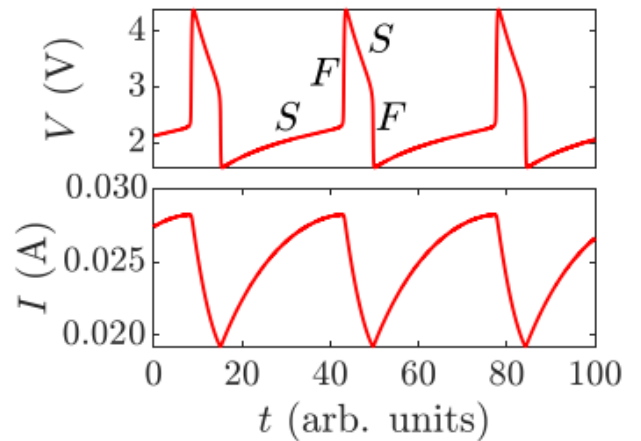


Figure 3.12: Corresponding waveform for a low $\sqrt{\frac{C}{L}} (0.001)$. Adapted from (Ortega-Piwonka et al. (2021))

The first slow stage corresponds to the orbit that overlaps the RTD current voltage characteristic in the first PDC and the voltage and current increase steadily, that is all of the electrons are crossing

the DBQW. When the maximum of the first PDC region is reached the first fast stage begins and the voltage increases suddenly, this stems from the fact that, if $\sqrt{\frac{C}{L}}$ is small then any alteration in the voltage is larger than the corresponding alteration in current which remains constant and larger than the current voltage characteristic, this implies that not all of the electrons are crossing the DBQW and charges accumulate at the ends. The orbit reaches the second PDC region in a very short time, the second slow stage begins and the voltage decreases slowly until it reaches the second PDC minimum. Then, the second fast stage begins where a sudden decrease in voltage and almost no decrease in current is seen, because the current is smaller than the current voltage characteristic this means that the ends of the DBQW are being discharged.

3.5 RTD Excitable Response

The excitable response of the RTD can be understood as a single one of these orbits, that is, if the device is biased near its NDC region in either one of its PDC regions the intersection point of the load line with the I-V characteristic is a stable attractor, as illustrated in figure 3.13. This implies that if a disturbance in the bias voltage is above a certain threshold and lasts long enough the system will present a single orbit (red) and only one oscillation/spike will be generated.

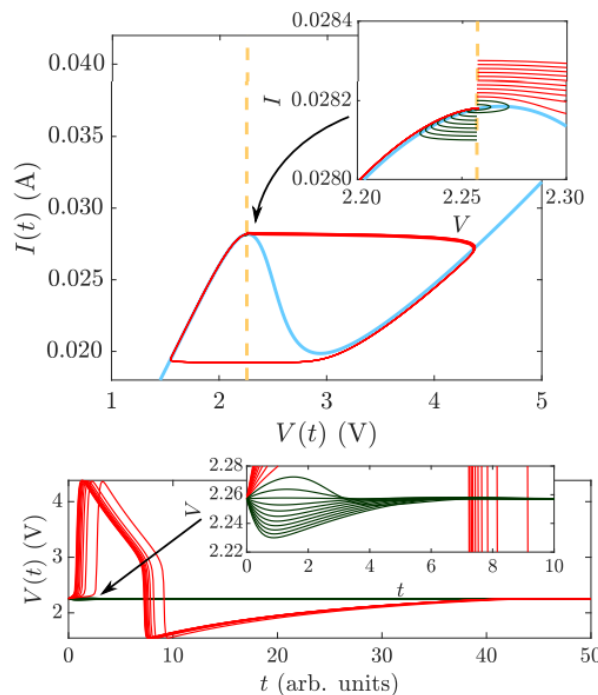


Figure 3.13: System response to several perturbations out of its natural equilibrium parameters. Adapted from (Ortega-Piwonka et al. (2021))

The orbit that is covered is similar to the stable limit cycle obtained for when the RTD is in its NDC. If the disturbance is not enough to cause the RTD to enter its NDC region the output is a small response that decays exponentially, also illustrated in figure 3.13 (black). In the same sense if the RTD is biased in its second PDC region close to the NDC a different orbit will be covered, in this case the voltage, instead of first rising and then decaying it would decay to then increase presenting a spike that is flipped when compared with the one presented in figure 3.13.

Chapter 4

Methods

In this chapter the methods that were developed and implemented in this dissertation are put forward. First the RTD samples provided are analysed where some of its characteristics are explored such as its structure, epilayers and electrical connections. After this, the methods used to electrically characterize the devices are talked through, starting from the extraction of the I-V characteristic, followed by the curve fitting software created to obtain a mathematical expression that replicates the behaviour of the corresponding I-V characteristic. After this the RTD NDC regions were characterized more specifically its self-oscillations. Following this, the experiments designed to infer and describe the spiking dynamics of the RTDs are put forward starting from the experimental setup going through the generated spikes characteristics, the voltage threshold, the bias voltages and the refractory times. The MatLab Simulink/Simscape simulator implemented that uses the AC signal equivalent circuit of the RTD and the I-V curve obtained with the curve fitting algorithm is presented at the end of the chapter.

4.1 Characterization of the RTDs

An understanding and characterization of the properties of RTDs is key in order to study the neuro-morphic properties of circuits containing them. In this section the characterization of the RTD samples provided by the ChipAi project is described. First a brief description of these samples is put forward where the DBQW structure and the semiconductor materials are discussed. Then the experiments performed are described, where the experimental setup used is presented and talked through. After this, the procedure used to extract the current voltage characteristic is put forward. Succeeding this, the method used to extract the current voltage characteristic is put forward. Finally, a curve fitting algorithm that uses (Schulman et al. (1996)) model was developed and applied to the I-V curves.

4.1.1 RTD samples

The RTDs used in this dissertation were provided by the Eindhoven University of Technology under the ChipAi project. These are epitaxially grown on a semi-insulating InP wafers. The layerstack is displayed in figure 4.1. The RTD devices are circular, as shown in figure 4.2. The devices that were studied in this dissertation have six different radius: 2.5, 3.5, 4, 4.5, 5 and 5.5 μm . The barrier is made from AlAs and has a 1.7 nm thickness. The well is composed of InGaAs layers with a thickness of 5.7 nm. The RTD emitter and collector consist of identical highly doped InGaAs layers for electrical contacts.

4. METHODS

Layer #	Thickness (nm)	Semiconductor	Doping (cm)	Description
12	200	InP	n.i.d	Cap Layer
11	100	In _{0.532} Ga _{0.468} As	N = 5e19	N-contact RTD (emitter)
10	50	n-InGaAs	N = 5e16	N- doped layer
9	2	InGaAs	n.i.d	Dopant diffusion stop layer
8	1.7	AlAs	n.i.d	Barrier layer
7	5.7	InGaAs	n.i.d	Well layer
6	1.7	AlAs	n.i.d	Barrier layer
5	2	InGaAs	n.i.d	Dopant diffusion stop layer
4	50	n-InGaAs	N = 5e16	N- doped layer
3	50	n-InGaAs	N = 5e18	N+ doped layer
2	20	n-InP	N = 5e18	N doped layer (etch stop layer)
1	100	n-InGaAs	N = 1e19	N contact RTD (collector)

Figure 4.1: Epilayers structure of the RTDs provided by the ChipAi project.

A schematic of an RTD device is shown in figure 4.2. with the red dot representing the top of the pillar. All the different sized RTDs are placed in the same wafer side by side as shown in figure 4.3.

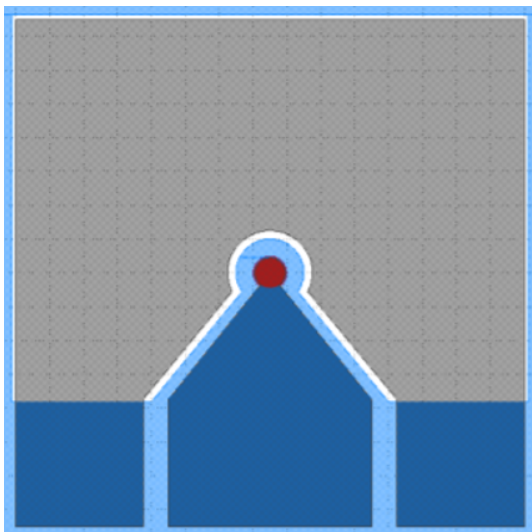


Figure 4.2: One element RTD illustration.

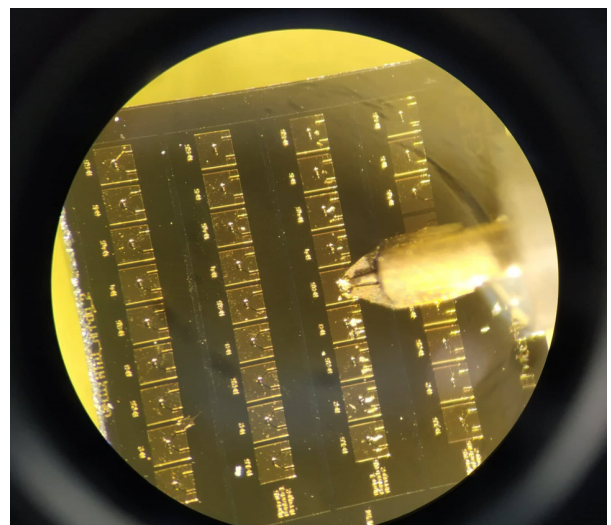


Figure 4.3: RTDs under the microscope.

4.1 Characterization of the RTDs

The RTDs were connected to the characterization circuit through 50Ω impedance in-wafer microwave probes (DC to 40 GHz) with a Ground Signal Ground (GSG) configuration which contact the RTD Co-planar Waveguide (CPW) transmission line, which consists of three paired conducting tracks with the central conductor acting as signal pad and the side pads acting as ground plane.

One characteristic of these RTDs is that they can be operated in forward bias: from 0 to 2 V; or under a reverse bias 0 to -2 V, as shown in figure 4.4 provided by ChipAi, for three of the RTDs ($4.5 \mu\text{m}$, $5 \mu\text{m}$, $5.5 \mu\text{m}$ radius's).

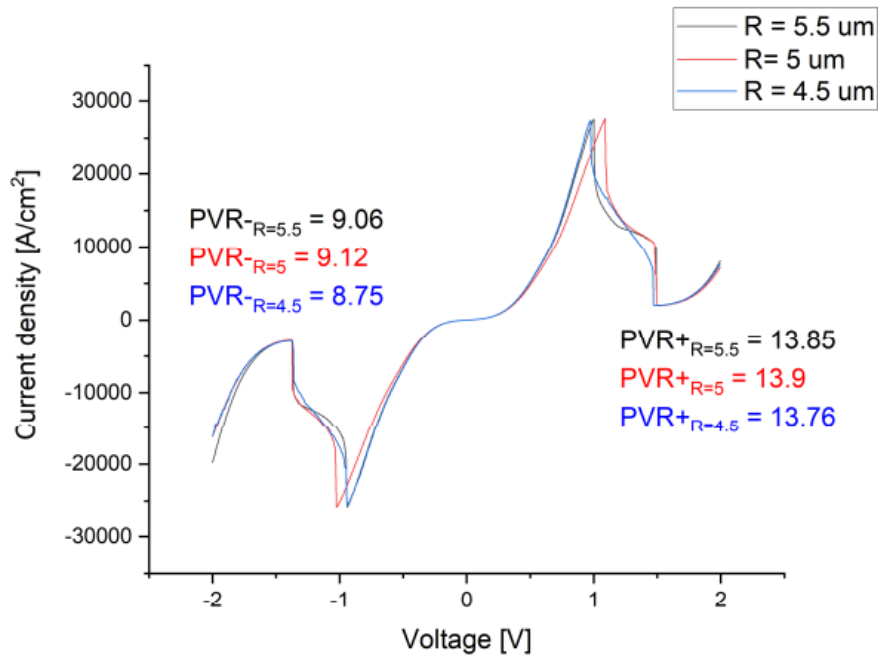


Figure 4.4: I-V characteristics provided by the ChipAi project in forward and reverse bias for the $4.5 \mu\text{m}$, $5 \mu\text{m}$, $5.5 \mu\text{m}$ radius RTDs.

4.1.2 Electrical Characterization of the Devices

The characterization of the devices as discussed before consisted in retrieving their current voltage characteristics experimentally and then applying the equation developed by (Schulman et al. (1996)) to obtain a function that mimics their I-V curves. After this the characterization of the self-oscillation of the RTDs in their NDC regions was performed.

4.1.2.1 Experimental Setup

The experimental setup constructed to electrically characterize the RTD samples is depicted in figure 4.5. The RTDs, shown on the right, were placed on a the working station under the microscope and the RF GSG probes, shown in figure 4.3, would be lowered until it came into contact with the device CPW pads (the three blue areas illustrated in figure 4.2).

The sourcemeter (Keithley 2450 Source meter) was used as a voltage supply all while measuring the current, it was connected to the Bias Tee (HP 11612A Bias Network 45 MHz - 26.5 GHz), a key component used in order to setup the DC bias of the device without disturbing the other components and

4. METHODS

equipment's and to allow injection and/or extraction of the RF signals. The part of the power divider (Tectronix Power Divider AM56113)) is that when coupled with the short circuit is creates a resonant cavity that, with the RTD, produces an RF signal. In the first end of the power there is a DC block to guarantee that the appropriate DC bias voltage reaches the RTD. The oscilloscope used was the Rohde & Schwarz RTP164 16 GHz Oscilloscope employed to observe the RTD self-oscillations as the bias point crosses the NDC region of the device I-V curve.

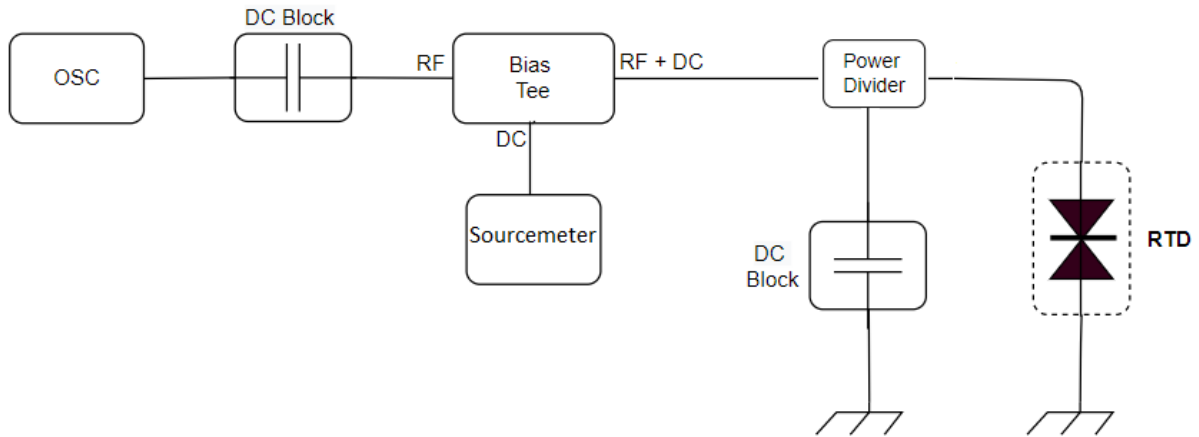


Figure 4.5: Schematic of the experimental setup used to measure the I-V characteristic of the RTDs.

The setup used in the laboratory presented in figure 4.6.

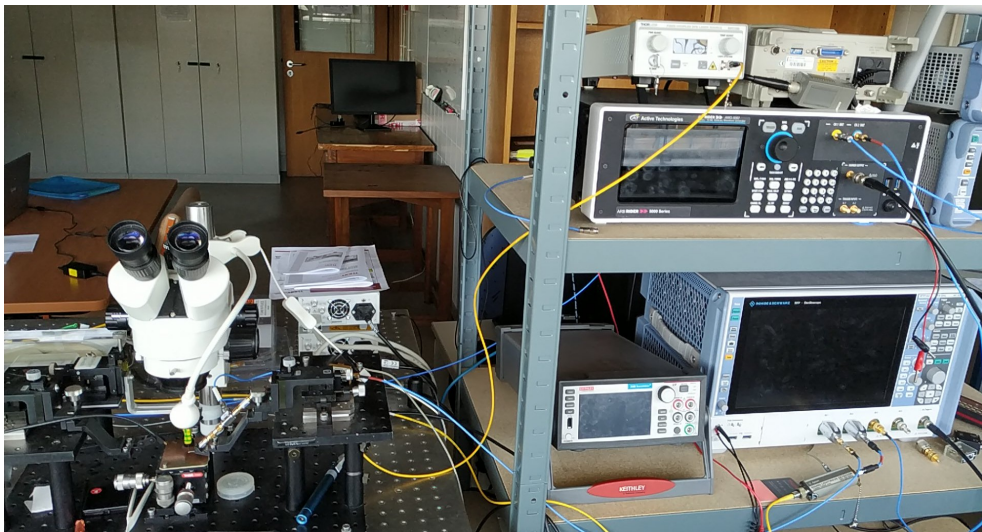


Figure 4.6: Experimental setup used in this dissertation.

On the right is the oscilloscope, the AWFG, the sourcemeater and the power supply, on the left the working bench, the microscope and the other components such as the bias tee and the microscope where the RTD were connected.

The experimental procedure consisted in using the sourcemeater to perform a dual sweep of voltage applied to the RTD all while measuring the current passing through the circuit. First a double sweep was performed with voltages varying from 0 to -2 V with 10 mV steps on all the RTDs. Because these RTDs work both under forward or reverse bias, a similar double sweep was performed with the RTD forward bias, this time with voltages varying from 0 to 2 V. This means that for each RTD there were four current

4.1 Characterization of the RTDs

voltage characteristics, two for the forward bias and another two for the reverse bias. From this point on the 0 to 2 V sweeps shall be referred as the ascending and the 0 to -2 V sweeps the descending. The sourcemeter automatically put the data in a file that was extracted to an USB drive and then loaded into Matlab.

4.1.3 Curve Fitting Software for the characterization of the RTDs

In order to analyse the RTD I-V characteristic and to use it in the developed RTD circuit simulation software a curve fitting software was developed. As explained in chapter 3, a curve fitting of the I-V characteristic can infer many of the properties of the RTD. Equation 5.1 was used to fit the experimental data and A, B, C, D, H, n_1 and n_2 were the curve fitting coefficients used. Before the curve fitting software is presented it is important to delineate some of the pre-processing that needed to be performed on the data.

First the data was loaded to Matlab and, because of the nature of the extraction of data (dual sweep of voltage), the data was split in half in order to have only one curve. In the case of the reverse bias I-V curves both the voltages and respective currents were multiplied by -1 in order to make them shift to the first quadrant. Second, the current was divided by the area of the device at hand, the area of the pillar disc, because the model devised by Schulman Schulman et al. (1996) considers the density of current instead of the total current flowing through the device.

Because of the nonlinear nature of the density of current equation, the curve fitting method used works around the "custom equation" functionality present in the *fit()* function in Matlab. This equation uses the Nonlinear Least Squares algorithm to give the coefficients of the curve fitting.

Several constraints were then added to make the algorithm converge to the best possible values of curve fitting parameters. The first constraint is that the points on the NDC need to be eliminated because of the DC extraction of data. The second constraint is that all of the curve fitting parameters need to be positive. Finally the last constraint applied to the fit was the starting values of the coefficients.

4.1.4 Voltage Controlled Oscillator

A voltage controlled oscillator is an oscillator circuit whose frequency can be controlled or varied by a DC input voltage. The RTD can then be operated as a VCO by applying a DC bias voltage on its NDC region. The output frequency, amplitude and waveform of oscillation depend on the input bias voltage.

4.1.4.1 Experimental Setup

The experimental setup used to characterize the RTDs in their NDC regions, is presented in figure 4.7. This time, instead of using the sourcemeter, the bias voltage device was a power supply (QL355P Power Supply). The rest of the components were the same as the ones described in the experimental setup used for the characterization of the devices.

4. METHODS

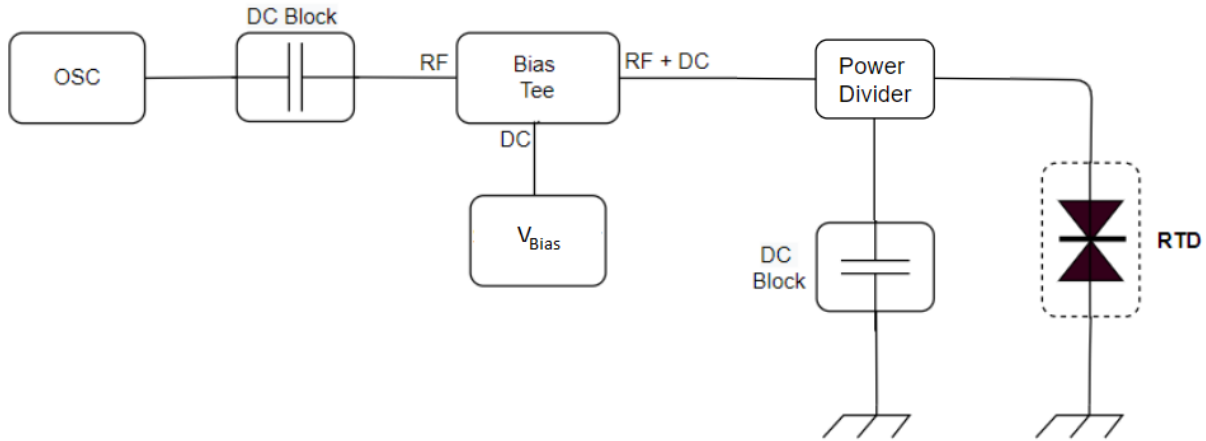


Figure 4.7: Experimental setup used to characterize the oscillating region of the RTDs.

The power supply biases the RTD without interfering with the returning signal because of the use of the Bias Tee, the RTD starts oscillating when biased in its NDC region and the signal then feeds into the oscilloscope.

The experimental procedure consisted firstly in biasing each RTD near their peak voltages, then voltage would be increased and the device would enter its NDC region and start oscillating. The signal was then picked up in the oscilloscope and the frequency and peak to peak voltage were retrieved for steps of 20 mV in DC bias voltage. This procedure was then conducted in the opposite direction as well, that is, the devices were biased near their valley voltages and the voltage would be decreased until they started oscillating, the peak to peak amplitudes and frequencies were retrieved again for each decreasing step of 20 mV in the bias voltage.

4.2 Spiking using RTDs

As put forward in section 3.5, in order to produce spikes the RTDs need to be biased at their peak and valley voltages (see figure 3.13) and a small disturbance needs to be performed upon this bias voltage as illustrated in figure 4.8. This disturbance causes the RTDs to enter their NDC regions and produce a single oscillation that can be interpreted as a spike.

Having six RTDs that work both under forward and reverse bias means that there are potentially twenty four possible polarization points in these RTDs. Using these points defined in the characterization of the devices section 4.1 as the bias voltages, and adding a Arbitrary Wave Function Generator (AWFG) to the setup presented in 4.7 to serve as the source of the disturbance signal was the method used to induce spiking as schematically represented in figures 4.8 and 4.9.

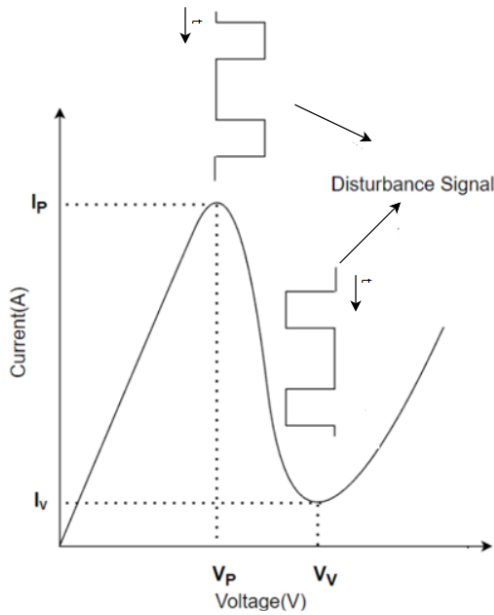


Figure 4.8: Concept behind spike generation using the non-linear nature of the current voltage characteristic of the RTDs in the forward bias.

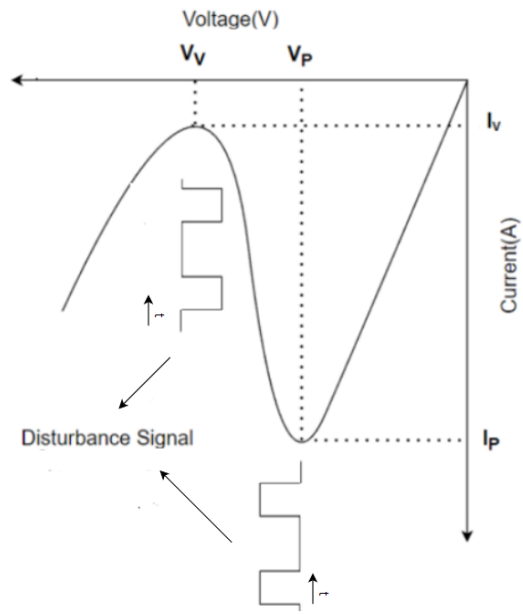


Figure 4.9: Concept behind spike generation using the non-linear nature of the current voltage characteristic of the RTDs in the reverse bias.

These figures indicate that for each bias point the disturbance signal is different. The forward bias peak needs to have a positive pulse disturbance in order to enter its NDC region while the reverse bias peak needs a negative pulse disturbance. As for the valleys, the forward bias one needs to have a negative disturbance and the reverse bias valley needs to have a positive disturbance. The increasing voltage path shall be referred to as the ascend and the decreasing voltage path the descend.

4.2.1 Experimental Setup

The experimental setup used to characterize the RTDs spike generation properties that were described above is presented in figure 4.10.

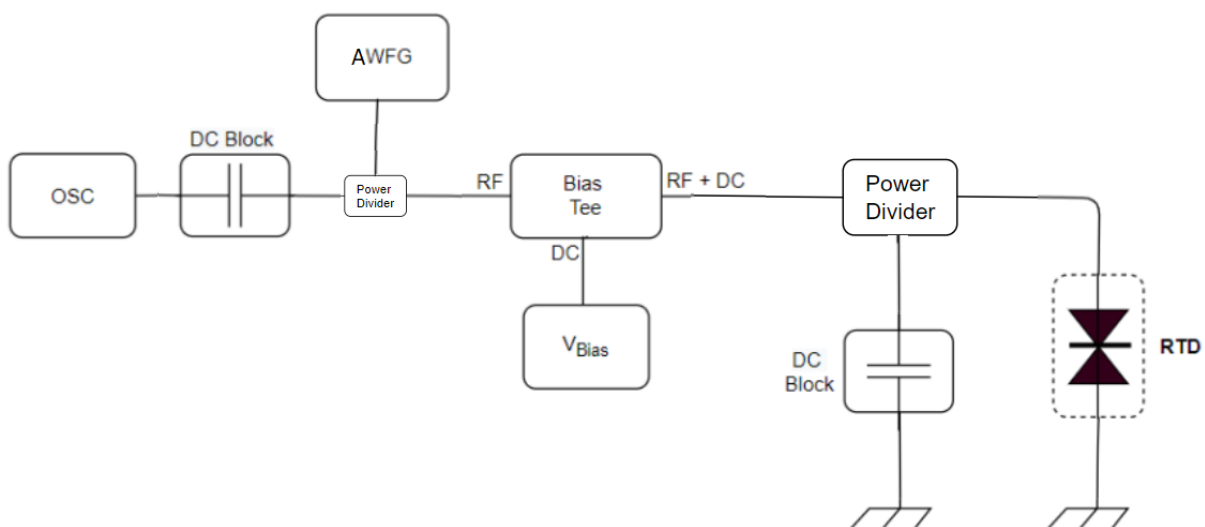


Figure 4.10: Experimental setup used to study the spiking properties of the RTDs.

The AWFG was added with a power divider (Tectronix Power Divider AM56113) in order to si-

4. METHODS

multaneously observe in the scope the disturbance signal and then the generated spike, as illustrated in figure 4.13. Adding the power divider means that both the disturbance pulse and the action potential of the spike are to half of their actual value. The power supply biases the RTDs on the intended operation points (peak and valley regions) being them positive or negative (forward or reverse bias) and the AWFG sends the disturbance signal. With the tools mentioned above there are several analysis that can be conducted on the spiking generation properties of the RTDs.

The first analysis that was performed was to simply ascertain the ability of the RTDs to produce spikes. This consisted in making the RTD produce a single spike and characterizing it for each of the bias points and devices. Then, a study on the properties of the produced spikes, namely their peak to peak amplitudes and periods was performed.

After this, a study on the voltage threshold of the RTDs for the experimentally determined peak and valley bias points, defined by the I-V curves, was performed.

Another experimental activity that was performed consisted in using set pulses for every RTD in order to infer the minimum and maximum bias voltages that can be applied and still produce a spike for given pulse amplitudes and widths, this was performed in order to have well set bias points that serve as references for future studies.

Finally, the refractory times of the system were inferred for all of the bias points.

4.2.2 Generated Spikes Analysis

This experiment was performed in order to understand the characteristics of the spikes that are generated by each RTD at each bias point. For the two peaks pulses of ± 75 mV of amplitude and 1 ns of temporal width were applied, and for the valleys ± 350 mV. In order to have the system produce a single spike the bias voltage was then adjusted to the point where only one clear spike was identified.

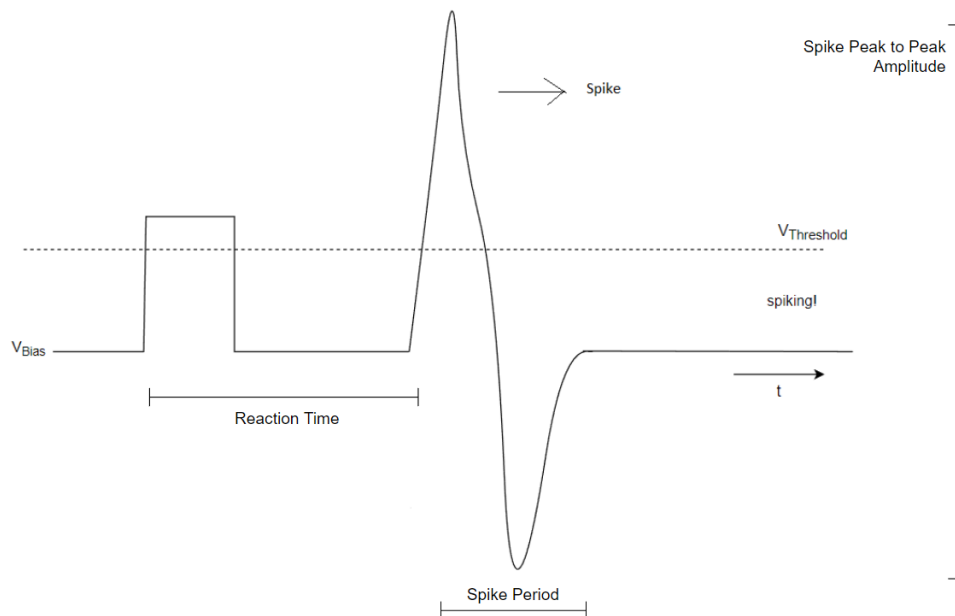


Figure 4.11: Illustration of the measured variables in the oscilloscope: the reaction time and the spike period and peak to peak amplitude.

After this the oscilloscope was used to measure a series of variables, such as, the response time of the RTD to the pulse, the temporal length of the spike (period) and the respective peak to peak amplitudes, as illustrated in figure 4.11.

4.2.3 Voltage Threshold

The voltage threshold is defined as the minimum amplitude of the disturbance pulse that still produces a spike, with this being said it should be mentioned that the voltage threshold depends on many parameters such as the DC bias applied to the RTD, the non-linearity of the I-V curve close to the NDC regions, the temporal width of the pulse, etc.

In figures 4.12 and 4.13 the basic concept behind this experiment is illustrated. One important thing that should be kept in mind is that a voltage threshold is always associated with a bias voltage, this means that biasing the RTDs in higher or lower points, that is, closer or farther away from their NDC regions, causes the voltage threshold to change.

In figure 4.12 the system is being disturbed by a pulse with an amplitude that is lower than its threshold, this means that the RTDs operation point does not enter its NDC region and the system does not produce an oscillation.

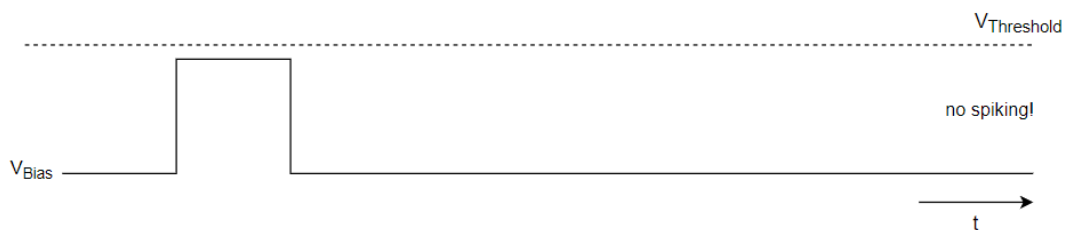


Figure 4.12: System being perturbed by a pulse with an amplitude below the voltage threshold. No spike is generated.

In figure 4.13 the case when the pulse on the bias voltage is higher than the threshold and a spike is produced.

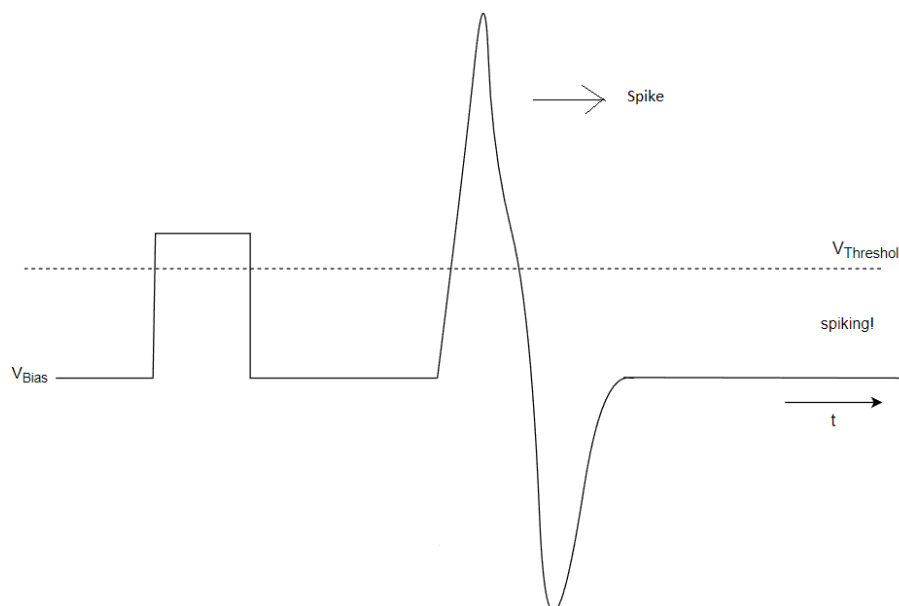


Figure 4.13: System being perturbed by a pulse with an amplitude higher than the voltage threshold of the bias point. A spike is produced.

In order to understand the dynamics of these points the voltage thresholds of the bias points defined in tables 5.1, 5.3, 5.2, 5.4 (peak and valley voltages) were inferred. The experiment consisted in using the power supply to bias the RTD on these points and then, pulses with 1 ns of width would be injected

4. METHODS

into the RTD using the AWFG. The amplitude of the pulse would then be increased until a spike was seen on the oscilloscope, as it is presented in figure 5.35 as an example for the $4.5 \mu\text{m}$ RTD.

4.2.4 Bias Voltage Analysis

In a similar sense as the voltage threshold, one can raise the bias voltage until the threshold is surpassed and a spike is formed, as it is illustrated in figure 4.14.

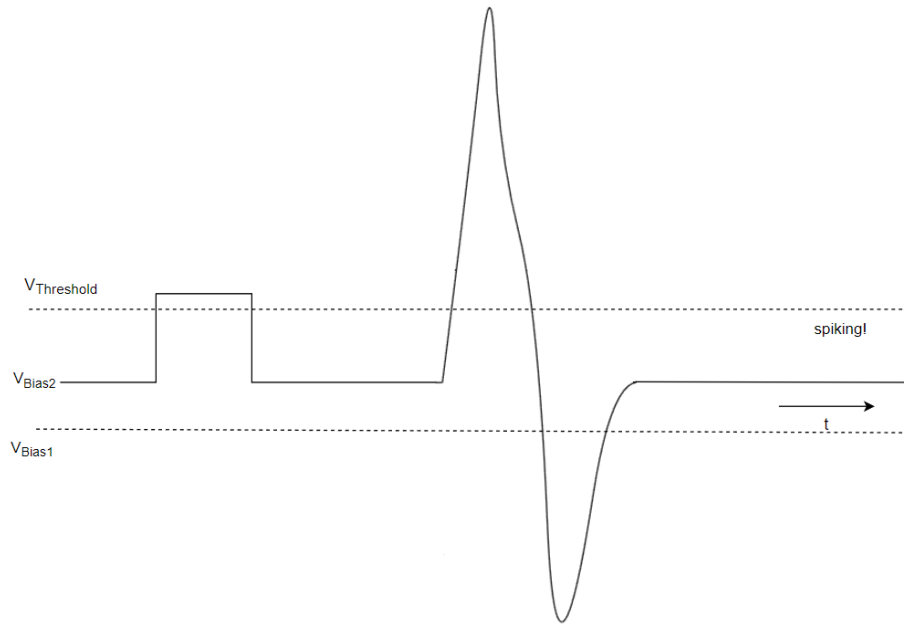


Figure 4.14: Illustration of how increasing the bias voltage can cause the RTD to produce a spike.

This time, pulses were applied to the RTDs. For the peaks two different amplitudes were chosen: 50 mV and 100 mV (−50 mV and −100 mV for the negative peak). For the valley pulses of ± 350 mV pulses were applied.

The experimental procedure consisted in applying the pulse amplitudes mentioned above with 1 ns of width using the AWFG. After this the bias voltage would be increased (or decreased) until the system responded with a spike, in the case of the peak the voltage was increased and in the case of the valley the voltage was decreased.

After this procedure was repeated for pulses with different pulse widths, for all of the peaks (DC bias on the peak regions) 0.5, 0.6, 0.7, 0.8, 0.9, 1, 2, 3, 4 and 5 ns widths and for all of the valleys (DC bias on the valley regions) pulses of 0.5, 1, 2.5 and 5 ns. Different pulse widths were used in order to characterize how the disturbance pulse width can influence the dynamics of spike generation of the different sized RTD.

4.2.5 Refractory Time

In figure 4.15 it is illustrated the case when the temporal separation between the pulses is not enough to produce two spikes, only one.

4.3 Simulation using MatLab's Simulink and Simscape

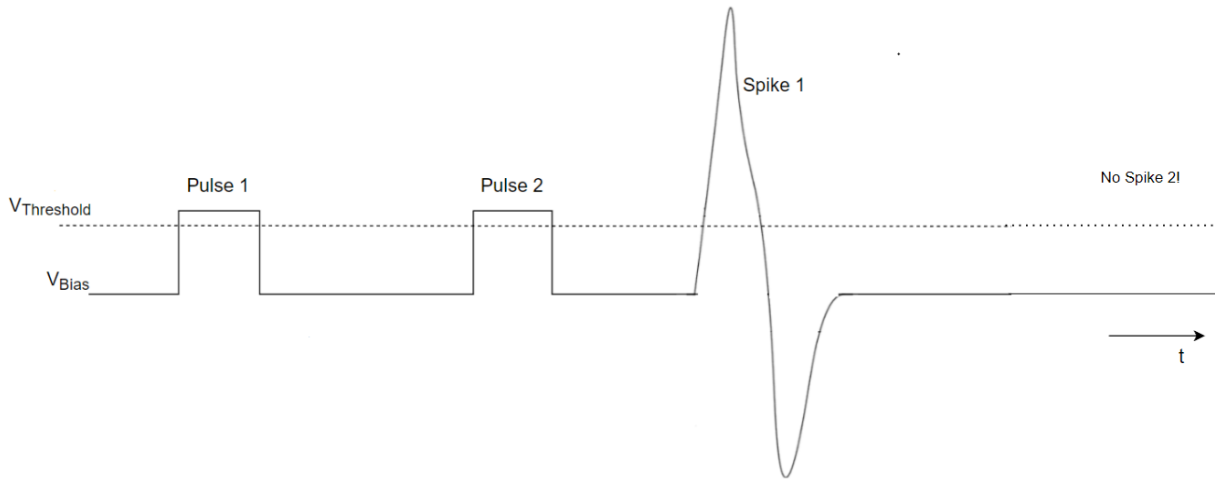


Figure 4.15: Illustration of the response of the system when the disturbance pulses are too close together (below the refractory time).

In figure 4.16 the pulses are far apart enough in order to allow the RTDs to produce two spikes.

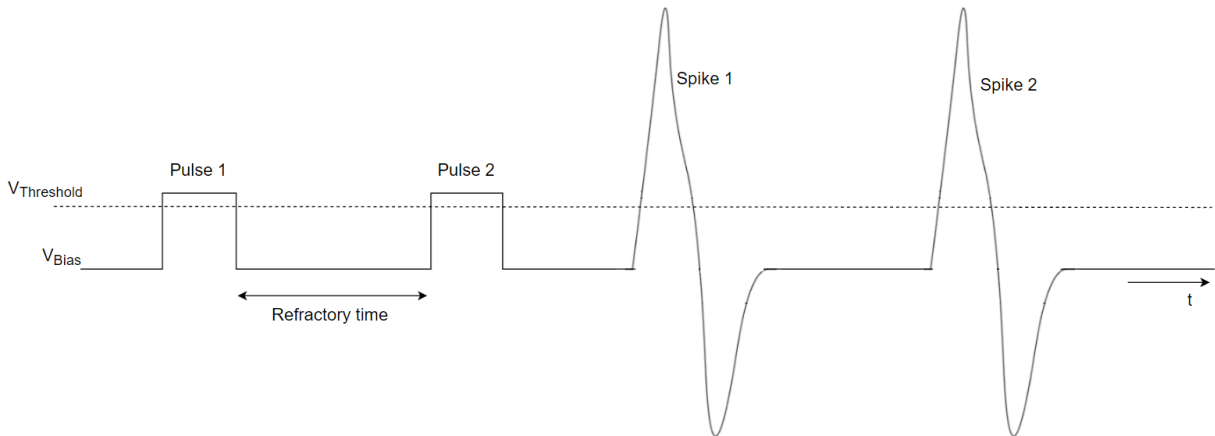


Figure 4.16: Illustration of the response of the system when the two disturbance pulses are temporally far enough to each one spikes individually.

The experimental procedure consisted in using the double pulse setting on the AWFG: two pulses with 50 mV and 100 mV of amplitude for the peak and ± 350 mV for the valley voltages, these pulses had 1 ns widths as well. After biasing the RTDs with the power supply with an appropriate voltage to perform this experiment, the distance between the pulses was shortened until the system stopped producing two individual spikes.

4.3 Simulation using MatLab's Simulink and Simscape

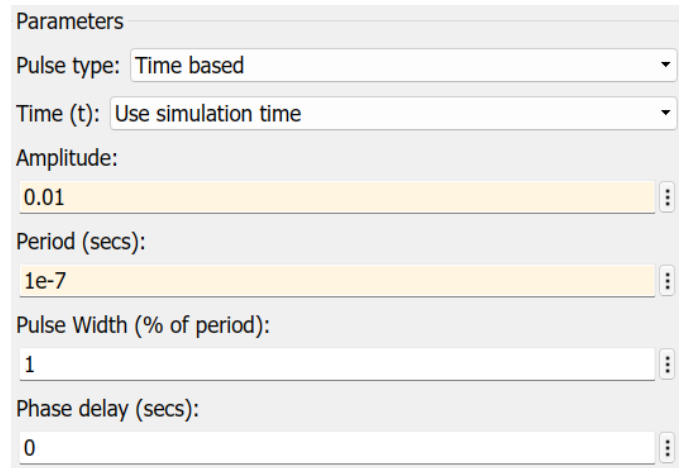
Using the basic AC signal equivalent circuit of a RTD presented in figure 3.8. A MatLab simulation package of the RTD was developed. Figure 4.18 shows the Simulink/Simscape implementation emphasizing the main elements and operations performed.

The simulator accepts as parameters the values of resistance, capacitance and inductance for the RLC circuit. For the RTD the I-V curve is defined by (Schulman et al. (1996)) physics based current voltage formula that is described by the coefficients of the current voltage characteristic: A, B, C, D, H, n1, n2 and M. It is important to differentiate the RTD capacitance with the parameter C used in Schulman's

4. METHODS

equation, so the capacitance of the RTD shall be referred to as C_{RTD} . The I-V curves and the simulation parameters used are presented in sections 5.4.1 and 5.4.2 of the results and discussion chapter.

Finally the last inputs consist of the DC bias voltage and the parameters of the pulse parameters (time, width and voltage amplitude) that were employed in order to investigate/infer the neuromorphic property of excitability of the circuit. The parameters that can be manipulated for the pulse generator are presented in figure 4.17.



The image shows a 'Parameters' dialog box for a pulse generator. It contains the following settings:

- Pulse type: Time based
- Time (t): Use simulation time
- Amplitude: 0.01
- Period (secs): 1e-7
- Pulse Width (% of period): 1
- Phase delay (secs): 0

Figure 4.17: Parameters that can be changed in the pulse generator.

In order to analyse the excitability of these RTDs in both the peak and valley regions, it is important to have in mind that when using the peak regions as an operation point the I-V characteristic used needs to be the one obtained in the ascending fit, while for the valley regions it needs to be the descending. So the first step is to extract the I-V curves of these devices, in this dissertation only the forward bias was considered.

The work that was developed using this simulator consisted first in studying the waveforms of the six RTDs when biased in their NDC regions.

The voltage dependent current source that represents the current voltage characteristic was constructed using an embedded Matlab function, a voltage sensor measures the voltage on the terminals of the capacitor and applies it to the current voltage characteristic equation that then injects the current via a controlled current source. The resistor, inductor and capacitor are components present in the Simscape package and one only needs to set their values.

4.3 Simulation using MatLab's Simulink and Simscape

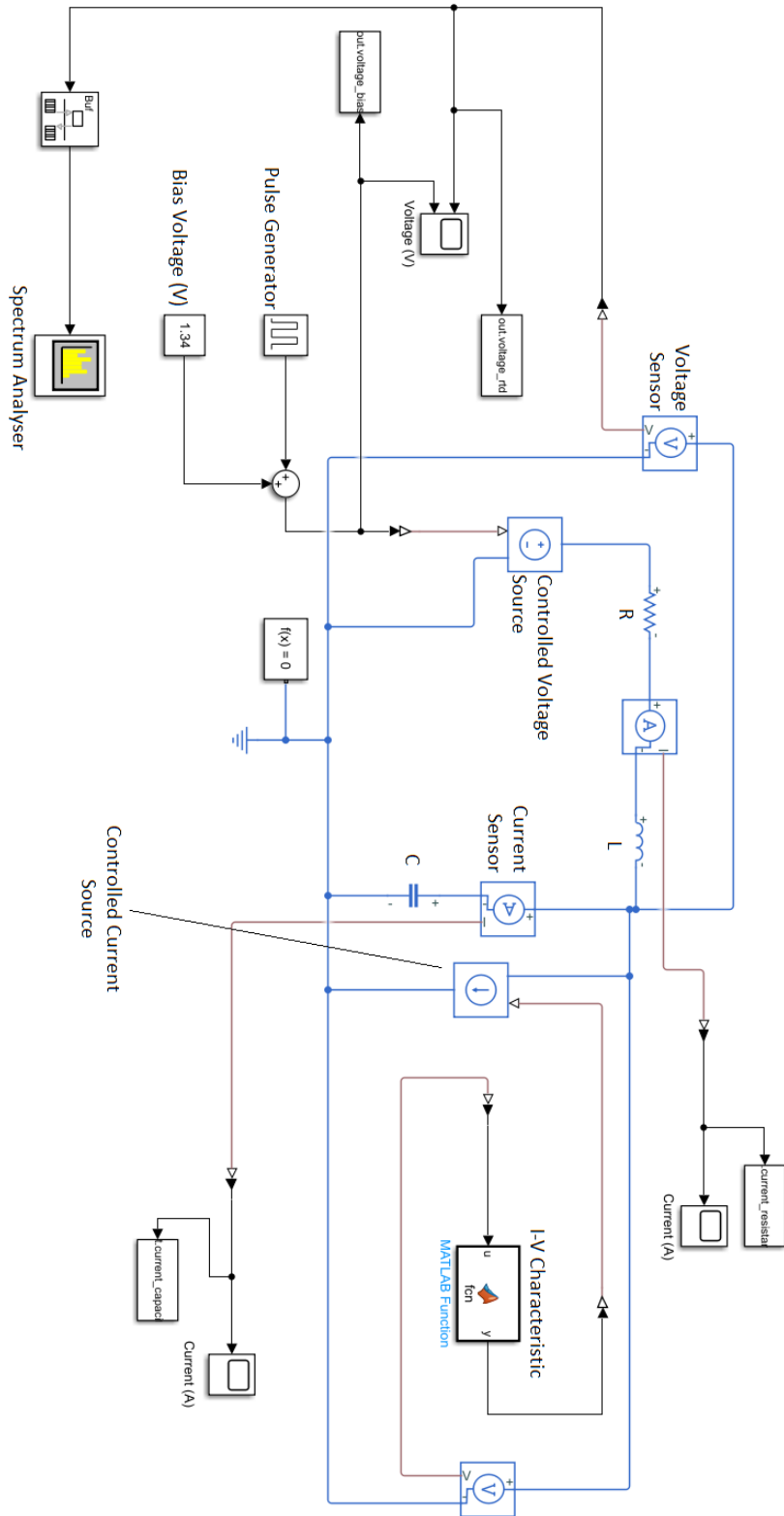


Figure 4.18: Simulink/Simscape simulation of the basic equivalent circuit for a DC biased RTD.

Chapter 5

Results and Discussion

In this chapter the results and discussion of the methods described in chapter 4 are put forward. First a DC characterization of the devices where the I-V curves of the devices are presented, followed by the respective curve fitting results. Then, the characterization of the NDC region of the RTDs by the study of the self-oscillations of the RTD. After this the spiking dynamics of the RTDs are put forward where the characteristics of the generated spikes, the voltage thresholds and the refractory times are presented and discussed. Finally, the results of the Simulink/Simscape simulator that uses the curves obtained from the fitting of (Schulman et al. (1996)) equation are shown and discussed as well.

5.1 Characterization of the Devices

The sourcemeter extracted the curve presented in figure 5.1, for the $4.5 \mu\text{m}$ radius RTD when under a reverse bias. This image is presented here as an example of what the sourcemeter measures.

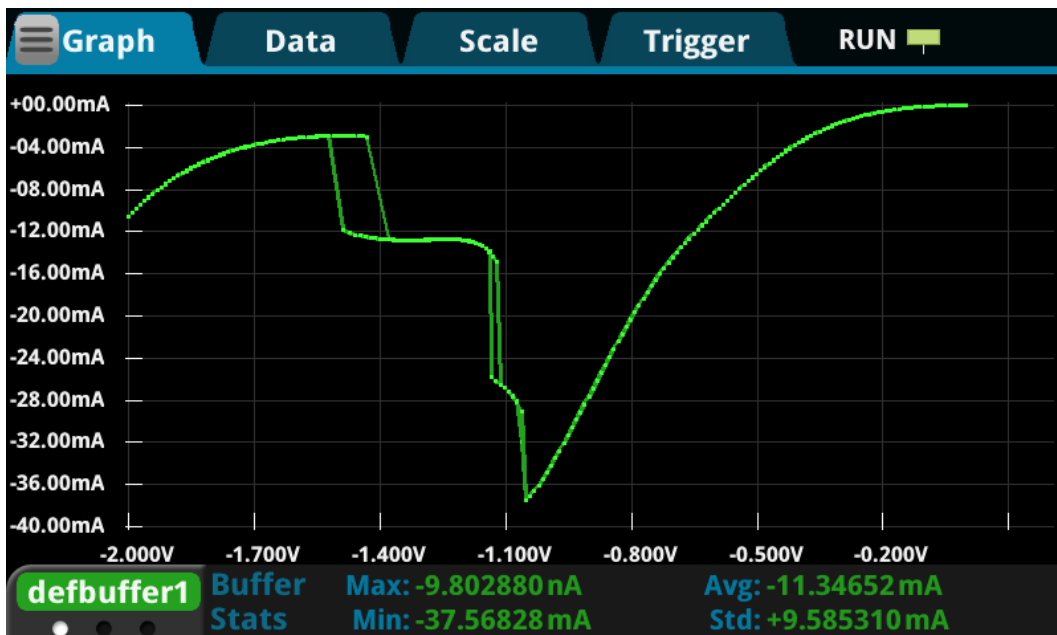


Figure 5.1: Current voltage characteristic print taken form the sourcemeter for the $4.5 \mu\text{m}$ radius RTD under reverse bias.

The curve at first glance seems to have the expected behaviour, two clearly visible PDC regions and exhibiting a characteristic plateau like behaviour and hysteresis in the NDC. This plateau like behaviour

5. RESULTS AND DISCUSSION

and hysteresis is still a controversial issue, with some authors claiming that is a fundamental property of the epilayer structure and others saying that is due to the experimental setup used.

A not so well defined NDC region is visible due to the fact that the DC nature of the measuring device (sourcemeter) and the fact that it is unable to measure the AC signal that is being produced, so it presents the sudden "jumps" presented in figure 5.1.

The I-V characteristics obtained for the RTD under forward bias are displayed in figures 5.2 5.3 for the ascend and descend respectively.

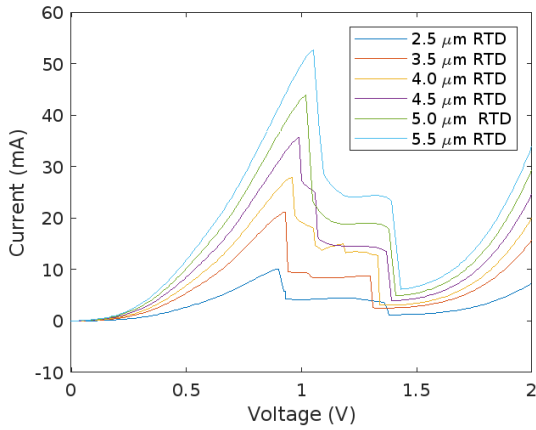


Figure 5.2: Current voltage characteristics for the six RTD under a forward voltage bias with a 0 to 2V sweep.

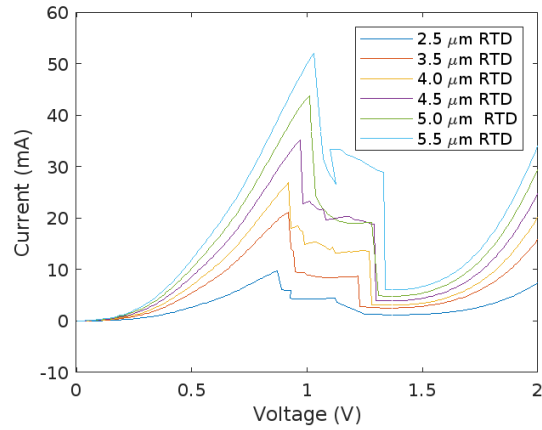


Figure 5.3: Current voltage characteristics for the six RTD under a forward voltage bias with a 2 to 0V sweep.

There is a clear scaling up on the total current passing through the devices with a bigger area, this is visible in both the ascent and descent. There may not be a clear difference between figures 5.2 and 5.3 but, as mentioned before a separate analysis needs to be done. These plots also hint that the peak and voltage move to higher voltages as the area of the device increases.

As for the reverse bias the curves are shown in figures 5.4 and 5.5 for the ascend and descend respectively.

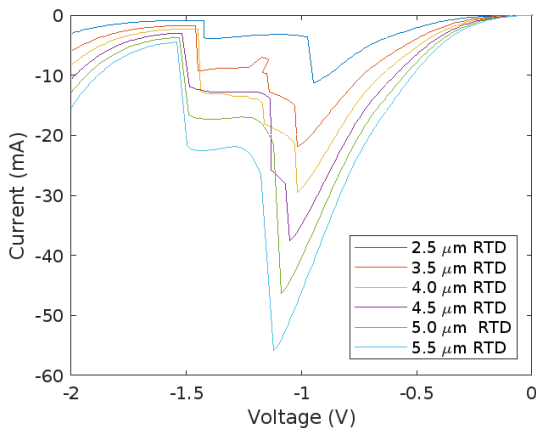


Figure 5.4: Current voltage characteristics for the six RTD under a reverse voltage bias with a 0 to -2V sweep.

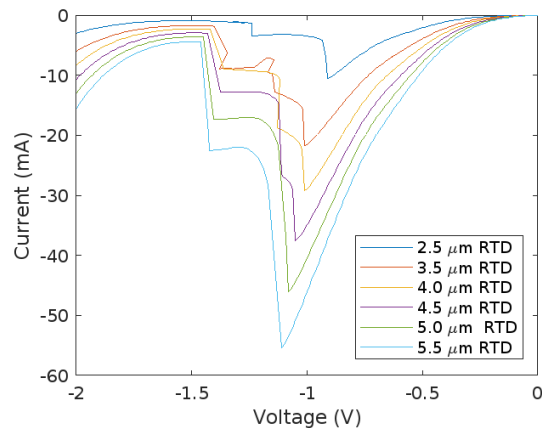


Figure 5.5: Current voltage characteristics for the six RTD under a reverse voltage bias with a -2 to 0V sweep.

In both figures 5.2 and 5.4 the three regions of the current voltage characteristics discussed in 3 are noticeable. In both the forward and reverse bias regions a first PDC region is present on all RTDs. Then,

5.1 Characterization of the Devices

when the bias voltage is increased even further a sharp decrease in current is identified, this corresponds to the second region, the NDC region. Between the first PDC and the NDC region lies the peak current I_{Peak} and its corresponding peak voltage V_{Peak} .

When the bias voltage is increased even further the current will reach a minimum, the valley current I_{Valley} , and beyond that point start rising again, this third region corresponds to the second PDC. All peak and valley currents and voltages, as well as their ratios are summarized in tables 5.1 and 5.2 for the forward and reverse bias RTD respectively in the ascend sweep. For the descend the same variables are shown in tables 5.3 and 5.4.

RTD Radius (μm)	I_{Peak} (mA)	I_{Valley} (mA)	PVCR	V_{Peak} (V)	V_{valley} (V)	Voltage Window (V)
2.5	10.85	1.21	9.78	0.90	1.38	0.48
3.5	21.18	2.55	8.31	0.93	1.31	0.38
4	27.94	3.06	9.13	0.96	1.33	0.37
4.5	35.65	3.92	9.09	0.99	1.39	0.4
5	43.85	4.86	9.02	1.02	1.41	0.39
5.5	52.58	6.17	8.52	1.05	1.43	0.38

Table 5.1: Peak/valley currents and voltages expressed in mA for each of the RTD's with a forward bias and respective ratio's in the ascend.

The ratio of the peak to valley current seems to maintain a somewhat constant value (around 9). The value seems to decrease as the area of the device increases in this case. The peak to valley voltage window seems to decrease as the area of the device increases.

RTD Radius (μm)	I_{Peak} (mA)	I_{valley} (mA)	PVCR	V_{Peak} (V)	V_{valley} (V)	Voltage Window (V)
2.5	-11.30	-0.98	11.53	-0.95	-1.42	0.47
3.5	-21.89	-1.76	12.43	-1.02	-1.46	0.44
4	-29.44	-2.34	12.58	-1.02	-1.45	0.43
4.5	-37.51	-2.98	12.59	-1.05	-1.52	0.47
5	-46.37	-3.69	12.57	-1.09	-1.53	0.44
5.5	-55.87	-4.47	12.50	-1.12	-1.54	0.42

Table 5.2: Peak/valley currents and voltages for each of the RTD's with a reverse bias and respective ratio's in the ascend.

In this case, as opposed to what was seen in the forward bias case, the peak to valley current ratio seems to increase as the area of the device increases having a slightly higher value of around 12. In this scenario the peak to valley voltage window presents slightly higher values than with forward bias. The same behaviour is seen though: as the area of the device increases this value decreases.

RTD Radius (μm)	I_{Peak} (mA)	I_{valley} (mA)	PVCR	V_{Peak} (V)	V_{valley} (V)	Voltage Window (V)
2.5	9.72	1.19	8.17	0.87	1.38	0.51
3.5	20.92	2.52	8.30	0.91	1.36	0.45
4	26.37	3.04	8.67	0.91	1.36	0.45
4.5	35.13	3.90	9.01	0.97	1.36	0.39
5	43.73	4.80	9.11	1.01	1.36	0.35
5.5	51.93	6.02	8.63	1.03	1.38	0.35

Table 5.3: Peak/valley currents and voltages for each of the RTD's with a forward bias and respective ratio's in the descend.

5. RESULTS AND DISCUSSION

When under a forward decreasing bias voltage the peak to valley current ratio lies around 8 – 9. It is important to note that this ratio is somewhat smaller than the ratio in the ascend case with the exception of the 5.5 μm RTD that has the same ratio. The peak to valley voltage window has the same behaviour as in the forward bias ascend, expect for the 3.5 μm RTD that presents a higher value. In the descend the scaling down of this value is even more present with the increase of the area.

RTD Radius (μm)	I_{Peak} (mA)	I_{valley} (mA)	PVCR	V_{Peak} (V)	V_{valley} (V)	Voltage Window (V)
2.5	-10.59	-0.89	11.90	-0.91	-1.51	0.6
3.5	-21.79	-1.74	12.52	-1.01	-1.50	0.49
4	-29.27	-2.30	12.72	-1.01	-1.49	0.48
4.5	-37.57	-2.95	12.74	-1.05	-1.49	0.44
5	-46.11	-3.63	12.70	-1.08	-1.49	0.41
5.5	-55.45	-4.41	12.57	-1.11	-1.49	0.38

Table 5.4: Peak/valley currents and voltages for each of the RTDs with a reverse bias and respective ratio's in the descend.

In a similar sense to what was seen in the descend before, the peak to valley current ratio is higher in the descend than in the ascend with values around 12. The peak to valley voltage window is different between the 2.5 μm and the 5.5 μm RTD with values ranging from 0.6 to 0.38 respectively. This asymmetry in the current voltage-characteristic is caused by asymmetry in the epilayers presented in figure 4.1 caused by the etch stop InP layer (layer 2).

The densities of current when under a forward bias for all of the RTDs are presented in figure 5.14 for the ascend and 5.18 for the descend.

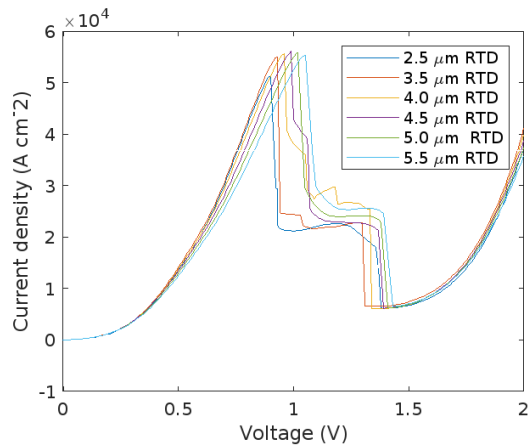


Figure 5.6: Density of current as a function of the bias voltage for all of the RTDs in the ascend.

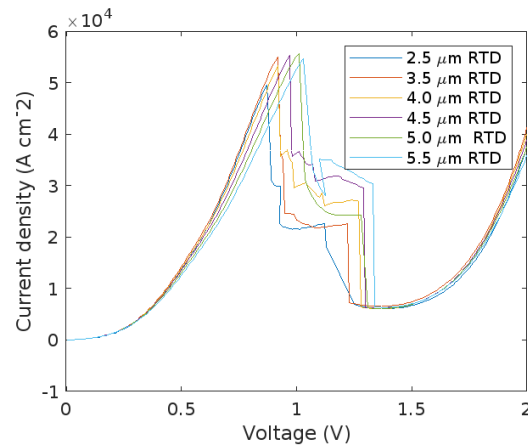


Figure 5.7: Density of current as a function of the bias voltage for all of the RTDs in the descend.

These plots indicate that the density of current that these devices present have a maximum for the 4 μm and 4.5 μm RTD, starting from the 2.5 μm RTD one can tell that as the area of the device increases all the way to the 4.5 μm RTD that the density of current also rises, then, it lowers slightly for the 5 μm and 5.5 μm RTDs. This phenomenon is present in both the ascend and descend for the RTDs under a forward bias. In these figures, 5.14 and 5.18, one thing that can be seen even more evidently than in figures 5.2 and 5.3 is the shift of the peak voltage to the right, to higher bias voltages.

In the reverse bias case, the densities of current are presented in figures 5.16 and 5.20 for the ascend and descend respectively.

5.1 Characterization of the Devices

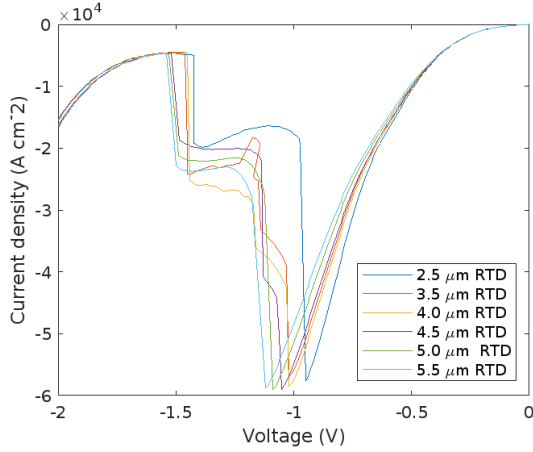


Figure 5.8: Density of current as a function of the bias voltage for all of the RTDs in the ascend.

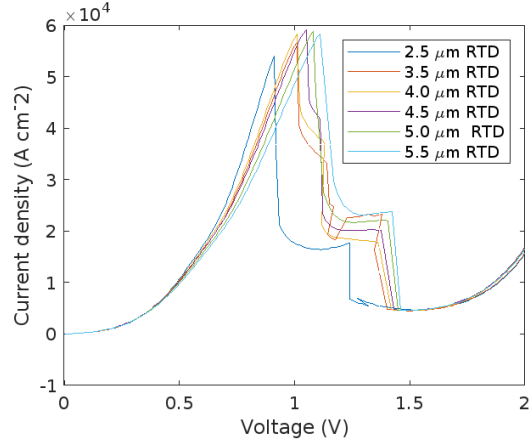


Figure 5.9: Density of current as a function of the bias voltage for all of the RTDs in the descend.

Like in figures 5.14 and 5.18 one can tell that there is a peak density current for the $4.5 \mu\text{m}$ RTD, this implies that this behaviour is present in all of the RTDs working either under a forward bias or a reverse bias. As for the shift in voltage, under a reverse bias the peak voltage this time shifts to the left, also towards higher bias voltages, with the scaling up of the device.

These plots presented above: figures 5.14, 5.18, 5.16, 5.20 are the ground work for the validation of the curve fitting software developed in order to be able to use the I-V in the numerical simulations. This means that the curve fitting model results need to have these behaviours presented above.

5.1.1 Curve Fitting Software for the Characterization of the RTDs

The results for the curve fitting of the experimental current voltage characteristics using equation 5.1 are presented in this section. The curve fitting plot results for the $4.5 \mu\text{m}$ radius RTD are presented in figures 5.10 and 5.12, as an example, for the forward and reverse bias RTDs respectively (ascending part of sweep). The rest of the curve fitting plots are shown in the annexes chapter in Annex A.

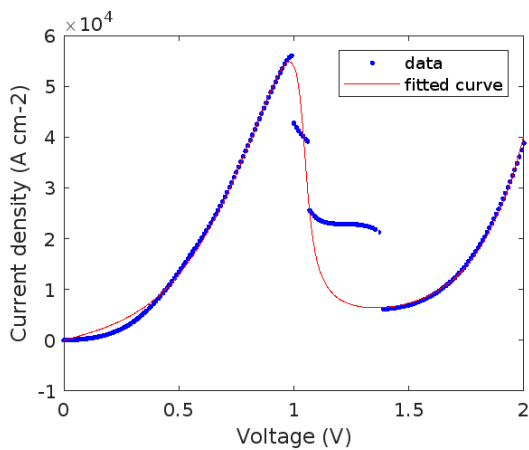


Figure 5.10: Plot of the experimental data and curve fit of the $4.5 \mu\text{m}$ radius RTD current voltage curve when forward bias is applied in the ascend. The curve fitting coefficients are: $A = 1.159 \times 10^4 \text{ A} \cdot \text{cm}^{-2}$, $B = 0.04978 \text{ V}$, $C = 0.1362 \text{ V}$, $D = 0.004599 \text{ V}$, $H = 2.949 \text{ A} \cdot \text{cm}^{-2}$, $n_1 = 0.1303$, $n_2 = 0.1224$.

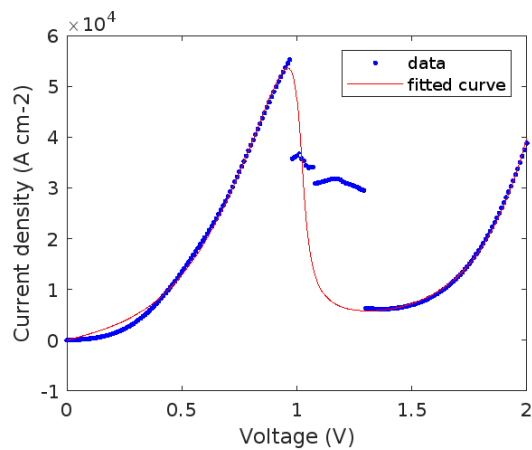


Figure 5.11: Plot of the experimental data and curve fit of the $4.5 \mu\text{m}$ radius RTD current voltage curve when a forward bias is applied in the descend. The curve fitting coefficients are: $A = 1.216 \times 10^4 \text{ A} \cdot \text{cm}^{-2}$, $B = 0.04459 \text{ V}$, $C = 0.1327 \text{ V}$, $D = 0.003917 \text{ V}$, $H = 5.205 \text{ A} \cdot \text{cm}^{-2}$, $n_1 = 0.1302$, $n_2 = 0.115$.

5. RESULTS AND DISCUSSION

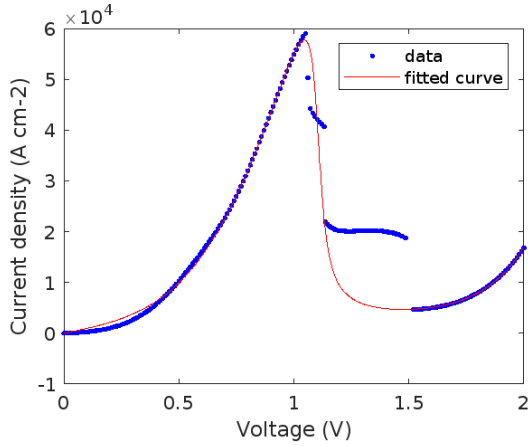


Figure 5.12: Plot of the experimental data and curve fit of the $4.5 \mu\text{m}$ radius RTD current voltage curve when a reverse bias is applied in the ascend. The curve fitting coefficients are: $A = 1.281 \times 10^4 \text{ A} \cdot \text{cm}^{-2}$, $B = 0.04576 \text{ V}$, $C = 0.1425 \text{ V}$, $D = 0.003802 \text{ V}$, $H = 0.5193 \text{ A} \cdot \text{cm}^{-2}$, $n_1 = 0.1289$, $n_2 = 0.1324$.

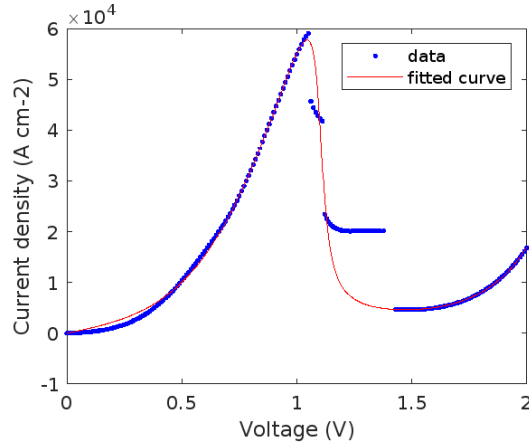


Figure 5.13: Plot of the experimental data and curve fit of the $4.5 \mu\text{m}$ radius RTD current voltage curve when a reverse bias is applied in the descend. The curve fitting coefficients are: $A = 1.34 \times 10^4 \text{ A} \cdot \text{cm}^{-2}$, $B = 0.04303 \text{ V}$, $C = 0.1396 \text{ V}$, $D = 0.003635 \text{ V}$, $H = 0.5685 \text{ A} \cdot \text{cm}^{-2}$, $n_1 = 0.265$, $n_2 = 0.1313$.

The first validation method of the curve fitting algorithm is to directly compare the experimental data (blue points) with the resulting fitted curve (red line) on all of the scenarios: under a forward and reverse bias in both the ascend and descend. When inspected visually, all of the curve fitting results seem to be accurate to the experimental data: both PDC regions seem to be well covered by the resulting curve.

Initially, the curve fitting models for most of the RTDs were overfitting, that is, they would perfectly cover both PDC regions but the peak would overextend to higher currents and bias voltages. This issue comes due to the fact that the NDC regions are not being considered by the algorithm. By completely eliminating these points from the curves the model is not able to give a solid fit. The solution found to solve this issue was to consider one of the points on the NDR as valid, by using this method the resulting curve collapses to the data and gives a better result. Because of this constraint that was added in order to stop the algorithm from overfitting, a flaw is found: the model does not fully cover the peak voltages, this gives rise to smaller peak currents and voltages than the ones measured experimentally, as it can be seen in table B.1. Table B.1 was constructed using the functions from the models, that is, this is the same table as the ones presented in tables 5.1, 5.3, 5.2, 5.4 but for the models, the densities of current were multiplied by the respective areas and the peak and valley currents were inferred.

Comparing the experimental results of the valley voltage with the ones obtained by using the model a key difference is found although the value of the absolute value of the valley current stays the same without showing a specific tendency, the valley voltages seems to decrease in absolute value. For example, the valley voltages of the $2.5 \mu\text{m}$ radius RTD are all a bit far from the experimental valley voltages and this leads to disparate peak to valley voltage differences for this RTD.

Because of the decrease in absolute value of the peak currents there is also a decrease in the peak to valley current ratio's. Although the forward/reverse bias effect is still seen: RTDs under a reverse bias have higher peak valley current ratio's, the scaling of this ratio with the size of the device is not present.

Another way to evaluate the curve fitting results is to compare the current density curves calculated directly using the experimental data with the models that the algorithm produced. In figure 5.14 the current density measured on all RTDs for an increasing forward bias is presented on the right, in figure 5.15 all of the curve fitting model results are presented.

5.1 Characterization of the Devices

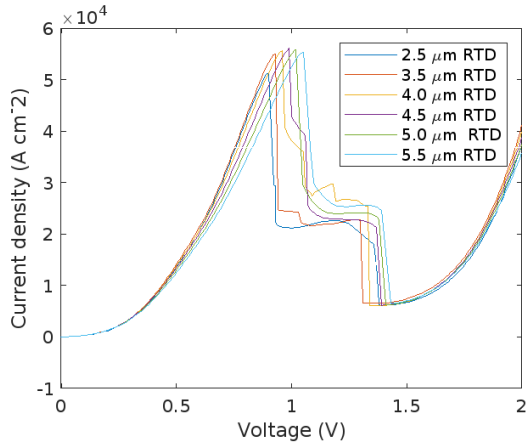


Figure 5.14: Density of current as a function of the bias voltage (forward) for all of the RTDs in the ascend.

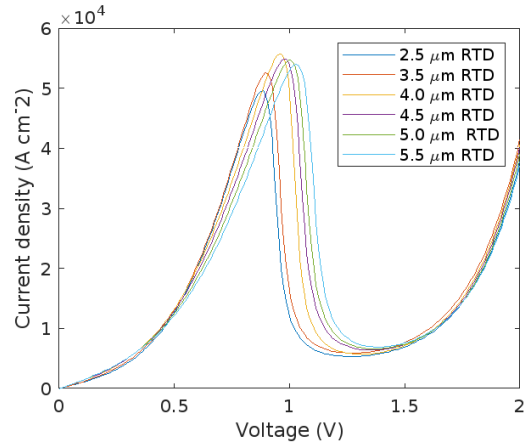


Figure 5.15: Curve fitting curves obtained for all of the RTDs for an increasing forward bias voltage.

The current voltage characteristics obtained using the algorithm all seem to have the same behaviours as the ones that are seen in the current densities calculated using the experimental data, with the exception of the 4 μm RTD that has a peak voltage that exceeds the 4.5 μm RTD. The peak voltage behaviour of the rest of the RTDs is the same as the experimental data: there is a scaling on the density of current until it reaches a maximum and then starts decreasing for the 5 μm and 5.5 μm RTD. As for the models behaviour on the valleys it seems to be quite disparate from the experimental data: in the plot on the left the 3.5 μm RTD is the first to reach its valley voltage followed by the 4 μm and then the 2.5 μm whereas in the plot on the right they come ordered with the size of the device.

In figures 5.16 and 5.17 the same images are presented but for the RTDs under a reverse bias.

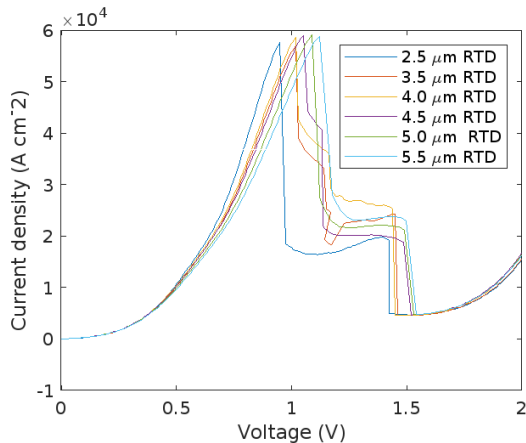


Figure 5.16: Density of current as a function of the bias voltage (reverse) for all of the RTDs in the ascend.

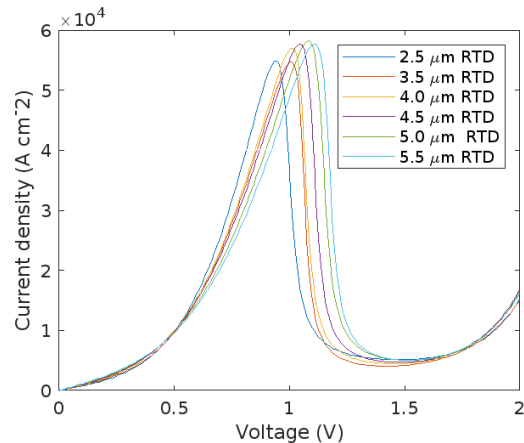


Figure 5.17: Curve fitting curves obtained for all of the RTDs for an increasing reverse bias voltage.

Comparing these two plots one can see that they show quite similar behaviours, from the already discussed scaling of the current density than then decreases for bigger RTDs to some small details on the peak voltages like the fact that the 2.5 μm radius RTD has a higher current density than the 3.5 μm radius RTD. Like before, the behaviour of the models concerning the valley region seems to differ from the one seen on the experimental data.

In figures 5.18 and 5.19 the density of current and curve fitting curves are presented for the case

5. RESULTS AND DISCUSSION

where the RTDs are under a decreasing forward bias voltage.

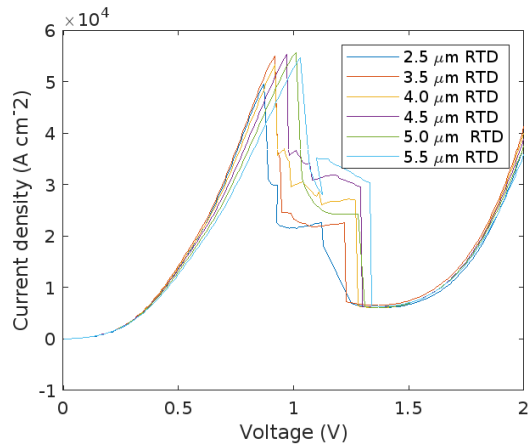


Figure 5.18: Density of current as a function of the bias voltage (forward) for all of the RTDs in the descend.

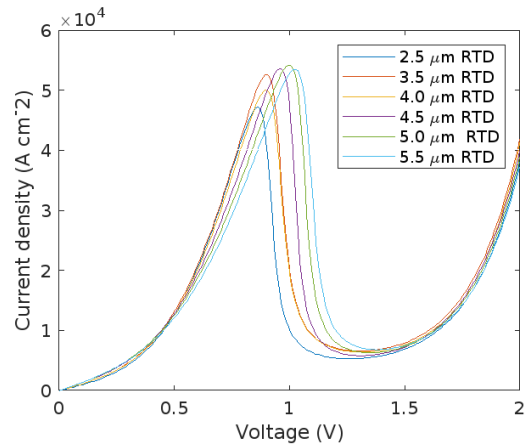


Figure 5.19: Curve fitting curves obtained for all of the RTDs for a decreasing forward bias voltage.

Analysing the peak voltage positions of these two plots it seems that they behave in similar ways again. In figures 5.20 and 5.21 the density of current and curve fitting curves are presented for the case where the RTDs are under a decreasing reverse bias voltage. In the example the same problem is found for the valley region, at least for the 2.5 μm RTD where it starts much further back.

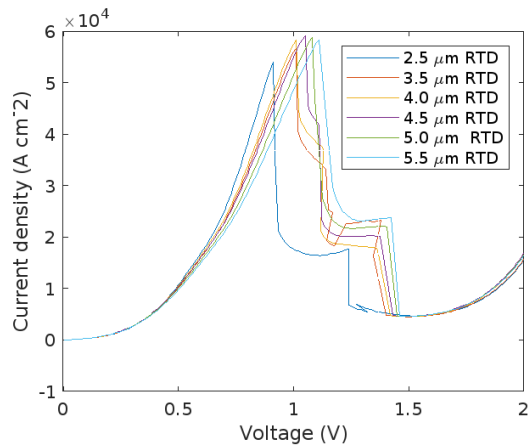


Figure 5.20: Density of current as a function of the bias voltage (reverse) for all of the RTDs in the descend.

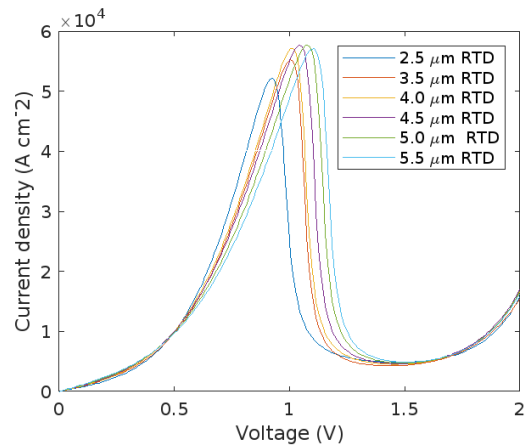


Figure 5.21: Curve fitting curves obtained for all of the RTDs for a decreasing reverse bias voltage.

Like before, it seems that the algorithm can produce around the peak region models that closely mimic the experimental. Whereas around the valley region some differences can be spotted.

These results are confirmation to what had already been discussed above when comparing the peak and valley currents/voltages. The peak voltages that were calculated using the model are much closer to the experimental voltages than the valley voltages. Although the behaviour of the models for the peaks seem to mimic that of the experimental data the behaviours on the valleys is different.

For the positive peaks the simulated peak current presents concordances of 90.8%, 95.47%, 99.71%, 97.9%, 97.97%, 95.53% for the 2.5 μm , 3.5 μm , 4 μm , 4.5 μm , 5 μm and 5.5 μm respectively. For the negative peaks it presents concordances of 95.49%, 96.3%, 97.42%, 97.89%, 98.58% and 98.17%. For

5.2 Voltage Controlled Oscillator

the positive valleys: 86.78%, 89.02%, 93.79%, 96.17%, 93.62% and 93.68%. And finally for the reverse bias: 97.96%, 88.07%, 95.73%, 97.32%, 92.95% and 92.62%.

The curve fitting algorithm seems to be able to fit most of the experimental peaks and valley currents with decent concordances. The concordances of the valley currents are smaller than the peak currents due to the fact that they are smaller in absolute value meaning that a slight deviation causes a huge disparity in the error.

5.2 Voltage Controlled Oscillator

The signals that returned to the oscilloscope for the RTDs are presented as examples in figures C.1, C.2, C.3, C.4, C.5 and C.6 for the bias voltages presented in the legends. The oscilloscope automatically measures the peak to peak voltage and the frequency of the signal.

5.2.1 Oscillation Waveforms

The waveforms on the oscilloscope took the forms presented in figures C.1, C.2, C.3, C.4, C.5 and C.6. The 5.5 μm , 5 μm , 4.5 μm and 4 μm RTDs present the slow-fast dynamics that was described in 3, a slow transition is followed by a fast transition in voltage upwards, followed by another slow downwards transition that suddenly drops (second fast transition) and finally rises slowly until it returns to its initial value. The waveform is similar to the one presented in figure 3.10. The effect of the $\sqrt{\frac{C}{L}}$ variable is also seen due to the fact that changing what varies in each RTD is the capacitance. Bigger devices, like the 5.5 μm for example have higher capacitance's that lead to higher $\sqrt{\frac{C}{L}}$ values, this causes the transitions to become slower when compared with the 4 μm RTD for example. The waveforms for the 2.5 μm and 3.5 μm RTDs do not follow this behaviour, they present a waveform similar to the one presented in figure 3.10, suggesting that they have a higher $\sqrt{\frac{C}{L}}$.

This might indicate that the oscillation that these two RTDs will present for spiking purposes will be more rounded, and less like a spike. Even so they were considered as isolated oscillations and the spiking experimental methods were executed on them.

5.2.2 Frequency Analysis

The frequency measured by the oscilloscope was plotted for all of the RTDs in every scenario: forward and reverse bias; ascend and descend.

The frequencies obtained when the RTDs are under a forward bias are presented in figures 5.22 and 5.23 for the ascend and descend respectively.

5. RESULTS AND DISCUSSION

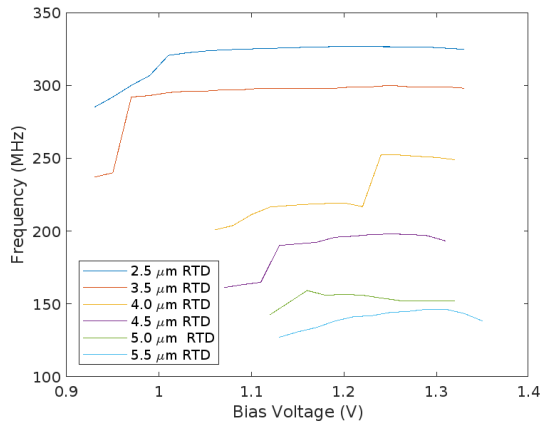


Figure 5.22: Frequency of oscillation of the RTDs as a function of the applied voltage in the ascend under a forward bias.

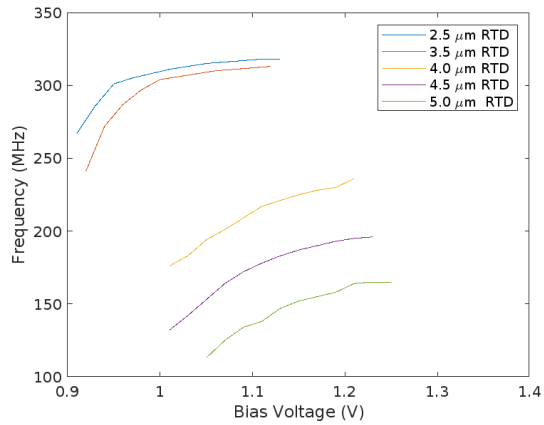


Figure 5.23: Frequency of oscillation of the RTDs as a function of the applied voltage in the descend under a forward bias.

The first thing that is noticed is that, in the ascend the RTDs have a much broader voltage span on which they oscillate. This can happen due to the fact that in this case, one is lowering the energy of the system to correspond to the resonant energy level of the DBQW, this means that there might be some stability issues with approaching this level from above than from below, this is most seen in the $2.5 \mu\text{m}$ and $3.5 \mu\text{m}$ RTDs where the voltage span is almost twice as large in the ascend than in the descend.

Another thing that is noted is that, on the ascend, the voltage span on which the RTDs oscillate is much higher for smaller RTDs, this can be understood with the data studied in table 5.1 where the peak to valley voltage difference is higher for devices with smaller areas. This behaviour is not seen on the descend, but as stated earlier the system seems to be less stable when trying to enter resonance from a higher energy state than from a lower energy state. Further more, it is also noted that the $5.5 \mu\text{m}$ radius RTD does not even present oscillation in the descend, the signal that the oscilloscope reads is presented in figure 5.24.

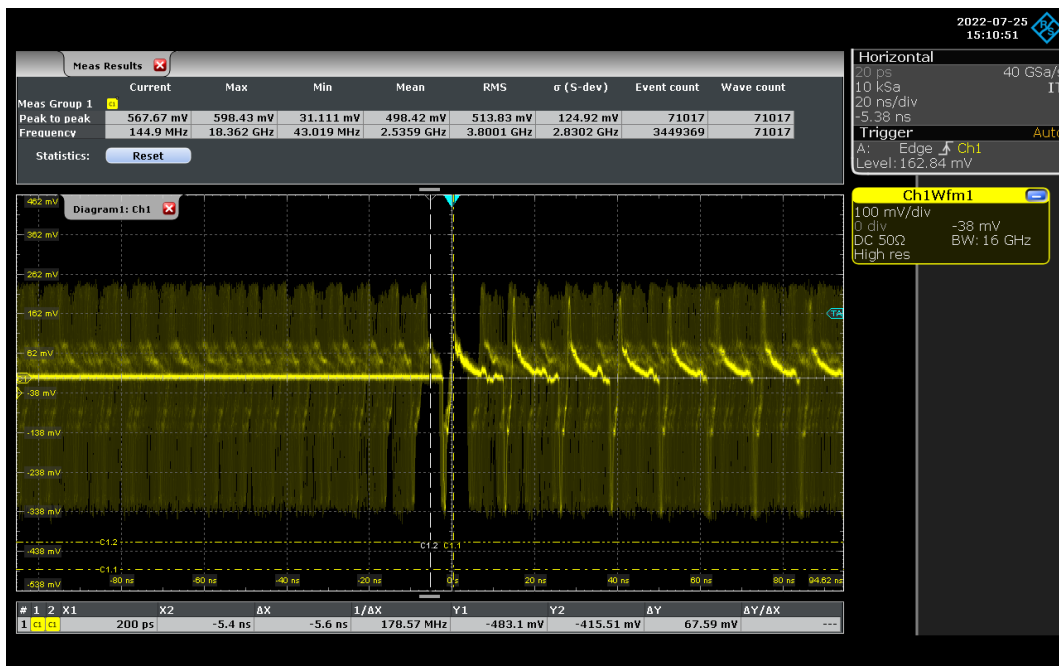


Figure 5.24: Waveform of the $5.5 \mu\text{m}$ RTD in the descend.

5.2 Voltage Controlled Oscillator

Like before, the frequencies obtained when the RTDs are under a reverse bias are presented in figures 5.25 and 5.26 for the ascend and descend respectively.

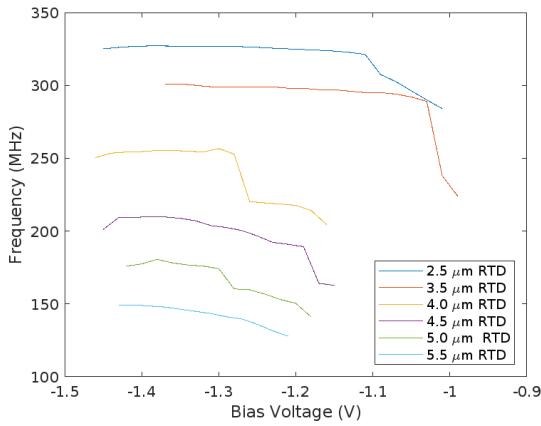


Figure 5.25: Frequency of oscillation of the RTDs as a function of the applied voltage in the ascend under a reverse bias.

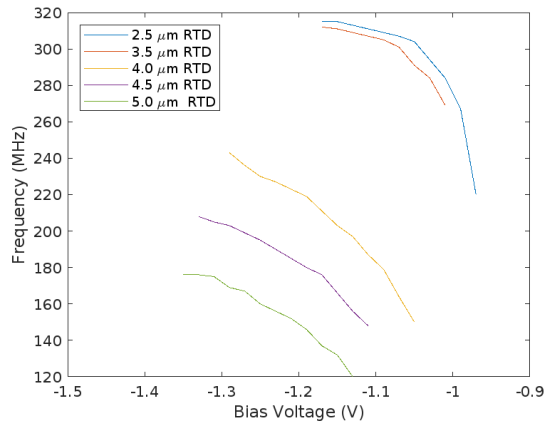


Figure 5.26: Frequency of oscillation of the RTDs as a function of the applied voltage in the descend under a reverse bias.

These plots seem to be the anti-symmetrical counterparts to the ones presented in figures 5.22 and 5.23, the same behaviour is seen: in the ascend smaller RTDs have a broader voltage span on where they oscillate. Again, in the descend the 5.5 μm RTD does not show stable oscillation.

The frequency at which the RTDs oscillate also seems to increase as the area of the device decreases, this can be understood with the help of figure 3.8. In this model, for the DC bias circuit, the RTD can be understood as a capacitor in parallel with a dependent current source that is in series with a parasitic inductance and resistance, this circuit is an RLC circuit that, when the RTD is biased in its NDC region, acts as a relaxation oscillator.

The capacitance for an infinite parallel plate capacitor can be estimated as $C = \epsilon_0 \frac{A}{d}$, where ϵ_0 corresponds to the permittivity of free space, A the cross sectional area of the device and d the distance between the plates. This means that the devices with smaller areas have a smaller capacitance that then lead to higher oscillation frequencies, and this is seen perfectly from figures 5.22 to 5.26 where there is a clear scaling of the frequency with the radius of the device.

5.2.3 Peak to Peak Amplitude Analysis

The peak to peak amplitudes obtained when the RTDs are under a forward bias are presented in figures 5.27 and 5.28 for the ascend and descend respectively.

5. RESULTS AND DISCUSSION

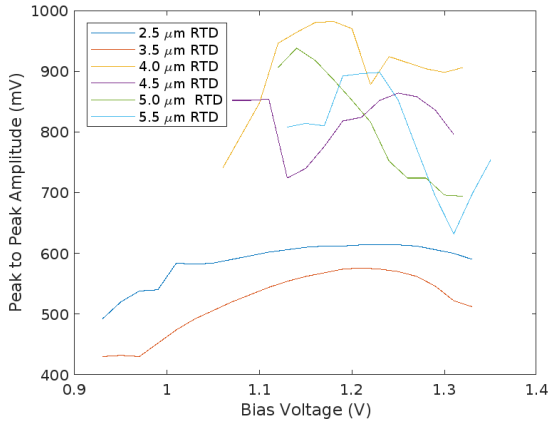


Figure 5.27: Peak to peak amplitude of oscillation of the RTDs as a function of the applied voltage in the ascend under a forward bias.

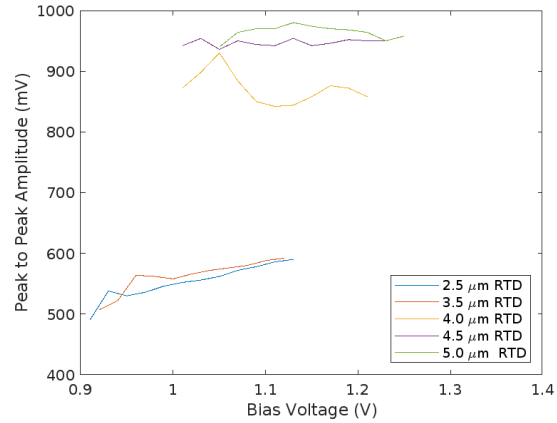


Figure 5.28: Peak to peak amplitude of oscillation of the RTDs as a function of the applied voltage in the descend under a forward bias.

The first thing that is noted from these plots is that there is not a clear relation between the size of the devices and their respective peak to peak amplitudes of oscillation for the $4 \mu\text{m}$, $4.5 \mu\text{m}$, $5 \mu\text{m}$ and $5.5 \mu\text{m}$ radius RTDs. Despite this fact it is seen that the $2.5 \mu\text{m}$ and $3.5 \mu\text{m}$ RTDs have a clearly lower amplitude of oscillation when compared with the $4 \mu\text{m}$, $4.5 \mu\text{m}$, $5 \mu\text{m}$ and $5.5 \mu\text{m}$ radius RTDs (about half). This behaviour can be partly explained with the use of tables 5.1 and 5.3 where the PVCRR should be the determining factor for the peak to peak amplitudes to be expected: higher peak to valley current ratios lead to higher oscillation amplitudes.

The peak to peak amplitudes obtained when the RTDs are under a reverse bias are presented in figures 5.29 and 5.30 for the ascend and descend respectively.

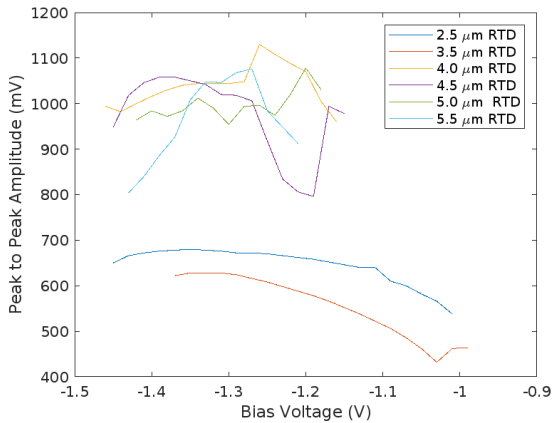


Figure 5.29: Peak to peak amplitude of oscillation of the RTDs as a function of the applied voltage in the ascend under a reverse bias. P2P vs Voltage reverse bias ascend.

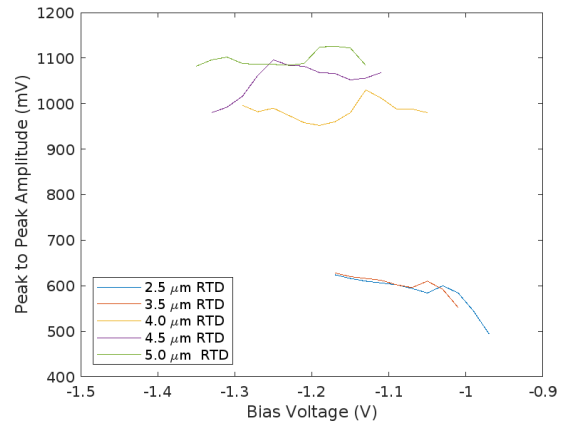


Figure 5.30: Peak to peak amplitude of oscillation of the RTDs as a function of the applied voltage in the descend under a reverse bias.

Like before, these graphics seem to be the anti-symmetrical counterparts of the ones presented in figures 5.27 and 5.28, but this time all RTDs seem to have slightly higher peak to peak amplitudes than when under a forward bias in both the ascend and descend. Going back to tables 5.2 and 5.4 one can state that the peak to valley current ratios are much higher when the RTDs are under a reverse bias than when the RTDs are under a forward bias, this can be seen in both the ascend and descend. This could mean that this value that can be inferred immediately after the extraction of the I-V characteristics can

help determine, for these type of devices that work both under forward and reverse bias, what bias could give higher peak to peak amplitudes.

5.3 Spiking

In this section the experimental spiking dynamics of circuits containing RTDs is put forward. The characterization of the generated spikes is first presented where the spikes amplitude, period and delay (with respect to the disturbance pulse) are analysed. After this, the voltage threshold and bias voltage analysis are presented and discussed. Finally, the measured refractory times of the RTDs are put forward and discussed as well.

5.3.1 Generated Spike Characteristics

The first analysis corresponds to the evaluation of the RTD response to a pulse perturbation/excitation.

Figure 5.31 shows a typical response of a $2.5 \mu\text{m}$ RTD, biased at the forward bias peak to a narrow electrical pulse (1 ns). The vertical and horizontal cursors allow the measurement of the time and voltage amplitude of the signals. This process was repeated for the other RTDs and bias points.

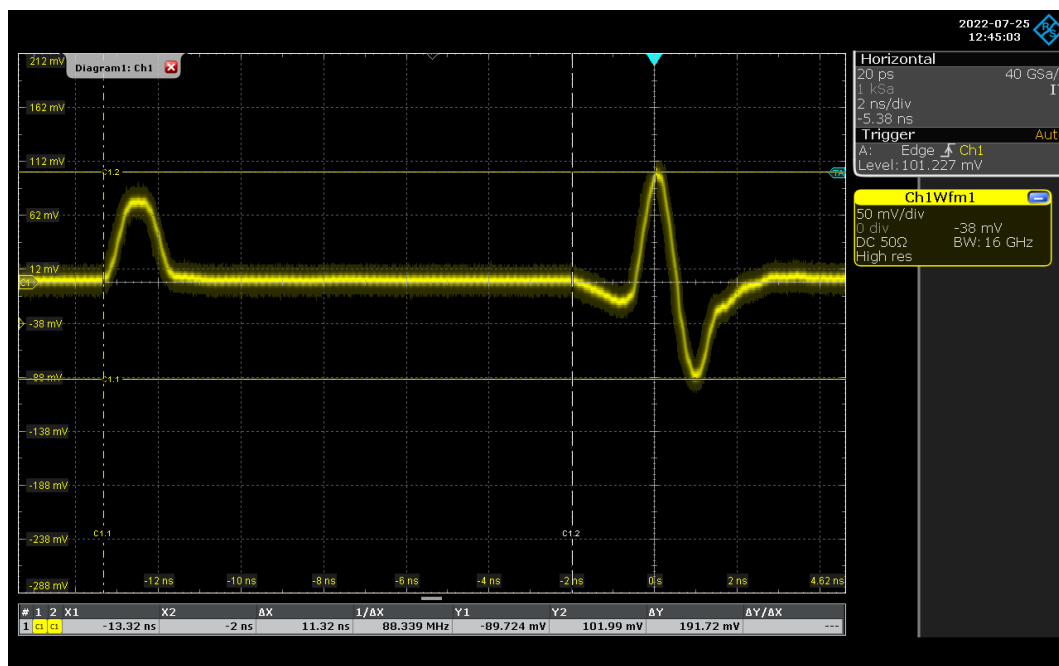


Figure 5.31: Waveform of the spike generated by the $2.5 \mu\text{m}$ RTD.

Some of the RTDs did not present a spike when biased in their valley regions, that is, they did not present an all-or-none response, the waveforms that were seen on the oscilloscope were similar to the one presented in figure 5.32.

5. RESULTS AND DISCUSSION

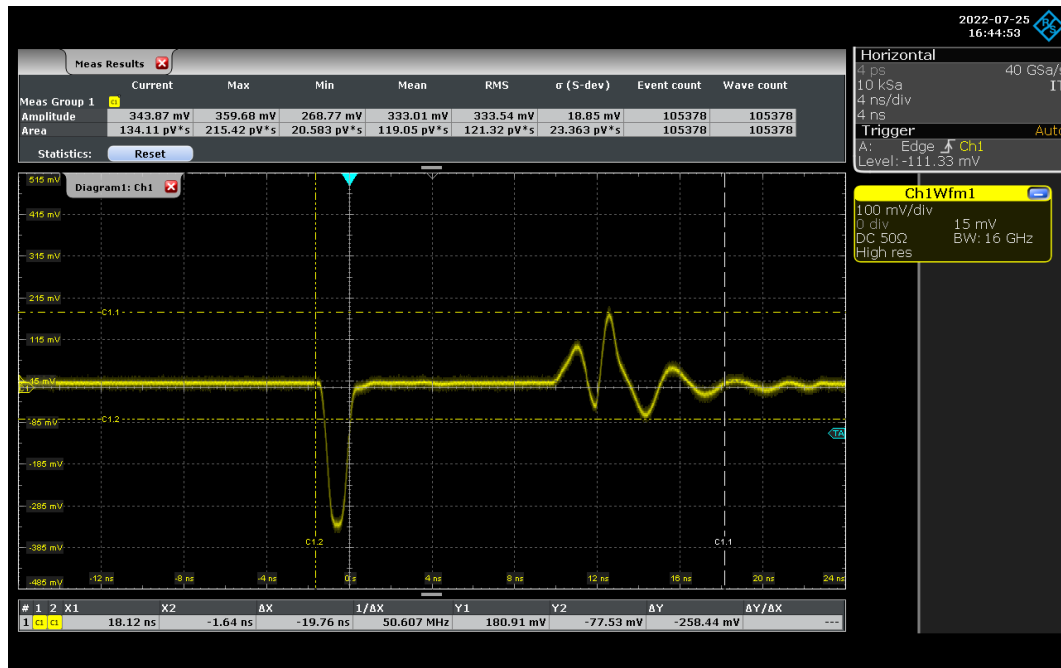


Figure 5.32: Waveform of the spike generated by the 2.5 μm RTD.

For the 2.5 μm and the 3.5 μm the spike is not well defined so they were not taken into account for this analysis.

The results obtained for the reaction time (delay time between the disturbance and the resulting spike), the period (temporal duration) of the spike and its peak to peak amplitude are presented in tables 5.5, 5.7, 5.6 and 5.8 for the forward bias peak and valley and reverse bias peak and valley respectively.

RTD radius (μm)	Reaction time (ns)	Spike Period (ns)	Peak to Peak Amplitude (mV)
2.5	11.3	4.6	191.72
3.5	11.2	4.96	203.22
4	11.2	6.44	385.74
4.5	11.3	7.8	414.88
5	11.1	8.6	438.65
5.5	11.4	9.9	454.75

Table 5.5: Spike analysis of the RTDs in the forward peak bias voltage. The reaction time corresponds to the elapsed time between the pulse and the generated spike. The spike period and peak to peak amplitude are the spike characteristics. These values are all for pulses with 1 ns of width and 75 mV of amplitude.

RTD radius (μm)	Reaction time (ns)	Spike Period (ns)	Peak to Peak Amplitude (mV)
2.5	11.32	4.9	231.59
3.5	11.34	4.9	242.4
4	11.36	7.0	440.95
4.5	11.6	7.8	487.73
5	11.84	9.8	513.8
5.5	11.9	10.8	535.27

Table 5.6: Temporal analysis of the RTDs in the reverse peak bias voltage. The reaction time corresponds to the elapsed time between the pulse and the generated spike. The spike wavelength and peak to peak amplitude are the spike characteristics. These values are all for pulses with 1 ns of width and -75 mV of amplitude.

RTD radius (μm)	Reaction time (ns)	Spike Period (ns)	Peak to Peak Amplitude (mV)
4	11.56	6.76	330.02
4.5	11.44	6.96	363.7
5	11.44	7.1	383.7
5.5	11.4	7.24	413.52

Table 5.7: Temporal analysis of the RTDs in the forward valley bias voltage. The reaction time corresponds to the elapsed time between the pulse and the generated spike. The spike wavelength and peak to peak amplitude are the spike characteristics. These values are all for pulses with 1 ns of width and -350 mV of amplitude.

RTD radius (μm)	Reaction time (ns)	Spike wavelength (ns)	Peak to Peak Amplitude (mV)
4	11.64	6.32	399.6
4.5	11.6	7.04	419.49
5	11.32	8.12	451.29
5.5	11.3	9	475.14

Table 5.8: Temporal analysis of the RTDs in the reverse bias voltage. The reaction time corresponds to the elapsed time between the pulse and the generated spike. The spike wavelength and peak to peak amplitude are the spike characteristics. These values are all for pulses with 1 ns of width and 350 mV of amplitude.

The first thing that is noted is that the peak to peak amplitude of the spikes is roughly half of the values of the peak to peak frequencies in the VCO happens due to the fact that a power divider has been added to the experimental setup. An interesting analysis that can be performed is to compare these values of amplitudes with the amplitudes obtained when characterizing the oscillating NDC region, to do this the amplitudes of the VCO were divided by two.

This comparison needs to be made on the edges of the NDCs closest to the bias points, that is, for the peaks its the amplitude that corresponds to the beginning of the of the NDC in the ascend and for the valleys its the beginning of the NDC region starting from a higher voltage. The pattern that is found is that the peak to peak amplitudes of the generated spikes are lower than the peak to peak amplitudes of the system when oscillating at a slightly higher bias point. With one exception, the $4 \mu\text{m}$ RTD reverse bias peak presents a spike that is bigger than its corresponding oscillation amplitude. In the same sense comparing the period of the waves of the VCO with the period of the generated spikes one can infer that the period of the spike is larger than the period of the oscillation on the corresponding NDC regions.

This decrease in spike amplitude and period when compared with the oscillation can be explained as follows: because we are disturbing the system only once into its unstable NDC point and then returning

5. RESULTS AND DISCUSSION

it to a stable point the system cannot produce an oscillation as coherent as when being continually in the unstable bias point.

When comparing the forward bias peaks with the reverse bias peaks one can see that the peak to peak amplitudes of the spikes under forward bias are lower than under a reverse bias, this goes in accordance with what was measured in the VCO analysis. As for the valleys the same thing is perceived, the forward bias spikes have smaller amplitudes than the reverse bias spikes.

In the $2.5 \mu\text{m}$ and $3.5 \mu\text{m}$ RTD when biased in their valley voltages, the spikes characteristics cannot be accurately measured due to the instability of the points, even so, it is still possible to differentiate whether the spike is being generated or not, so the voltage threshold measurements, the bias voltage analysis and the refractory time measurements can still be performed.

5.3.1.1 Elapsed Time

The reaction times (see figure 5.31 for a typical screenshot) for all of the RTDs stays the same, around 11.5 ns this can be easily understood. In order to understand the elapsed time between the stimulus and the spike the data-sheets of the cables were consulted, in the data-sheet it was stated that the cables have a 76% velocity of propagation. So, in order to understand the 11.5 ns value the lengths of all cables and connections were taken. The relevant cables and components physical lengths are indicated in the setup schematics in figure 5.33, referenced as numbers from 1 to 6, the corresponding lengths of the cables to the numbers are presented in table 5.9.

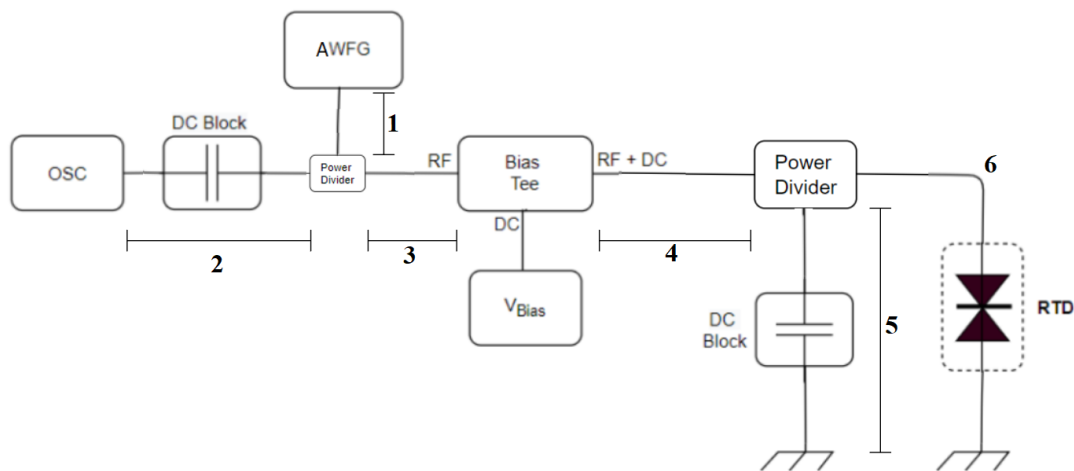


Figure 5.33: Experimental setup used to study the spiking properties of the RTDs with the lengths of the cables that are connecting the components

#	Cable Length (cm)
1	92
2	6
3	92
4	23
5	3
6	3

Table 5.9: Corresponding cables lengths of the numbers presented in figure 5.33.

The pulse goes through path 1 + 3 + 4 + 5 + 6 to reach the RTD and the generated spike 6 + 4 + 3 + 2, but it is important to mention that although the pulse travels all this distance it also needs to travel 1 + 2 to reach the oscilloscope, so the difference in timing will be given by the time the pulse takes to reach the RTD plus the time the spike takes to reach the oscilloscope minus the time the original spike takes to reach the oscilloscope, the total distance is given by: $1 + 3 + 4 + 5 + 6 + 6 + 4 + 3 + 2 - 1 - 2 = 239$ cm.

Because we have a 76% VoP this means that the speed on the electrons propagating through the cables is given by: $v = 0.76c = 2.28 \times 10^8 \text{ ms}^{-1} = 22.8 \text{ cmns}^{-1}$. The travel time can then be estimated to be $43.9 \text{ ps} \cdot \text{sm}^{-1}$. This implies that the theoretical temporal separation between the pulse and the spike is $\sim 10.5 \text{ ns}$, this goes in accordance with the elapsed times measured experimentally that are presented in tables 5.5, 5.6, 5.7, 5.8. The difference in times that is seen may be caused by the connectors and the other component's that the signal needs to cross.

5.3.2 Voltage Threshold

The voltage threshold of an excitable system consists in the minimum disturbance pulse amplitude that generates a spike, for these RTDs the voltage thresholds of the experimentally determined peak and valley bias voltages where inferred. In figures 5.34 and 5.35 the method that was described in figures 4.12 and 4.13 is presented for the $4.5 \mu\text{m}$ RTD, the bias voltages are shown in the legend.

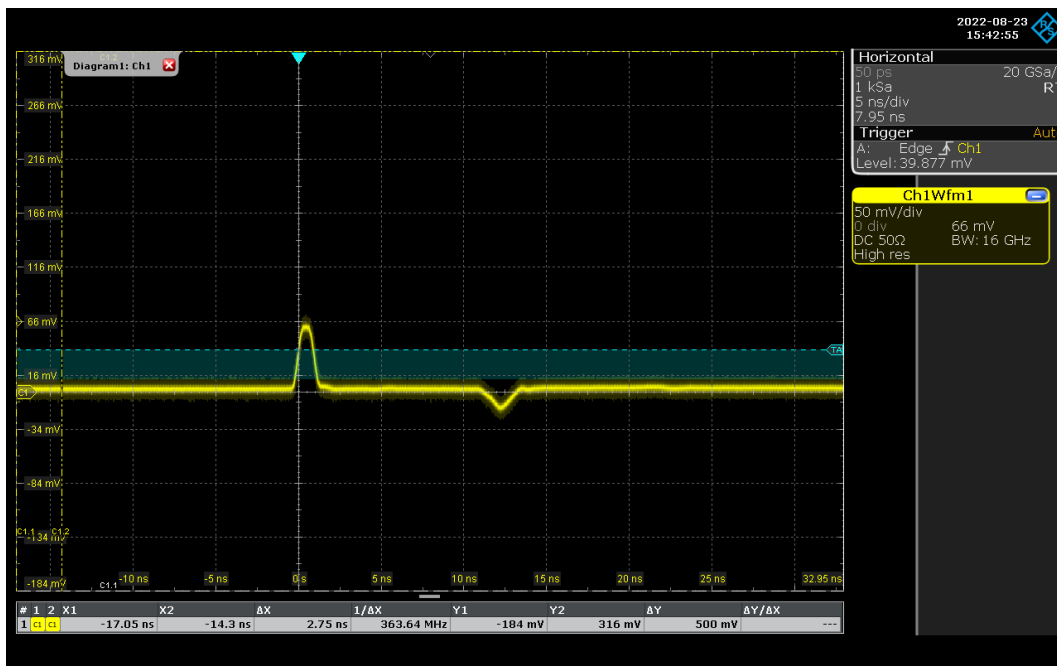


Figure 5.34: Response of the system to a pulse disturbance under its voltage threshold. The pulse width is 1 ns and its amplitude is 64 mV. The DC bias voltage applied was 0.96 V.

In the all-or-none property this corresponds to the none, the response that is seen at 12 ns corresponds to the reflection of the disturbance pulse that appears because of the short-circuit that is present in the experimental setup.

5. RESULTS AND DISCUSSION

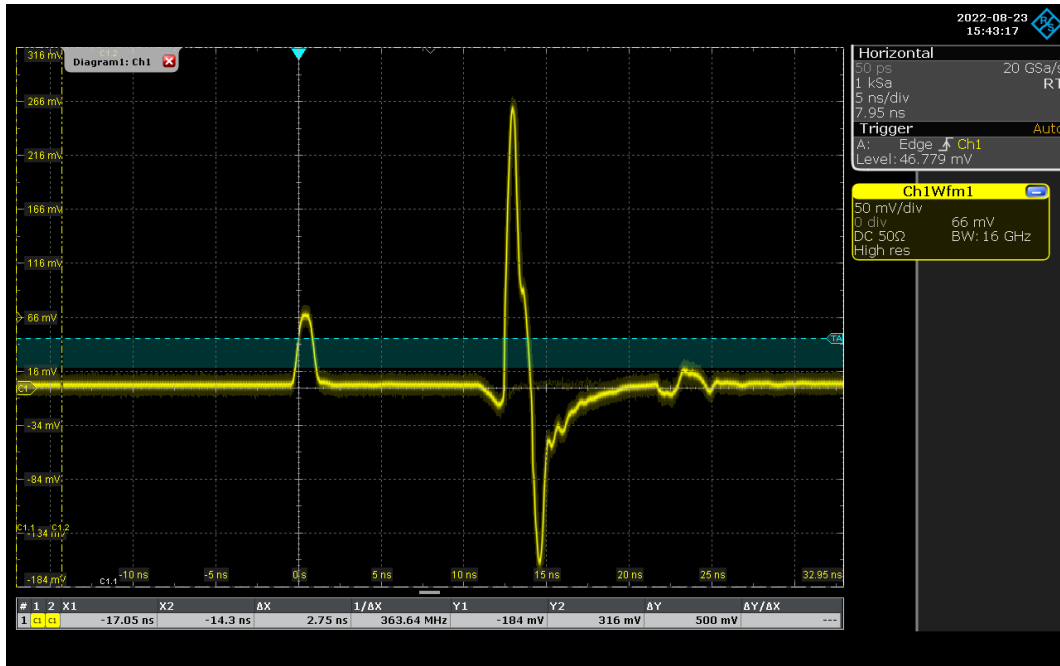


Figure 5.35: Response of the system to a pulse disturbance over its voltage threshold. The pulse width is 1 ns and its amplitude is 65 mV. The DC bias voltage applied was 0.96 mV.

This corresponds to the all response property, this implies that this RTD, when biased at 0.96 V and disturbed with a pulse with 1 ns of width has a 65 mV voltage threshold. In tables 5.10, 5.12, 5.11, and 5.13, the results of the voltage threshold are presented for the forward bias peaks/valleys and for the reverse bias peaks/valleys respectively.

RTD radius (μm)	V_{Peak} (V)	Bias Voltage (V)	Voltage Threshold (mV)
2.5	0.9	0.89	34
3.5	0.93	0.93	110
4	0.96	0.93	50
4.5	0.99	0.96	65
5	1.02	1.01	73
5.5	1.05	1.05	54

Table 5.10: Voltage threshold of the RTDs. V_{Peak} represents the peak voltage defined in 5.1 and the bias voltage the actual voltage that was applied to the devices.

RTD radius (μm)	V_{Peak} (V)	Bias Voltage (V)	Voltage Threshold (mV)
2.5	-0.95	-0.95	-75
3.5	-1.02	-0.97	-46
4	-1.03	-1.03	-102
4.5	-1.05	-1.02	-70
5	-1.09	-1.07	-59
5.5	-1.12	-1.09	-75

Table 5.11: Voltage threshold of the RTDs. V_{Peak} represents the peak voltage defined in 5.2 and the bias voltage the actual voltage that was applied to the devices.

RTD radius (μm)	V_{Valley} (V)	Bias Voltage (V)	Voltage Threshold (mV)
2.5	1.38	1.32	-306
3.5	1.36	1.31	-301
4	1.36	1.33	-225
4.5	1.36	1.35	-213
5	1.36	1.34	-175
5.5	1.38	1.37	-170

Table 5.12: Voltage threshold of the RTDs. V_{Valley} represents the peak voltage defined in 5.3 and the bias voltage the actual voltage that was applied to the devices.

RTD radius (μm)	V_{Valley} (V)	Bias Voltage (V)	Voltage Threshold (mV)
2.5	-1.51	-1.41	277
3.5	-1.50	-1.42	286
4	-1.49	-1.47	250
4.5	-1.49	-1.46	206
5	-1.49	-1.48	200
5.5	-1.49	-1.49	170

Table 5.13: Voltage threshold of the RTDs. V_{Valley} represents the peak voltage defined in 5.4 and the bias voltage the actual voltage that was applied to the devices.

The first problem that was encountered for the peaks was the fact that the bias points that were defined using the experimental data were not the ideal ones, that is, the voltages in the first PDC region that present the highest currents are too close to the NDC region. Due to stability issues the RTDs would enter into their NDC regions and would not exit, causing the RTD to produce oscillations. To solve for this issue the bias voltages were adjusted slightly until the oscilloscope presented a signal similar to the one presented in figure 5.35.

This adjustment comes due to the fact that the bias voltages are too close to the NDC region of the I-V characteristic, causing the RTDs to enter oscillation. This can be understood with the analysis that was performed when describing the VCO in section 5.2. For example, looking at the 2.5 μm RTD in figure 5.22 one can see that the device starts oscillating at around 0.94 V, this indicates that it would be reasonable setting a bias voltage in the range of 0.9 – 0.93 V, but when inspecting the same RTD with the same forward bias on the descend (figure 5.23) one can see that the RTD keeps oscillating until around 0.91 V, this can also be seen on all of the other RTDs in these two plots: all the curves shift to the left on the descend. In the reverse bias the same behaviour is perceived but this time all of the curves have been shifted to the right

It is because of this phenomenon that the bias voltages need to be slightly tuned, most of them to lower values: the RTD when disturbed with a pulse "covers" the ascend I-V characteristic in the rising edge, but goes through the descend in the downwards edge. These adjustments that were performed were only to infer stability, more adjustments could have been made, for example the 3.5 μm RTD could have been biased with a higher voltage that would lead to a lower voltage threshold, but this analysis was left for the following section where the object of study were the bias voltages instead of the pulse amplitudes.

Analysing the voltage threshold of tables 5.10 and 5.11 no clear pattern is found. This indicates that for the peaks this analysis is not enough to characterize the stability of the different radius RTDs and to compare the forward and reverse bias thresholds.

5. RESULTS AND DISCUSSION

In the valley the adjustments were in the opposite direction, that is, if the RTDs were biased in the valley voltages defined in 5.3 and 5.4 the voltage threshold would escalate. To put it simply, the amplitude of the disturbance pulse would be bigger than the resulting spike from the RTD. So, the procedure consisted in reducing the voltage putting the bias point of the RTD closer to its NDC and then adjusting the amplitude of the pulse until a spike was seen on the oscilloscope.

It is noted is that for the valley a bigger pulse needs to be applied in order for the spike to be measured, this happens because the valleys present less stability than the peaks because they are less "sharp". It is due to this fact that the spikes generated by using the valley are smaller than the spikes generated by using the peak, because the RTD is biased further away from its valley voltage (closer to the NDC) the fast transitions correspond to a smaller "jump" in voltage of the orbits.

Unlike the peak voltage thresholds, the stability of the different sized RTDs in the valley seem to exhibit a pattern. Bigger RTDs can be biased closer to their NDC region and thus have lower voltage threshold points, as seen in tables 5.12 and 5.13.

With this analysis only some conclusions can be inferred, the first one is that the bias points that are calculated with the I-V characteristics are not the proper ones to apply to the RTDs, the peak bias points need to be moved farther away from the NDC, i.e to a lower voltage while the valley points need to be moved closer to the NDC. They all need to be biased with a lower voltage but for different reasons as explained above. The second conclusion is that the peak bias points present better stability than the valley bias points, this happens due to the fact that the transition from the first PDC to the NDC region is much sharper than the NDC to the second PDC region.

5.3.3 Influence of the Bias Points on the Generated Spike

There are four operation points for each of the RTDs, in the forward bias a peak and a valley and in the reverse bias another peak and valley. Depending on the operation point used the generated spike presents different characteristics, more specifically on the direction of the generated spike. This analysis was performed for the 4.5 μm , RTD and it is put forward bellow.

In figure 5.36 a spike generated by biasing the 4.5 μm device in its forward peak voltage point and disturbing it with a 75 mV pulse is presented, one can see that for the positive bias peak the system, when disturbed, produces a spike that first goes up, that is, it increases in amplitude to then decrease, this can be understood by looking at the orbits that were put forward in figure 3.13. Because the RTD enters its NDC region near its peak voltage there is a sudden voltage increase that corresponds to the first fast transition, then the first slow stage begins and the voltage drops slowly, then, when the orbit reaches the minimum of the second PDC the second fast transition begins and the voltage drops suddenly, finally the second slow stage begins and the RTD returns to its peak voltage.

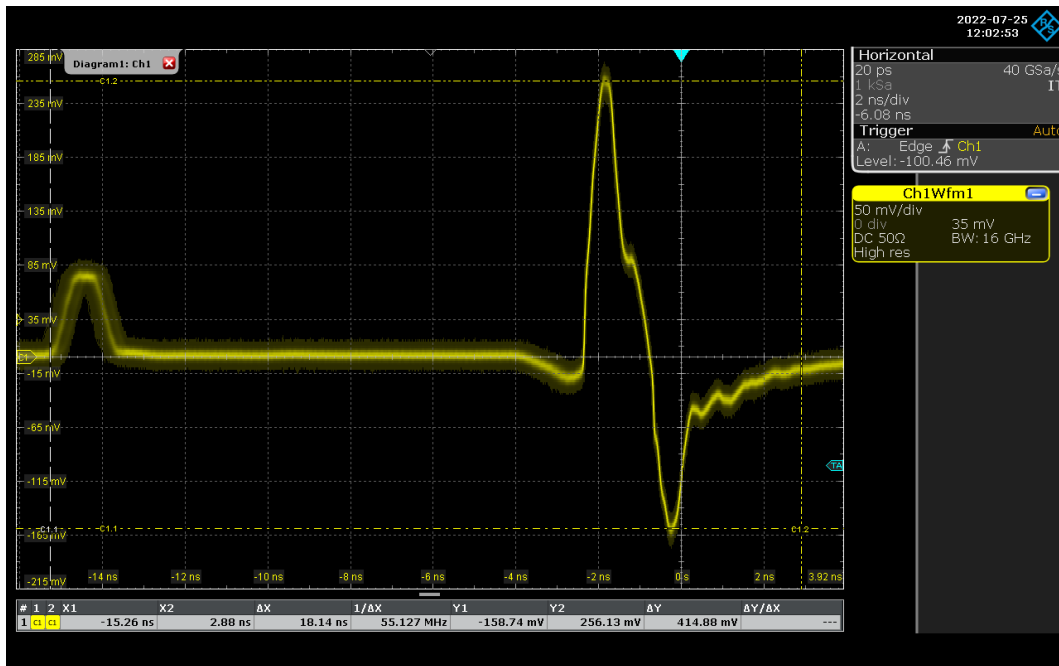


Figure 5.36: Oscilloscope trace for the generated spike of the 4.5 μm RTD, when disturbed in its forward peak voltage. The bias voltage was of 0.96 V and the pulse amplitude was of 75 mV and 1 ns width.

The same analysis can be performed for the valley voltage. The forward bias valley points, when disturbed with a negative pulse does the path that starts with the fast transition from the ending of the NDC to the first PDC, so, the generated spike goes downwards as it can be seen in figure 5.37, the rest of the analysis is the same as for the peak: when the first fast transition ends the voltage starts rising again slowly until it reaches the maximum of the first PDC, then the fast transition occurs and the voltage rises abruptly, the final slow stage is then covered and the RTD reaches its valley voltage again.

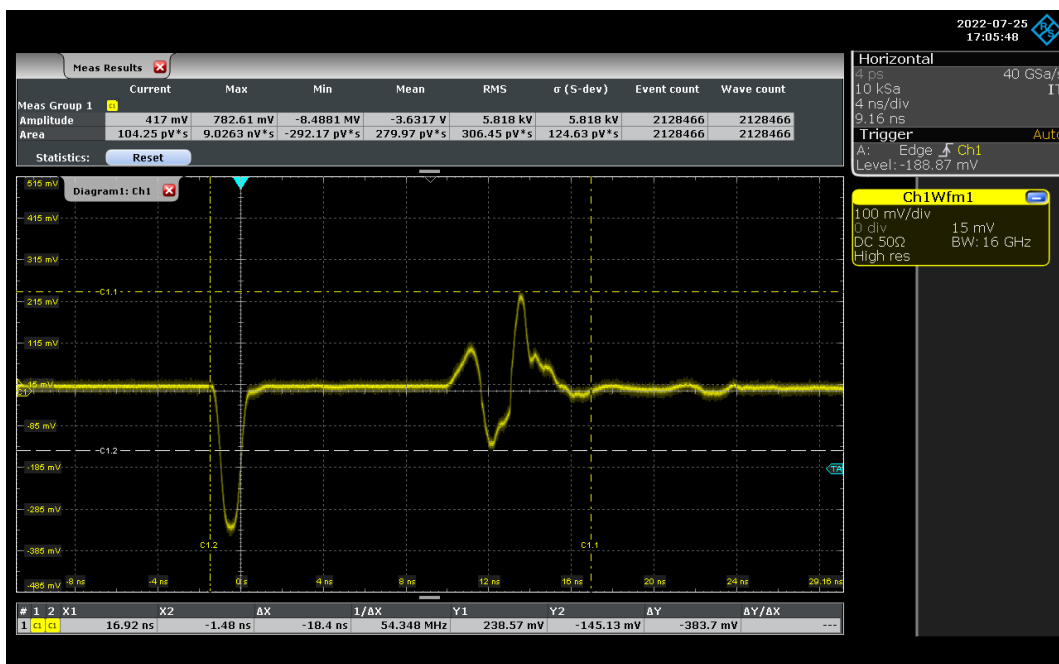


Figure 5.37: Oscilloscope trace for the generated spike of the 4.5 μm RTD, when disturbed in its forward valley voltage. The bias voltage was of 1.43 V and the pulse amplitude was of -350 mV and 1 ns width.

5. RESULTS AND DISCUSSION

For the reverse bias peaks the behaviour is similar, the difference is that the current voltage characteristic is the anti-symmetrical counterpart of the forward bias, so the generated spike is the symmetrical counterpart of the one produced by the forward operation points, as it can be seen in figures D.1 and D.2 presented in the appendices.

This behaviour of the direction of the paths of operation seen for the $4.5 \mu\text{m}$ RTD is also present in all of the other RTDs operation points.

5.3.4 Bias Voltage Analysis

The voltage thresholds that were presented in tables 5.10, 5.11, 5.12 and 5.13 correspond to the experimentally determined peak and valley bias voltages, because of the dynamics of the RTDs these bias voltages are not all at the same "distance" from their respective NDC regions and the bias voltage needs to be adjusted.

A better analysis was then performed by setting reliable voltage thresholds for all of the RTDs: for the peaks 50 mV and 100 mV in absolute value because voltage thresholds lower than 50 mV would cause the devices to enter their NDC and oscillate; for the valleys 300 mV for the positive valley and -350 mV. A deeper analysis on the valleys could be performed but due to the fact that they present stability issues it was decided that these values would suffice for an understanding of their susceptibility to the disturbance. This analysis was also performed for pulses of different widths to have a better understanding of the dependence of the excitability of the RTDs with the duration of the perturbation.

In figures 5.38 and 5.39 the method that was described in figures 4.12 and 4.13 is presented as an example of what was measured in the laboratory for the $4.5 \mu\text{m}$ RTD when disturbed with a pulse of 100 mV and 1 ns of width. Using this same disturbance pulse the bias voltage had to be slightly raised (from 0.9 V to 0.911 V) until a spike, depicted in figure 5.39 was seen.

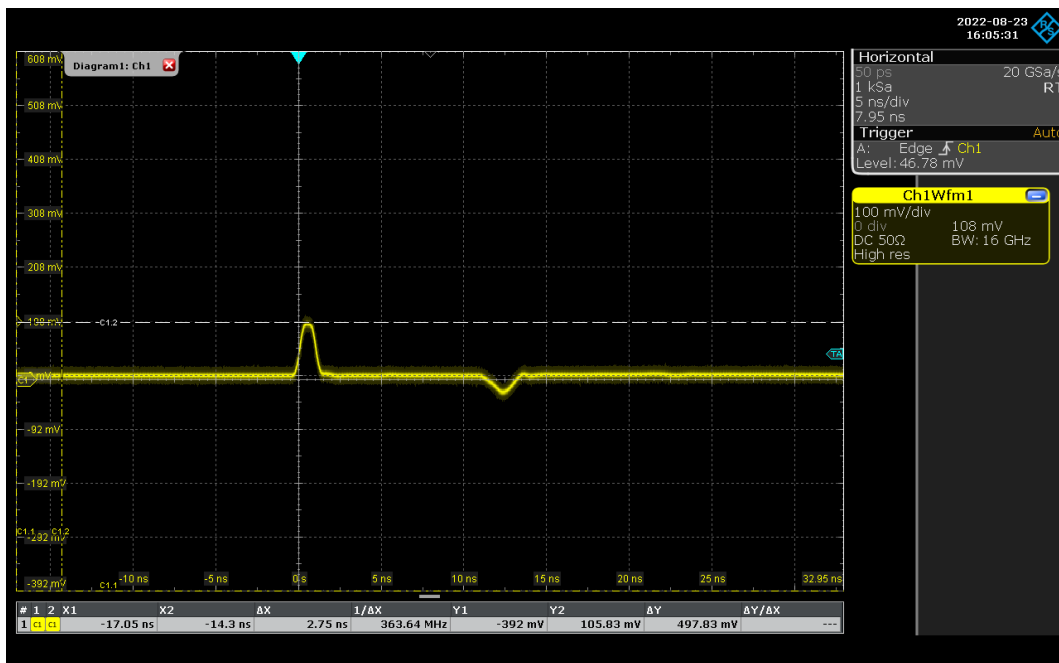


Figure 5.38: Response of the $4.5 \mu\text{m}$ RTD to a 100mV pulse with 1 ns of width. The bias voltage applied was $V_{DC} = 0.9$ V.

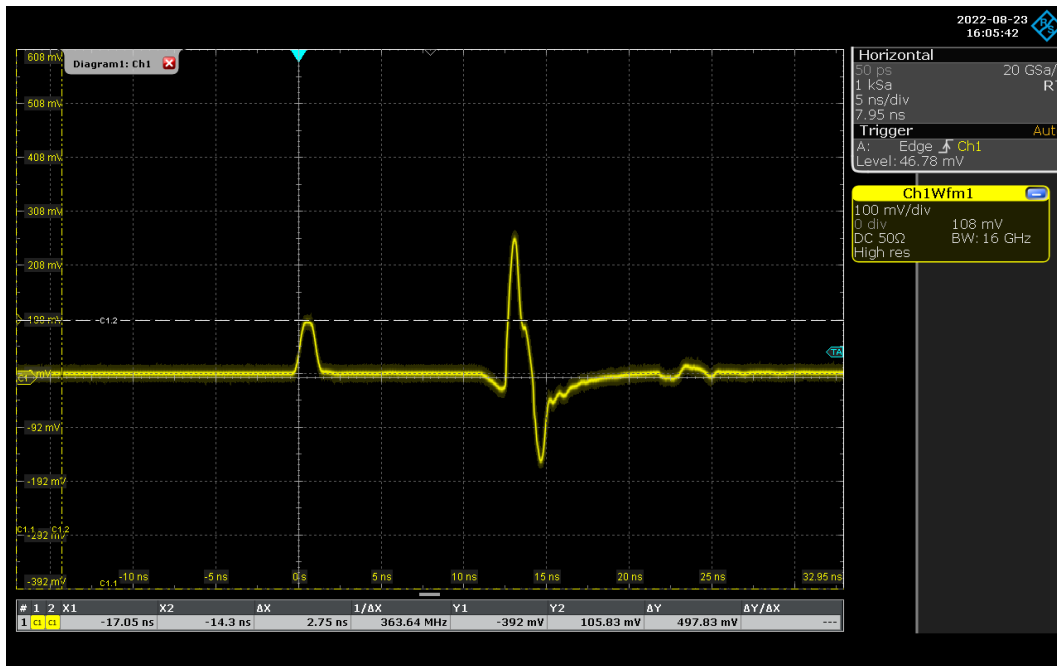


Figure 5.39: Response of the system to the same disturbance (100mV pulse with 1 ns of width) but with a higher bias voltage of $V_{DC} = 0.911$ V.

This indicates that for the forward bias peak region of the $4.5 \mu\text{m}$ RTD, when using a 100 mV disturbance pulse with 1 ns of width the minimum bias voltage that needs to be applied is $V_{DC} = 0.911$ V. As explained in section 4.2.4 one of the goals of this experimental activity was to study the influence of the disturbance pulse width with the spike generation of these RTDs so the temporal width of the spikes were changed: for all of the peaks (DC bias on the peak regions) 0.5, 0.6, 0.7, 0.8, 0.9, 1, 2, 3, 4 and 5 ns pulse widths and for the all of the valleys (DC bias on the valley regions) pulses of 0.5, 1, 2.5 and 5 ns.

In figures 5.40 and 5.41 the results for the minimum bias voltages are presented when the forward and reverse bias RTDs are perturbed with a ± 50 mV disturbance in their peak bias voltages with different temporal widths.

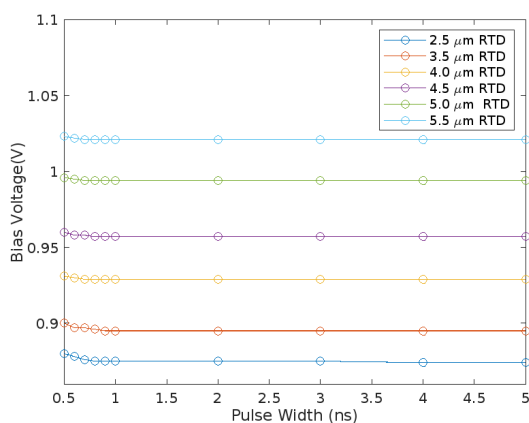


Figure 5.40: Minimum Bias voltage to be applied to the forward bias (peak) RTD as a function of the pulse width. The pulse amplitude used was of 50 mV.

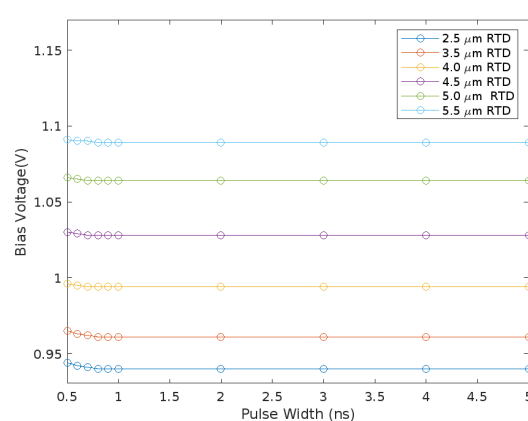


Figure 5.41: Minimum Bias voltage to be applied to the reverse bias (peak) RTD as a function of the pulse width. The pulse amplitude used was of -50 mV. Only the absolute value of the bias voltage was considered for the plots for an easier analysis.

5. RESULTS AND DISCUSSION

In both the forward and reverse bias it is noted that bigger RTDs need higher bias voltages to produce a spike, this happens due to the fact that their NDC regions occur at higher voltages, as it was seen in the VCO characterization. It is also seen that the reverse bias RTDs need higher bias voltages when compared with the forward bias. This can also be understood by inspecting figures 5.22 and 5.25. In figure 5.22 the RTDs start oscillating at lower (absolute) bias voltages than in figure 5.25. This means that for the same perturbation, reverse bias RTDs need higher bias voltages to produce a spike.

In figures 5.42 and 5.43 the results for the minimum bias voltages are presented when the forward and reverse bias RTDs biased at their peaks are perturbed with a ± 100 mV disturbance in their peak bias voltages with different temporal widths.

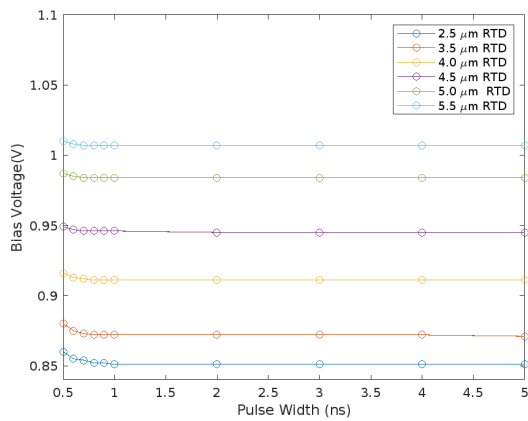


Figure 5.42: Minimum Bias voltage to be applied to the forward bias (peak) RTD as a function of the pulse width. The pulse amplitude used was of 100 mV.

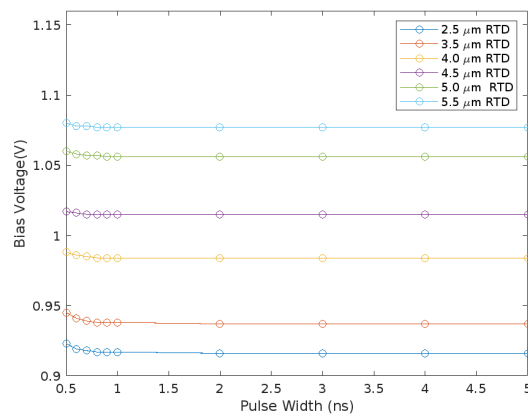


Figure 5.43: Minimum Bias voltage to be applied to the reverse bias (peak) RTD as a function of the pulse width. The pulse amplitude used was of -100 mV. Only the absolute value of the bias voltage was considered for the plots for an easier analysis.

The analysis that was made for the 50 mV perturbation is also valid for the 100 mV, larger area RTDs need higher bias voltages; forward bias RTDs present lower minimum bias voltages, that is, using the same disturbance pulse one needs to apply a higher bias voltage if using reverse bias. The main conclusion from this analysis is that a difference of 50 mV in the perturbation pulse does not correspond to a 50mV difference in the minimum bias voltage. If one uses 50 mV of voltage threshold the minimum bias voltage only needs to be around 25 mV higher than the one used for 100 mV pulse amplitude.

In figures 5.44 and 5.45 the results for the minimum bias voltages are presented when the forward and reverse bias RTDs are perturbed with a ± 350 mV disturbance in their valley bias voltages with different temporal widths respectively.

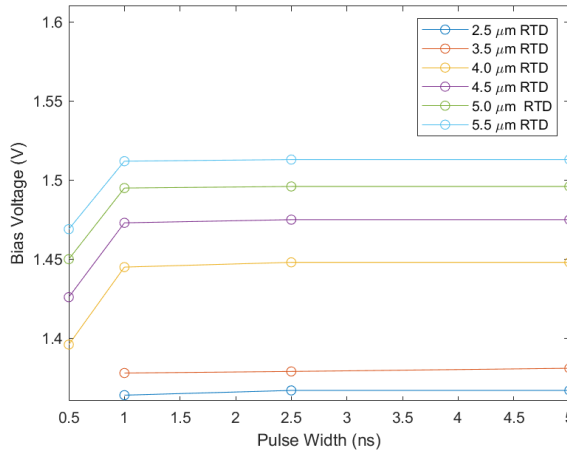


Figure 5.44: Minimum Bias voltage to be applied to the forward bias (valley) RTD as a function of the pulse width. The pulse amplitude used was of -350 mV.

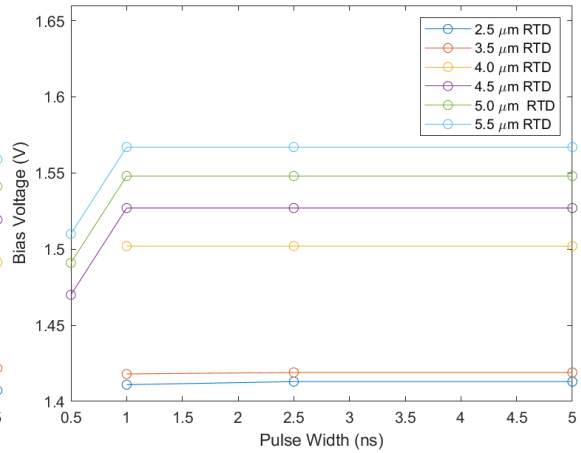


Figure 5.45: Minimum Bias voltage to be applied to the forward bias (valley) RTD as a function of the pulse width. The pulse amplitude used was of 350 mV. Only the absolute value of the bias voltage was considered for the plots for an easier analysis.

Again, for the valleys, the same behaviour is observed, the minimum bias voltage seems to increase with the device. The reverse bias RTD also needs higher bias voltages in order to present a spike. The lack of points on the 0.5 ns pulse widths comes due to the fact that, for this width, the pulse amplitude had to be increased to the point that the RTD would enter its NDC and oscillate. This is another indication on the lack of stability of the valleys as bias points to produce spikes. The main goal for this bias voltage analysis on the valleys was to infer the influence of the pulse widths on the minimum bias voltage applied to the RTDs.

The main conclusion that is made from this bias voltage analysis is that: for pulses wider than 1 ns the minimum bias voltage remains constant, this indicates that the voltage threshold of the system only depends on the pulse width if the pulse width is smaller than 1 ns, this seems to be true not only the peaks but also for the valleys.

Despite having stability issues the valleys were still characterized because even though they need bigger pulses than the peaks, the operation point presents a much lower electric power. Despite having to work at higher bias voltages they are working on much less current (about 10 times lower). Meaning that they consume much less electric power.

5.3.5 Refractory Time

The results for the refractory times of all the RTDs bias in their peaks are presented in tables 5.14 and 5.15 for the forward and reverse bias voltages respectively. In table 5.16 the refractory times for the valleys is also presented.

5. RESULTS AND DISCUSSION

RTD Radius (μm)	Pulse Amplitude: 50 mV		Pulse Amplitude: 100 mV	
	Refractory Time (ns)	Bias Voltage (V)	Refractory Time (ns)	Bias Voltage (V)
2.5	2	0.892	2	0.89
3.5	2	0.906	2	0.89
4	9	0.938	8	0.93
4.5	9	0.984	9	0.96
5	13	0.996	13	0.986
5.5	16	1.028	13	1.02

Table 5.14: Refractory Times and respective peak bias voltages off all the RTDs, for pulses with 50 mV and 100 mV of amplitude. The pulse width was of 1 ns.

RTD Radius (μm)	Pulse Amplitude: -50 mV		Pulse Amplitude: -100 mV	
	Refractory Time (ns)	Bias Voltage (V)	Refractory Time (ns)	Bias Voltage (V)
2.5	3	-0.946	2	-0.94
3.5	3	-0.969	3	-0.95
4	13	-0.999	7	-1
4.5	13	-1.031	13	-1.02
5	15	-1.058	13	-1.058
5.5	21	-1.086	13	-1.09

Table 5.15: Refractory Times and respective peak bias voltages off all the RTDs, for pulses with -50 mV and -100 mV of amplitude. The pulse width was of 1 ns.

RTD Radius (μm)	Pulse Amplitude: -350 mV		Pulse Amplitude: 350 mV	
	Refractory Time (ns)	Bias Voltage (V)	Refractory Time (ns)	Bias Voltage (V)
2.5	7	1.33	7	-1.398
3.5	7	1.3	7	-1.41
4	5	1.37	8	-1.49
4.5	6	1.425	6	-1.52
5	6	1.44	8	-1.54
5.5	7	1.45	8	-1.551

Table 5.16: Refractory Times and respective valley bias voltages off all the RTDs, for pulses with ± 350 mV of amplitude. The pulse width was of 1 ns.

The trend that is seen is that, for the peak bias voltages, the refractory time decreases with the size of the device, that is: smaller RTDs have shorter refractory times. In figure 5.46 the oscilloscope trace for the $2.5 \mu\text{m}$ RTD is presented for the positive peak being disturbed with a 50 mV amplitude pulse.

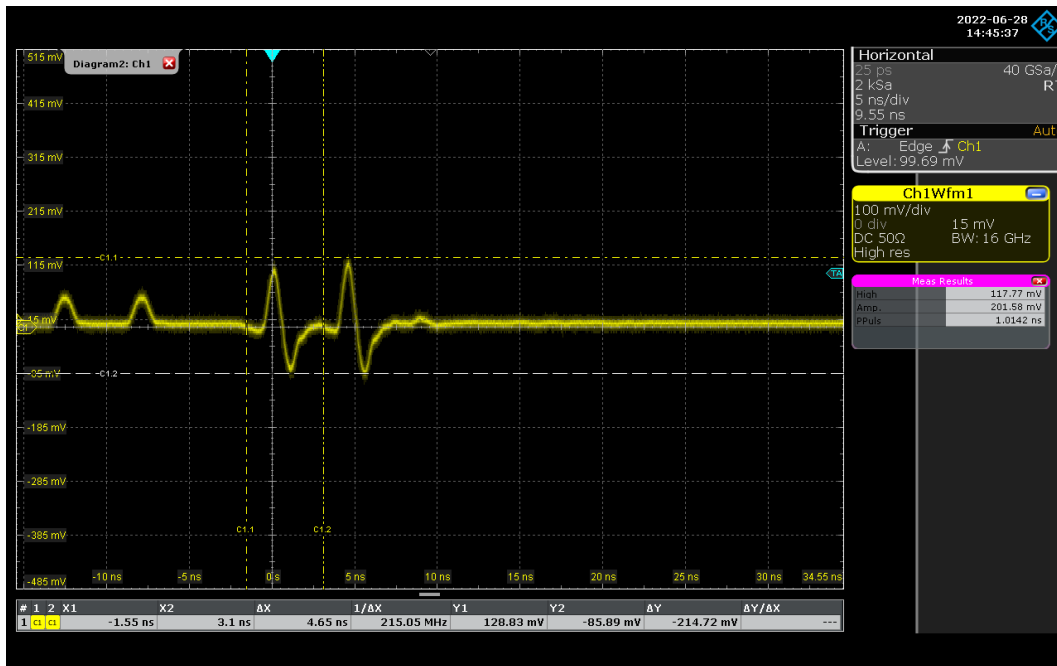


Figure 5.46: Oscilloscope trace for the 2.5 μm RTD responding to two pulses (50 mV) separated by 2 ns. The RTD was biased in its positive peak voltage.

In this case the RTDs can respond to pulses with shorter separation than the reaction time of the system. In figure 5.47 the oscilloscope trace for the 2.5 μm RTD is presented for the positive peak being disturbed with a 50 mV amplitude pulse.

In figure 5.47 the oscilloscope trace is presented for the 5.5 μm RTD.

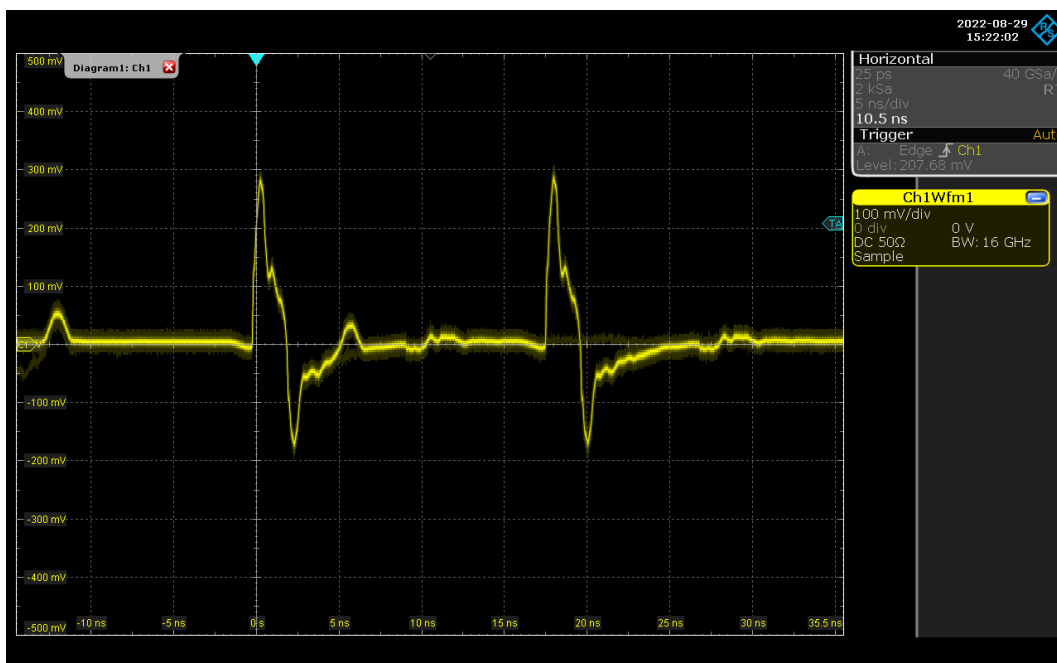


Figure 5.47: Oscilloscope trace for the 5.5 μm RTD responding to two pulses (50 mV) separated by 13 ns. The RTD was biased in its positive peak voltage.

The behaviour for this RTD is that the refractory time is bigger than the reaction time of the system, so only the first disturbance pulse is clearly observed in the oscilloscope because the other is "inserted"

5. RESULTS AND DISCUSSION

in the first generated spike. If one tried to decrease the temporal separation between the disturbance pulses the second spike would not be observed.

It appears that the refractory time cannot be close to the reaction time of the system, it either is bigger making the system respond like figure 5.47 or smaller (figure 5.46).

Another conclusion that is made by comparing the refractory times of pulses with 50 mV and 100 mV is that increasing the pulse amplitude seems to influence the refractory time for some of the RTDs. For example, the $4\mu\text{m}$ RTD when biased in its reverse bias peak voltage presents a 7 ns refractory time for a 100 mV disturbance while for a 50 mV it presents 13 ns.

It is because of this behaviour that the RTDs biased in their valley voltages can all present refractory times shorter than the ones for the peaks. In figure 5.48 the oscilloscope trace is presented for the $4.5\mu\text{m}$ RTD biased in its positive valley voltage.

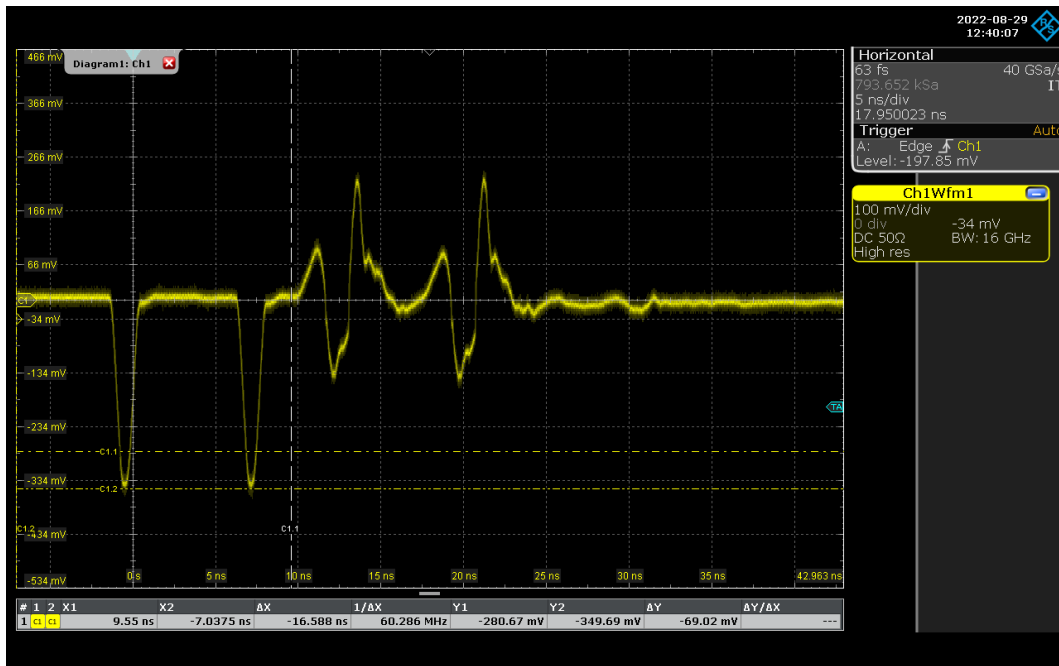


Figure 5.48: Oscilloscope trace for the $4.5\mu\text{m}$ RTD responding to two pulses (-350 mV) separated by 6 ns. The RTD was biased in its positive peak voltage.

The fact that smaller RTDs present smaller refractory times is an indication that the scaling down of the device can increase its response rate which is a promising result.

5.4 Simulation using MatLab's Simulink/Simscape

In this section the results obtained from the MatLab Simulink/Simscape simulation are put forward and discussed. The layout for this section is the following: first the current voltage characteristics that were obtained using the curve fitting algorithm developed and used in simulation are put forward. After this the other input parameters of simulation for each of the RTDs are presented and briefed through.

The waveforms that are generated when the RTDs are biased at their NDC regions are also presented and characterized followed by a discussion on whether they can be considered spikes by estimating their $\sqrt{\frac{C}{L}}$ values. Remember that in section 3.5 it was shown that when the ratio of the capacitance over the inductance is low: $\sqrt{\frac{C}{L}} \ll 1$, the oscillations that are created present a "slow-fast" dynamics (see figure 3.12).

5.4 Simulation using MatLab's Simulink/Simscape

Finally, the property of excitability of the 2.5 μm RTD was demonstrated using a disturbance pulse in both its peak and valley regions.

Remember that the circuit that we are simulating is the basic AC signal equivalent circuit for a RTD, see figure 3.8.

The function $F(V)$ is given by:

$$F(V) = M \left(A \ln \left[\frac{1 + e^{(B-C+n_1V)e/(k_B T)}}{1 + e^{(B-C-n_1V)e/(k_B T)}} \right] \left[\frac{\pi}{2} + \tan^{-1} \left(\frac{C - n_1V}{D} \right) \right] + H \left(e^{n_2Ve/(k_B T)} - 1 \right) \right) \quad (5.1)$$

The current voltage characteristics used as well as the other simulation parameters are presented in the sections below.

5.4.1 I-V Characteristics

It is noted that only the forward bias ascending direction I-V characteristics were used in this study, this means that the self-oscillation that are generated when the RTDs are biased at their NDC regions are only for the forward bias RTD ascending I-V curves. The I-V curves and respective derivatives for the 2.5 and 3.5 μm RTDs are presented in figures 5.49 and 5.50 respectively.

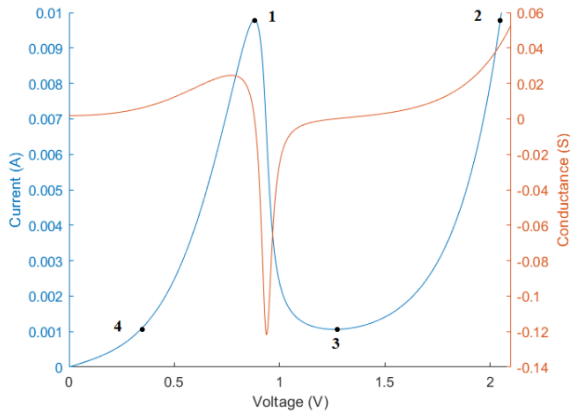


Figure 5.49: I-V curve of the 2.5 μm RTD in the ascend with load line at $V_{DC} = 0.95$ V.

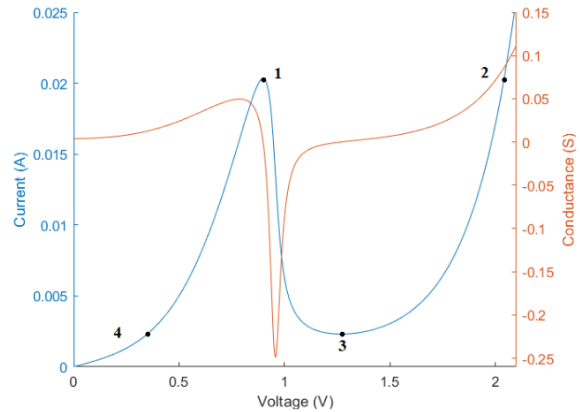


Figure 5.50: I-V curve of the 3.5 μm RTD in the ascend with load line at $V_{DC} = 0.97$ V.

Using equation 3.12 one can estimate the value of the critical resistance. The critical resistance calculated for these two devices was $R_C = 8.3 \Omega$ for the 2.5 μm RTD and $R_C = 4.04 \Omega$ for the 3.5 μm RTD. These values will be compared with the actual critical resistance that was determined using the simulator.

The points that represent the orbits of the oscillations, numbered from 1 to 4 in figures 5.49 and 5.50 are presented in table 5.17.

RTD	2.5 μm				3.5 μm			
Points	1	2	3	4	1	2	3	4
Voltage (V)	0.875	2.04	1.265	0.38	0.89	2.039	1.287	0.35
Current (mA)	9.77	9.77	1.3	1.3	28.1	28.1	2.9	2.9

Table 5.17: Orbit points (voltage and current) for the 2.5 and 3.5 μm RTDs.

5. RESULTS AND DISCUSSION

These values will be used to help characterize the oscillations that are seen on the RTDs when they are biased in their NDC regions.

The I-V curves and respective derivatives for the 4 and 4.5 μm RTDs are presented in figures 5.51 and 5.52 respectively.

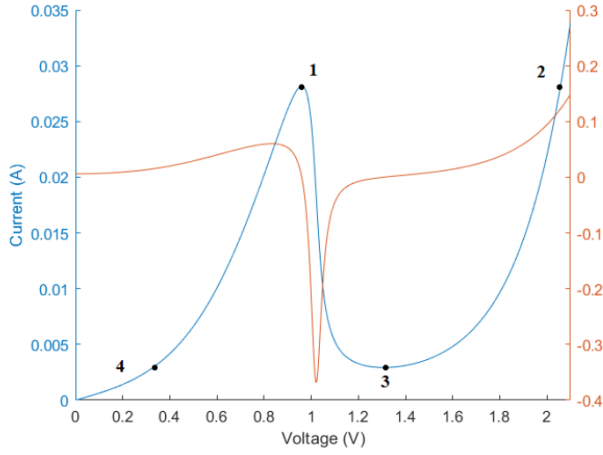


Figure 5.51: I-V curve of the 4 μm RTD in the ascend with load line at $V_{DC} = 1.03$ and $R = 1 \Omega$.

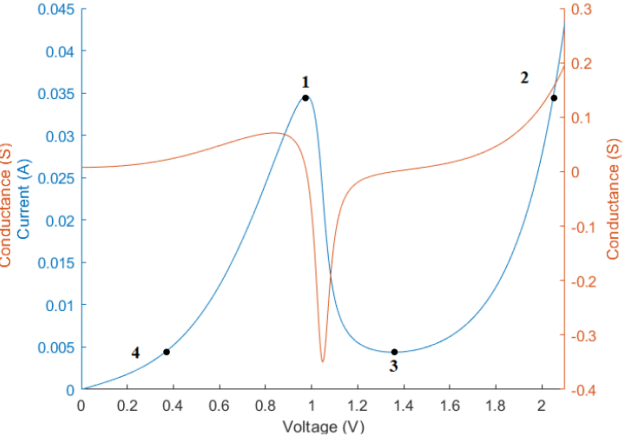


Figure 5.52: I-V curve of the 4.5 μm RTD in the ascend with load line at $V_{DC} = 1.07$ and $R = 1 \Omega$.

Again, using equation 3.12 one can estimate the value of the critical resistance, for these two devices: $R_C = 2.73 \Omega$ for the 4 μm RTD and $R_C = 2.62 \Omega$ for the 4.5 μm RTD.

The points that represent the orbits of the oscillations, numbered from 1 to 4 in figures 5.51 and 5.52 are presented in table 5.18.

RTD	4 μm				4.5 μm			
	1	2	3	4	1	2	3	4
Voltage (V)	0.957	2.057	1.3	0.34	0.97	2.052	1.35	0.37
Current (mA)	28.1	28.1	2.9	2.9	34.7	34.7	4.4	4.4

Table 5.18: Orbit points (voltage and current) for the 4 and 4.5 μm RTDs.

The I-V curves and respective derivatives for the 5 and 5.5 μm RTDs are presented in figures 5.53 and 5.54 respectively.

5.4 Simulation using MatLab's Simulink/Simscape

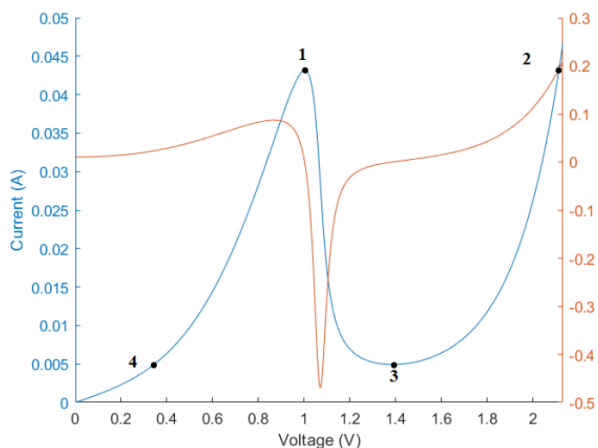


Figure 5.53: I-V curve of the $5 \mu\text{m}$ RTD in the ascend with load line at $V_{DC} = 1.1$ and $R = 1 \Omega$.

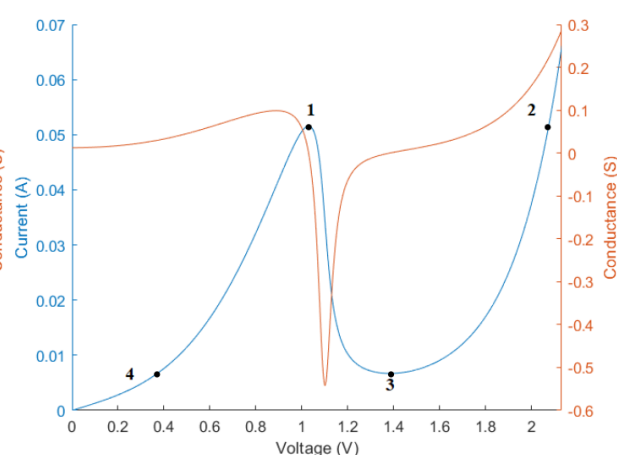


Figure 5.54: I-V curve of the $5.5 \mu\text{m}$ RTD in the ascend with load line at $V_{DC} = 1.13$ and $R = 1 \Omega$.

Again, using equation 3.12 the critical resistance for these two devices: $R_C = 2.14 \Omega$ for the $5 \mu\text{m}$ RTD and $R_C = 1.85 \Omega$ for the $5.5 \mu\text{m}$ RTD. This implies that the resistance chosen for the simulator needs to be smaller than 1.85Ω .

The points that represent the orbits of the oscillations, numbered from 1 to 4 in figures 5.53 and 5.54 are presented in table 5.19.

RTD	$5 \mu\text{m}$				$5.5 \mu\text{m}$			
Points	1	2	3	4	1	2	3	4
Voltage (V)	1.01	2.1	1.38	0.36	1.03	2.08	1.38	0.37
Current (mA)	43	43	4.9	4.9	51.9	51.9	6.7	6.7

Table 5.19: Orbit points (voltage and current) for the 5 and $5.5 \mu\text{m}$ RTDs.

5.4.2 Simulation Parameters

The simulation parameters that were the same for all of the RTD circuits are presented in table 5.20.

Parameters	Values
R	1Ω
L	50 nH
e	$1.602 \times 10^{-19} \text{ C}$
k_B	$1.381 \times 10^{-23} \text{ J K}^{-1}$
T	297 K

Table 5.20: Simulation parameters that remained constant for all of the RTDs.

The circuit presented in figure 3.8 accounts for the basic AC signal equivalent circuit for a RTD, however the setups used in the experimental activities contain a resonant cavity that allow the production of an RF signal. In this simulation this was accounted for in the choice of the inductance parameter L . The value of inductance that was chosen was $L = 50 \text{ nH}$.

The simulation input parameters for the $2.5 \mu\text{m}$, $3.5 \mu\text{m}$ and $4 \mu\text{m}$ RTDs are presented in table 5.21.

5. RESULTS AND DISCUSSION

Parameters	2.5 μm	3.5 μm	4 μm
C_{RTD}	39.3 fF	79.97 fF	100.53 fF
A	$1.187 \times 10^4 \text{ A cm}^{-2}$	$1.309 \times 10^4 \text{ A cm}^{-2}$	$1.171 \times 10^4 \text{ A cm}^{-2}$
B	0.04337 V	0.04106 V	0.04873 V
C	0.1418	0.1382	0.1369 V
D	0.004704	0.004566 V	0.003928 V
H	4.263 A cm^{-2}	5.209 A cm^{-2}	4.548 A cm^{-2}
n1	0.1515	0.1448	0.1343
n2	0.1168	0.1154	0.1171
M	$1.96 \times 10^{-7} \text{ cm}^2$	$3.84 \times 10^{-7} \text{ cm}^2$	$5.03 \times 10^{-7} \text{ cm}^2$

Table 5.21: Simulation parameters for the 2.5 μm , 3.5 μm and 4 μm RTD.

The simulation input parameters concerning the 4.5 μm , 5 μm and 5.5 μm RTDs are presented in table 5.22.

Parameters	4.5 μm	5 μm	5.5 μm
C_{RTD}	127.25 fF	157.08 fF	190.07 fF
A	$1.159 \times 10^4 \text{ A cm}^{-2}$	$1.323 \times 10^4 \text{ A cm}^{-2}$	$1.238 \times 10^4 \text{ A cm}^{-2}$
B	0.04978 V	0.04193 V	0.04457 V
C	0.1362 V	0.1281 V	0.1278 V
D	0.004978 V	0.004248 V	0.004241 V
H	2.949 A cm^{-2}	2.297 A cm^{-2}	4.081 A cm^{-2}
n1	0.1303	0.12	0.1164
n2	0.1224	0.122	0.117
M	$6.36 \times 10^{-7} \text{ cm}^2$	$7.85 \times 10^{-7} \text{ cm}^2$	$9.5 \times 10^{-7} \text{ cm}^2$

Table 5.22: Simulation parameters for the 4.5 μm , 5 μm and 5.5 μm RTD.

The choice of C_{RTD} came from the fact that the RTD capacitance can be estimated as $\sim 2 \text{ fF}\mu\text{m}^{-2}$ (Ironsides et al. (2009)). With the values of inductance and capacitance that were defined above the value of the ratio of the capacitance of the the inductance is much less than one for every RTD with the 5.5 μm RTD presenting the highest value of 0.0019. So, all of these devices will be in the fast-slow regime and a spike (large amplitude signal) is observed.

5.4.3 Waveforms

The waveforms presented are only for the I-V curves in the ascending direction as it was mentioned above. The waveform for the voltage across the the capacitor, is presented in figure 5.55 for the 2.5 μm RTD. The voltage bias is $V_{DC} = 0.95 \text{ V}$. The waveform of the current in the resistor and the inductor is presented in figure 5.56, the very sharp current pulses that is go through the capacitor are also presented.

5.4 Simulation using MatLab's Simulink/Simscape

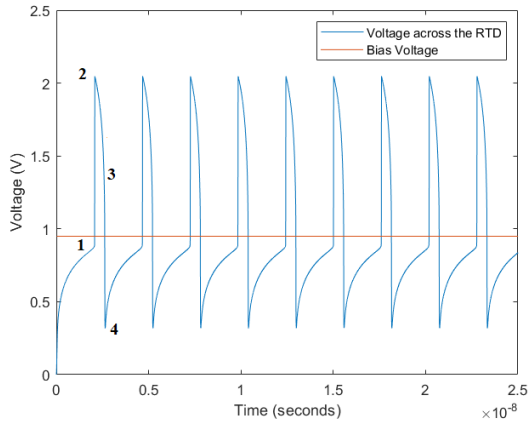


Figure 5.55: Voltage across the $2.5 \mu\text{m}$ radius RTD for a bias voltage of $V_{DC} = 0.95 \text{ V}$.

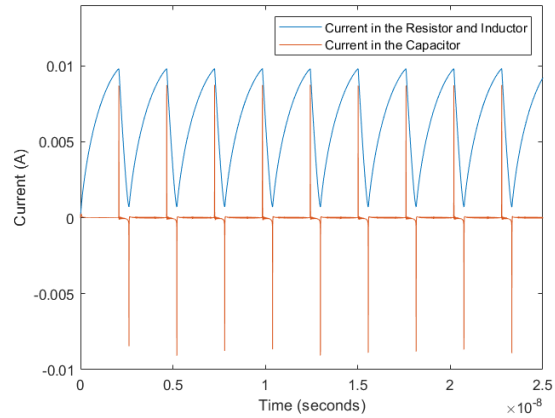


Figure 5.56: Current going through the resistor and the inductor for a bias voltage of $V_{DC} = 0.95 \text{ V}$. The current across the capacitor is also presented. This figure is concerning the $2.5 \mu\text{m}$ radius RTD.

The points marked in bold in figure 5.56 represent the points that were presented in figure 5.49 and the values that are put forward in table 5.17 for the $2.5 \mu\text{m}$ RTD.

This RTD has a $\sqrt{\left(\frac{C}{L}\right)} = 0.0009$. This implies that the oscillations that the RTD is producing are spikes because $\sqrt{\left(\frac{C}{L}\right)} \ll 1$ thus implying the fast-slow transitions that are happening in the voltage across the RTD.

The critical resistance that this device presents is $R_C = 7.2 \Omega$, that is, if the value of resistance is increased any further the RTD will cease to oscillate. This value goes in accordance with the 8.3Ω that were estimated using the current voltage characteristic.

The waveform FFT (waveform spectrum) analyser result for the oscillations of voltage across the capacitor is presented in figure 5.57. This spectrum analyser was added to the simulation because it is a way of measuring the frequency of oscillation of the produced spikes.

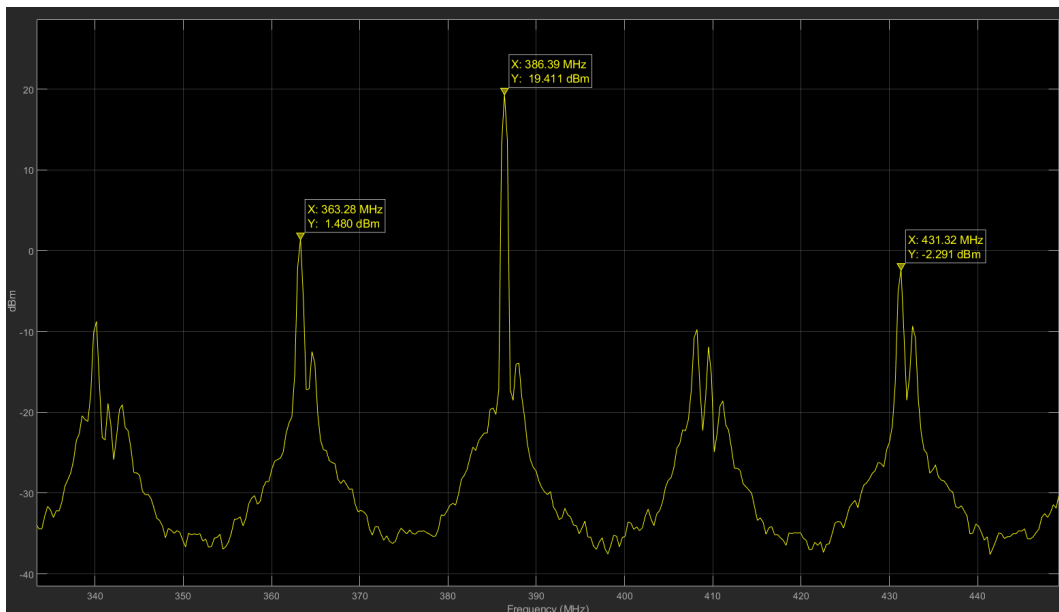


Figure 5.57: Spectrum analyser result for the simulation presented above of the $2.5 \mu\text{m}$ RTD.

This result implies that the oscillations that are being presented in figure 5.55 have a frequency of

5. RESULTS AND DISCUSSION

oscillation of 386.39 MHz. This value is slightly higher than the experimentally measured frequency for the $2.5 \mu\text{m}$ RTD of around 300 MHz.

The simulation waveform for the voltage across the capacitor presented in figure 5.58 for the $3.5 \mu\text{m}$ RTD. The voltage bias is $V_{DC} = 0.97 \text{ V}$. The waveform of the current in the resistor and the inductor is presented in figure 5.59, the current that is going through the capacitor is also presented.

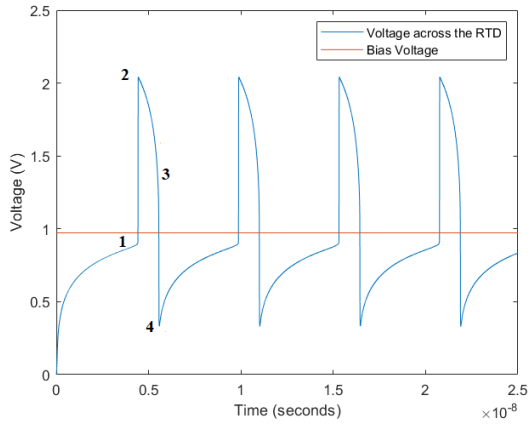


Figure 5.58: Voltage across the $3.5 \mu\text{m}$ radius RTD for a bias voltage of $V_{DC} = 0.97 \text{ V}$.

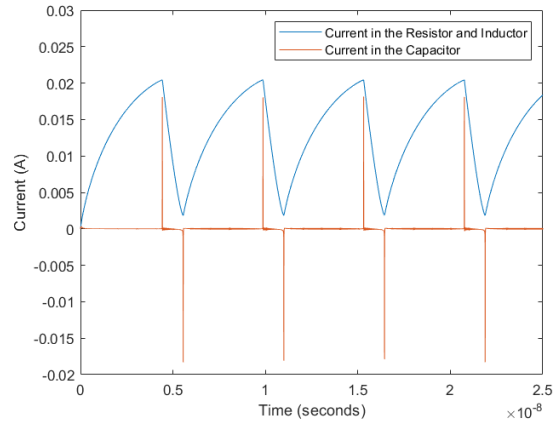


Figure 5.59: Current going through the resistor and the inductor for a bias voltage of $V_{DC} = 0.97 \text{ V}$. the current going through the capacitor is also presented. This figure is concerning the $3.5 \mu\text{m}$ radius

The points marked in bold in figure 5.59 represent the points that were presented in figure 5.50 and the values that are put forward in table 5.17 for the $3.5 \mu\text{m}$ RTD.

This RTD has a $\sqrt{\left(\frac{C}{L}\right)} = 0.0013$. This implies that the oscillations that the RTD is producing are spikes because $\sqrt{\left(\frac{C}{L}\right)} \ll 1$ thus implying the fast-slow transitions that are happening in the voltage across the RTD.

The critical resistance that this device presents is $R_C = 3.9 \Omega$, that is, if the value of resistance is increased any further the RTD will cease to oscillate. This value goes in accordance with the 4.04Ω that were estimated using the current voltage characteristic.

The waveform FFT (waveform spectrum) analyser result for the oscillations of voltage across the capacitor is presented in figure 5.60.

5.4 Simulation using MatLab's Simulink/Simscape

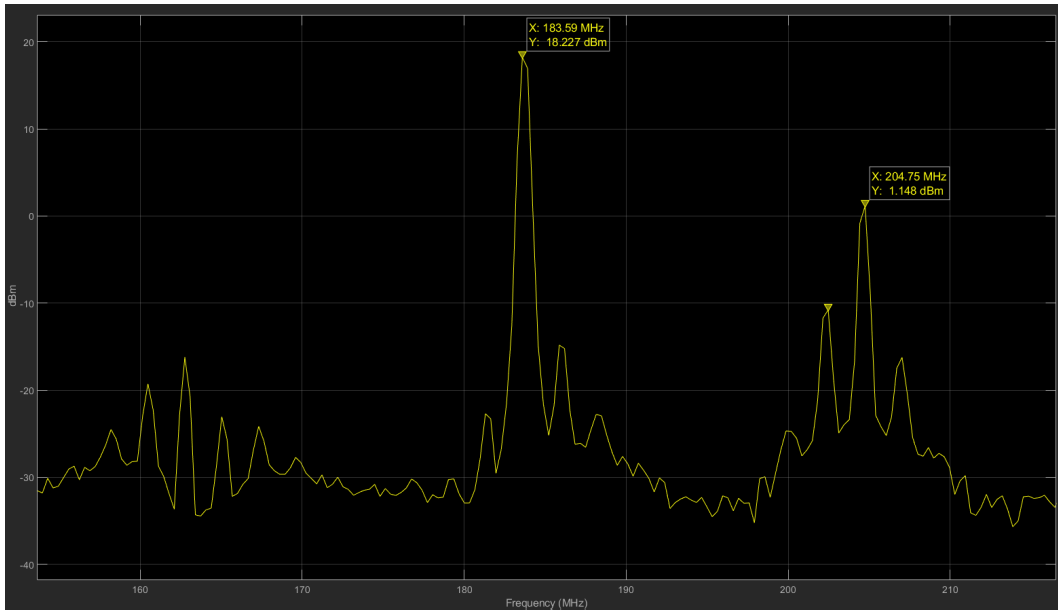


Figure 5.60: Spectrum analyser result for the simulation presented above of the $3.5 \mu\text{m}$ RTD.

This result implies that the oscillations that are being presented in figure 5.58 have a frequency of oscillation of 183.59 MHz. Despite the fact that this value is lower than the experimentally measured frequency for the $3.5 \mu\text{m}$ RTD of around 250 MHz it still goes in accordance with it.

The simulation waveform for the voltage across capacitor is presented in figure 5.61 for the $4 \mu\text{m}$ RTD. The voltage bias is $V_{DC} = 1.03 \text{ V}$. The waveform of the current in the resistor and the inductor is presented in figure 5.62, the current that is going through the capacitor is also presented.

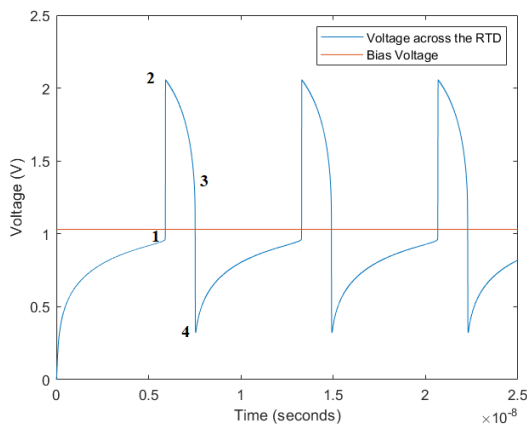


Figure 5.61: Voltage across the $4 \mu\text{m}$ radius RTD for a bias voltage of $V_{DC} = 1.03 \text{ V}$.

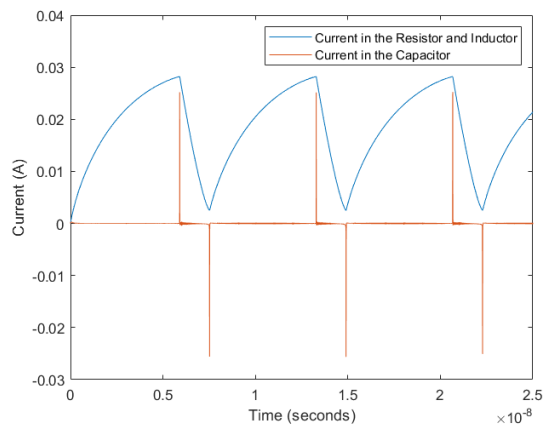


Figure 5.62: Current going through the resistor and the inductor for a bias voltage of $V_{DC} = 1.03 \text{ V}$. The current going through the capacitor is also presented. This figure is concerning the $4 \mu\text{m}$ radius

The points marked in bold in figure 5.62 represent the points that were presented in figure 5.51 and the values that are put forward in table 5.18 for the $4 \mu\text{m}$ RTD.

This RTD has a $\sqrt{\left(\frac{C}{L}\right)} = 0.0014$. This implies that the oscillations that the RTD is producing are spikes because $\sqrt{\left(\frac{C}{L}\right)} \ll 1$ thus implying the fast-slow transitions that are happening in the voltage across the RTD.

The critical resistance that this device presents is $R_C = 2.7 \Omega$, that is, if the value of resistance is

5. RESULTS AND DISCUSSION

increased any further the RTD will cease to oscillate. This value goes in accordance with the 2.73Ω that were estimated using the current voltage characteristic.

The waveform FFT (waveform spectrum) analyser result for the oscillations of voltage across the capacitor is presented in figure 5.63.

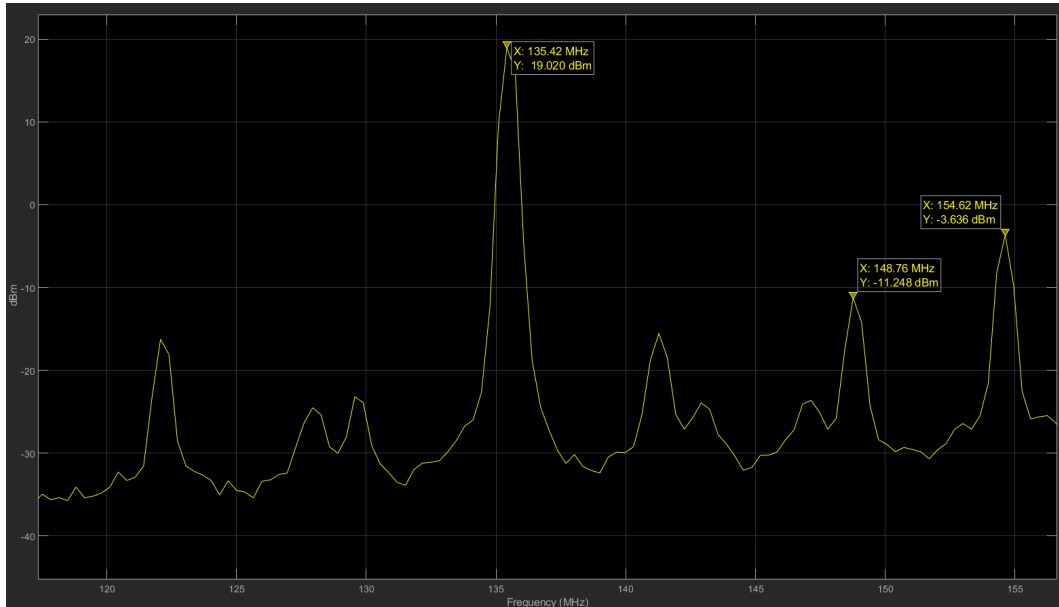


Figure 5.63: Spectrum analyser result for the simulation presented above of the $4 \mu\text{m}$ RTD.

This result implies that the oscillations that are being presented in figure 5.61 have a frequency of oscillation of 135.42 MHz. Despite the fact that this value is lower than the experimentally measured frequency for the $4 \mu\text{m}$ RTD of around 200 MHz which can still be considered a valid result.

The simulation waveform for the voltage across the capacitor is presented in figure 5.64 for the $4 \mu\text{m}$ RTD. The voltage bias is $V_{DC} = 1.07 \text{ V}$. The current going through the resistor and the inductor is presented in figure 5.65.

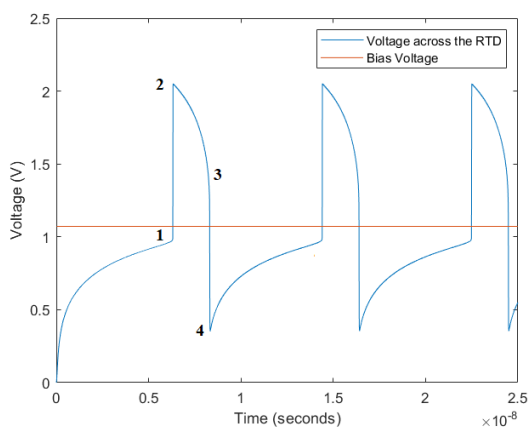


Figure 5.64: Voltage across the $4.5 \mu\text{m}$ radius RTD for a bias voltage of $V_{DC} = 1.07 \text{ V}$.

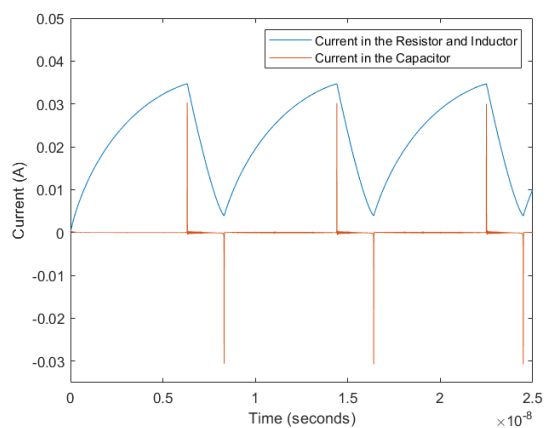


Figure 5.65: Current going through the resistor and the inductor for a bias voltage of $V_{DC} = 1.07 \text{ V}$. the current going through the capacitor is also presented. This figure is concerning the $4.5 \mu\text{m}$ radius

The points marked in bold in figure 5.65 represent the points that were presented in figure 5.52 and the values that are put forward in table 5.18 for the $4.5 \mu\text{m}$ RTD.

5.4 Simulation using MatLab's Simulink/Simscape

This RTD has a $\sqrt{\left(\frac{C}{L}\right)} = 0.0016$. This implies that the oscillations that the RTD is producing are spikes because $\sqrt{\left(\frac{C}{L}\right)} \ll 1$ thus implying the fast-slow transitions that are happening in the voltage across the RTD.

The critical resistance that this device presents is $R_C = 2.6 \Omega$, that is, if the value of resistance is increased any further the RTD will cease to oscillate. This value goes in accordance with the 2.62Ω that were estimated using the current voltage characteristic.

The waveform FFT (waveform spectrum) analyser result for the oscillations of voltage across the capacitor is presented in figure 5.66.

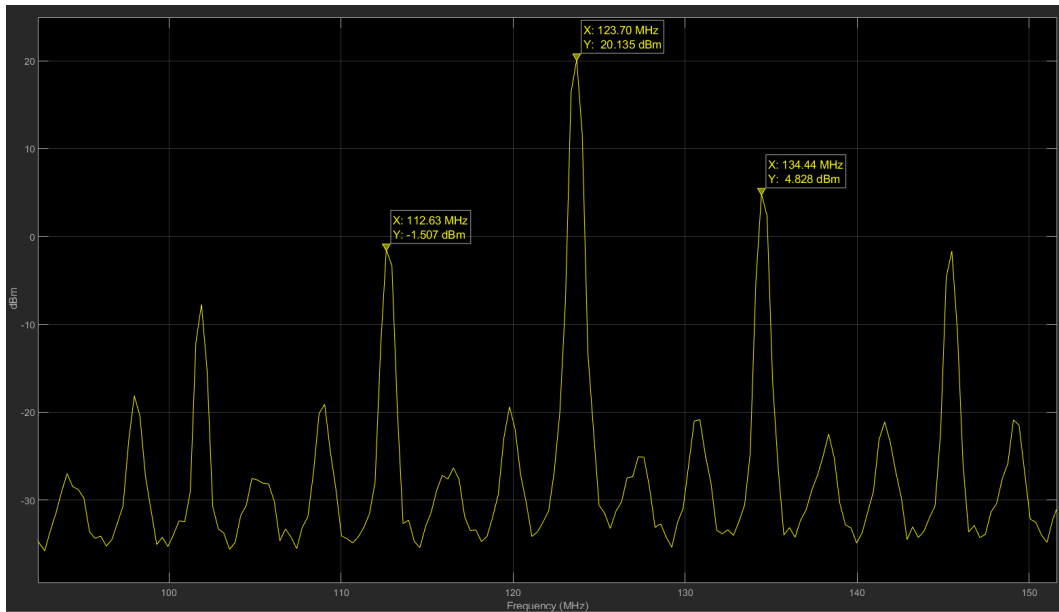


Figure 5.66: Spectrum analyser result for the simulation presented above of the $4.5 \mu\text{m}$ RTD.

This result implies that the oscillations that are being presented in figure 5.64 have a frequency of oscillation of 123.7 MHz. Despite the fact that this value is lower than the experimentally measured frequency for the $4.5 \mu\text{m}$ RTD of around 150 MHz it is still a valid result.

The simulation waveform for the voltage across the capacitor is presented in figure 5.67 for the $5 \mu\text{m}$ RTD. The voltage bias is $V_{DC} = 1.1 \text{ V}$. The waveform of the current in the resistor and the inductor is presented in figure 5.68, the current that is going through the capacitor is also presented.

5. RESULTS AND DISCUSSION

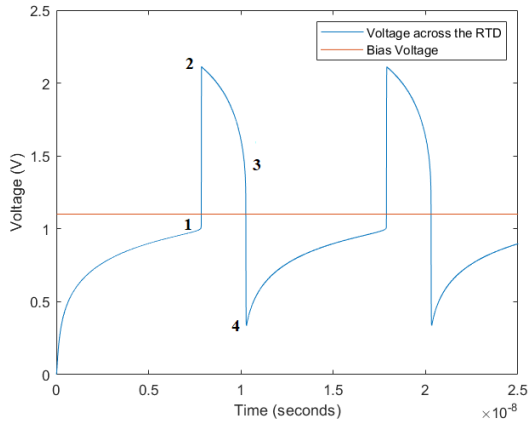


Figure 5.67: Voltage across the $5 \mu\text{m}$ radius RTD for a bias voltage of $V_{DC} = 1.1 \text{ V}$.

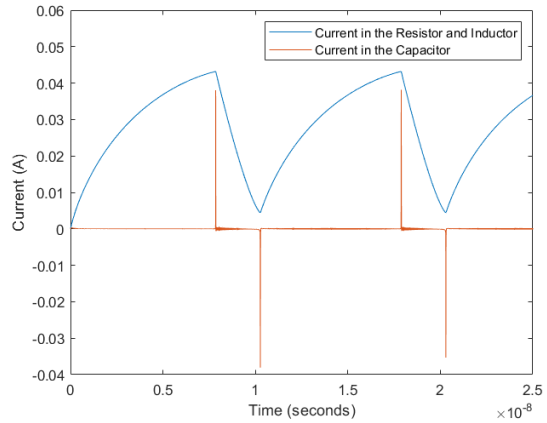


Figure 5.68: Current going through the resistor and the inductor for a bias voltage of $V_{DC} = 1.1 \text{ V}$. the current going through the capacitor is also presented. This figure is concerning the $5 \mu\text{m}$ radius

The numbered points marked in bold in figure 5.68 represent the points that were presented in figure 5.53 and the values that are put forward in table 5.19 for the $5 \mu\text{m}$ RTD

This RTD has a $\sqrt{\left(\frac{C}{L}\right)} = 0.0018$. This implies that the oscillations that the RTD is producing are spikes because $\sqrt{\left(\frac{C}{L}\right)} \ll 1$ thus implying the fast-slow transitions that are happening in the voltage across the RTD.

The critical resistance that this device presents is $R_C = 2 \Omega$, that is, if the value of resistance is increased any further the RTD will cease to oscillate. This value goes in accordance with the 2.14Ω that were estimated using the current voltage characteristic.

The waveform FFT (waveform spectrum) analyser result for the oscillations of voltage across the capacitor is presented in figure 5.69.

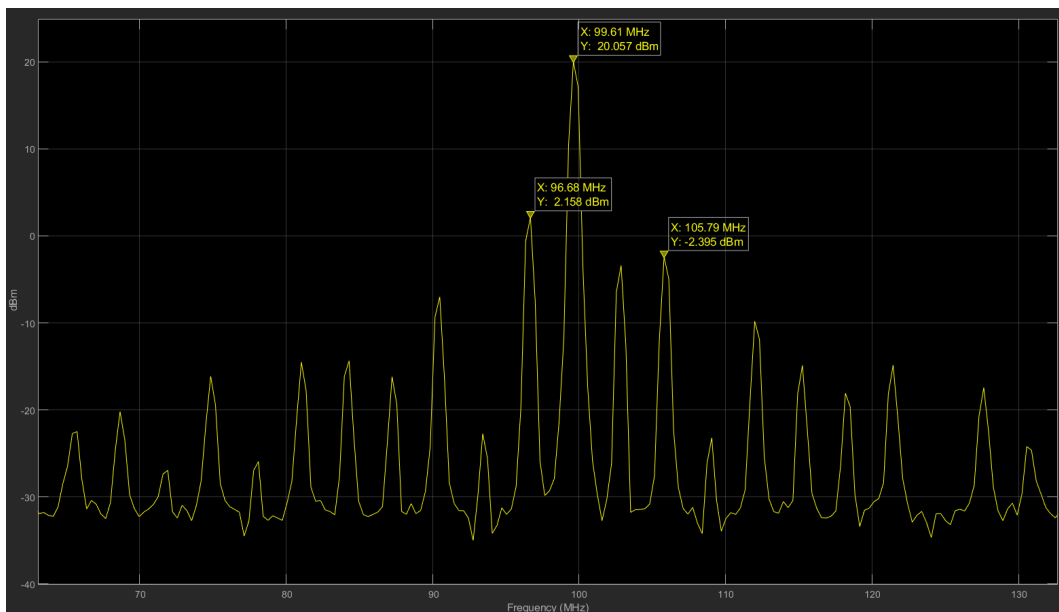


Figure 5.69: Spectrum analyser result for the simulation presented above of the $5 \mu\text{m}$ RTD.

This result implies that the oscillations that are being presented in figure 5.67 have a frequency of oscillation of 99.61 MHz. Despite the fact that this value is lower than the experimentally measured

5.4 Simulation using MatLab's Simulink/Simscape

frequency for the $5 \mu\text{m}$ RTD of around 130 MHz it is still a valid result.

The simulation waveform for the voltage across the capacitor is presented in figure 5.70 for the $5.5 \mu\text{m}$ RTD. The voltage bias is $V_{DC} = 1.13 \text{ V}$. The waveform of the current in the resistor and the inductor is presented in figure 5.71, the current that is going through the capacitor is also presented.

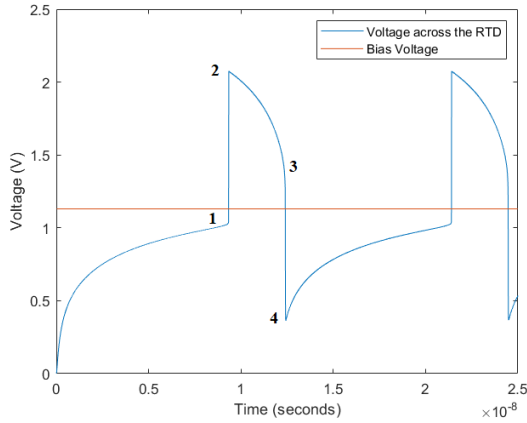


Figure 5.70: Voltage across the $5.5 \mu\text{m}$ RTD for a bias voltage of $V_{DC} = 1.13 \text{ V}$.

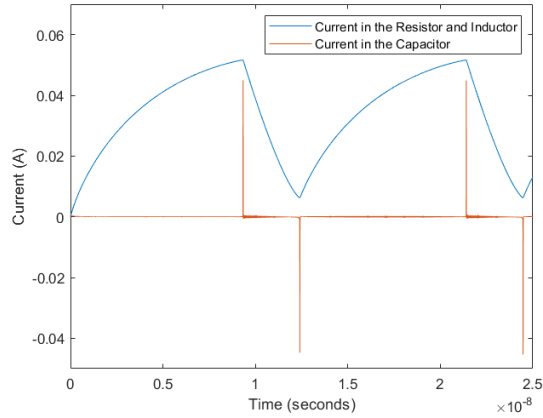


Figure 5.71: Current going through the resistor and the inductor for a bias voltage of $V_{DC} = 1.13 \text{ V}$. the current going through the capacitor is also presented. This figure is concerning the $5.5 \mu\text{m}$ radius

The numbered points marked in bold in figure 5.71 represent the points that were presented in figure 5.53 and the values that are put forward in table 5.19 for the $5.5 \mu\text{m}$ RTD.

This RTD has a $\sqrt{\left(\frac{C}{L}\right)} = 0.0019$. This implies that the oscillations that the RTD is producing are spikes because $\sqrt{\left(\frac{C}{L}\right)} \ll 1$ thus implying the fast-slow transitions that are happening in the voltage across the RTD.

The critical resistance that this device presents is $R_C = 1.4 \Omega$, that is, if the value of resistance is increased any further the RTD will cease to oscillate. This value goes in accordance with the 1.85Ω that were estimated using the current voltage characteristic.

The waveform FFT (waveform spectrum) analyser result for the oscillations of voltage across the capacitor is presented in figure 5.72.

5. RESULTS AND DISCUSSION

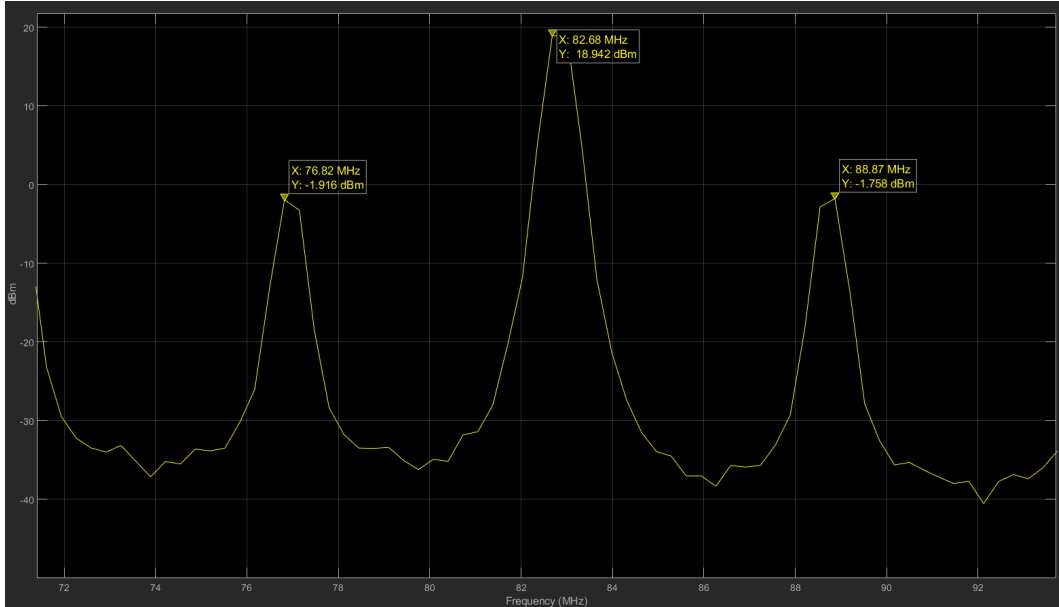


Figure 5.72: Spectrum analyser result for the simulation presented above of the $5.5 \mu\text{m}$ RTD.

This result implies that the oscillations that are being presented in figure 5.70 have a frequency of oscillation of 82.68 MHz. Despite the fact that this value is lower than the experimentally measured frequency for the $5.5 \mu\text{m}$ RTD of around 125 MHz it is still a valid result.

The discrepancy that is seen between the experimental and the simulated frequencies of oscillation is due to the uncertainty of the capacitance of the RTD, the value of 2 fF is an estimation and allows to estimate that the devices oscillate at MHz frequencies.

The very sharp pulses in the current going through the capacitors can be explained in the following way: when looking at the points in the current voltage characteristics in the transition **1** to **2** the voltage across the capacitor increases suddenly, this causes charges to accumulate at the ends of the capacitor. The second sharp pulse of current in the capacitor corresponds to the **3** to **4** transition.

When analysing the waveforms of all of the RTDs it is also noted that the slow-fast dynamics that were put forward in section 3.5 are also seen here: a slow transition that corresponds to the orbit that overlaps the RTD I-V characteristic in the first PDC region, followed by a sudden increase in voltage that corresponds to the first fast transition. Then the second slow transition begins after this and progresses into the second fast transition and a sudden decrease in voltage is observed.

In this analysis the oscillations of the RTDs when biased in their NDC regions were studied, the results indicate that the frequency of oscillation is the main characteristic that changes from RTD to RTD, the $2.5 \mu\text{m}$ RTD is the one that presents the highest frequency of oscillation. The peak to peak amplitude of the spikes when analysing the voltage waveforms seems to remain constant but when looking at the power delivered by the oscillation one can see that the RTDs that correspond to the larger area devices have slightly higher values. Both of the behaviours mentioned here were also seen in the experiments performed using the real RTDs in the laboratory.

5.4.4 Excitability

The analysis that will be explored in this section was only conducted for the $2.5 \mu\text{m}$ RTD, in order to observe the property of excitability in this device the concept that was described in section 3.5 was followed. The first step was deciding the proper bias voltage that should be applied to the device. As

5.4 Simulation using MatLab's Simulink/Simscape

demonstrated before, the RTD can produce a spiking excitable response using both the peaks and the valleys as operation points. The concept is the following: a positive pulse disturbance needs to be applied to the voltage when we are biasing the RTD in its peak; a negative pulse disturbance needs to be applied to the voltage when we are biasing the RTD in its valley. If this disturbance is lower than the voltage threshold of the system almost no response is seen while if the disturbance is greater a spike (large amplitude signal) is observed. This corresponds to the all-or-none property of neuromorphic devices.

For the $2.5 \mu\text{m}$ RTD the bias voltage chosen was of $V_{DC} = 0.88 \text{ V}$. In figure 5.73 the RTD is being disturbed by a 0.01 V pulse with 1 ns of width.

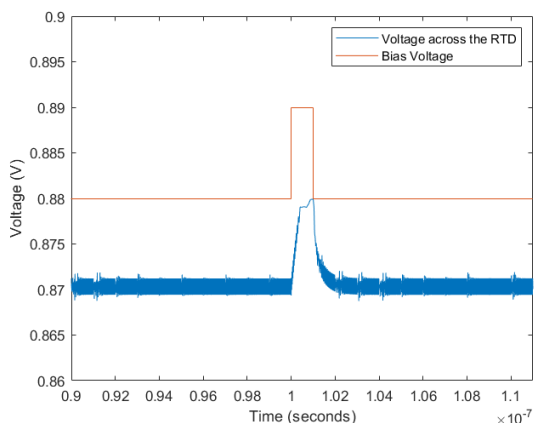


Figure 5.73: Voltage across the RTD for a sub-threshold disturbance in its peak.

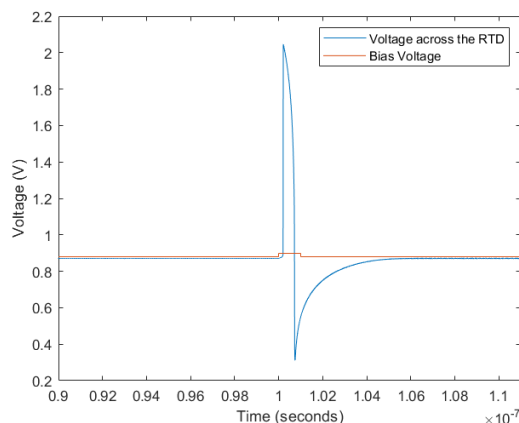


Figure 5.74: Voltage across the RTD for disturbance above its threshold in its peak.

The voltage across the RTD increases momentarily but then decreases to $\sim 0.87 \text{ V}$. This shows that the response of this RTD to a disturbance pulse that is below its threshold produces no significant response, this corresponds to the "none" in the all-or-none law that neuromorphic devices need to present.

In order to observe a spike the amplitude of the pulse needs to be increased, in this case increased from 0.01 V to 0.02 V . In figure 5.74 the pulse amplitude was increased to 0.02 V and the RTD produced a spike. The pulse width remained 1 ns .

This is an indication of the excitability of RTDs to pulse disturbances. The four stages, two fast and two slow, are visible although the first slow stage seems to smoothly transition into the second fast stage. The waveform of the spike is similar to the one presented in figure 5.55. The voltage threshold for the 0.88 V operation point is 20 mV . The same behaviour that was seen experimentally concerning the direction of the spike is seen: when using the peaks as operation points the spike first goes upward and then downward.

The second part of this activity is concerning the excitable property of the RTD when a disturbance in its valley bias voltage is applied. The current voltage characteristic that was considered here was the descending I-V curve of the $2.5 \mu\text{m}$ RTD, presented in figure 5.75 along with its derivative.

5. RESULTS AND DISCUSSION

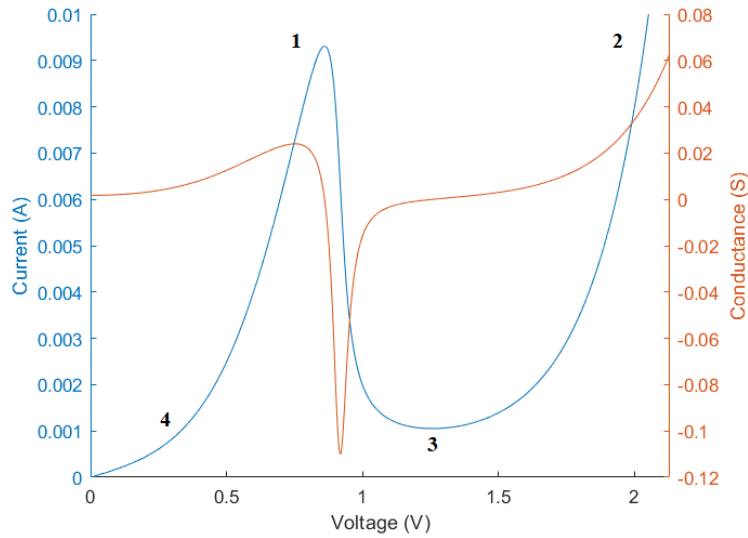


Figure 5.75: I-V curve of the 2.5 μm RTD used to study the excitable response of the device when disturbing it with a negative pulse in its the valley voltage.

The parameters of simulation are presented in table 5.23.

Parameters	2.5 μm RTD
C_{RTD}	39.3 fF
A	$1.161 \times 10^4 \text{ A cm}^{-2}$
B	0.04263 V
C	0.1419 V
D	0.005081 V
H	3.514 A cm^{-2}
n1	0.155
n2	0.1193
M	$1.96 \times 10^{-7} \text{ cm}^2$

Table 5.23: Simulation parameters for the 2.5 μm RTD in the descending direction current voltage characteristic.

In figure 5.76 the excitable response spike of the 2.5 μm RTD is presented for the case when we are disturbing the RTD in its valley voltage. In this case the current voltage characteristic presented in figure 5.75 because this represents the descend. The disturbance pulse width used was the same of before (1 ns).

5.4 Simulation using MatLab's Simulink/Simscape

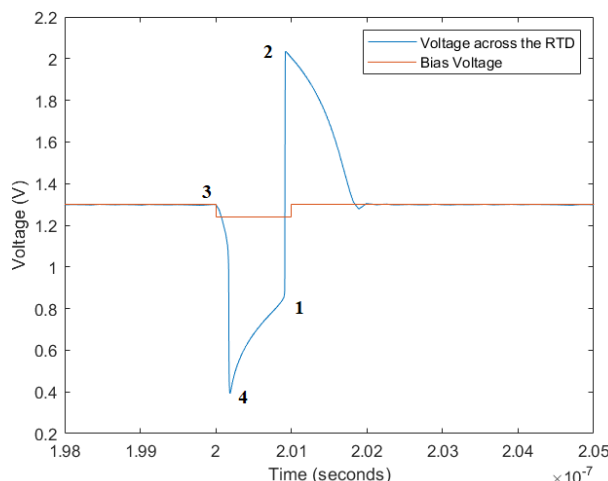


Figure 5.76: Voltage across the RTD for disturbance above its treshold in its valley.

The shape of the spike is different from the one presented in figure 5.74 because the current voltage characteristic is different. In this case the bias voltage was of $V_{DC} = 1.3$ V leading to a voltage threshold of -50 mV. These values of voltage treshold are smaller than the ones that were measured experimentally because a lot more variables influence this value in real life. Concerning the shape of the spike the predicted behaviour is found: using valleys as operation points leads to a spike that first goes downward and then upward. The points that are presented in figure 5.76 represent the values that are marked in figure 5.75 and are presented in table 5.24.

Points	1	2	3	4
Voltage (V)	0.866	2.033	1.263	0.347
Current (mA)	9.2	9.2	1	1

Table 5.24: Orbit points (voltage and current) of the descending I-V characteristic of the $2.5 \mu\text{m}$ RTD.

In this section the excitable response of the $2.5 \mu\text{m}$ RTD was demonstrated for the peak when using a bias voltage of $V_{DC} = 0.87$ V and a pulse with 1 ns of width, in this case the system presents a voltage threshold of 20 mV. For the valley, when using a bias voltage of $V_{DC} = 1.3$ V and a similar disturbance pulse with the difference that it needs to have a negative amplitude the system presented a voltage threshold of 50 mV.

In this section the results obtained using the MatLab Simulink/Simscape simulation and the current voltage characteristics obtained using (Schulman et al. (1996)) model, presented in equation 5.1, were presented. The waveforms of the voltage across the capacitor (that represents the RTD) presented slow-fast transitions and were validated because $\sqrt{\frac{C}{L}} < 0.002$ for all of the RTDs. It was also found that the frequency of oscillation of the voltage across the RTD increases as the capacitance decreases, the capacitance on the other hand, increases with the area of the devices so smaller RTDs present higher frequencies of oscillation. The property of excitability was also observed using the simulation corresponding to the $2.5 \mu\text{m}$ RTD (ascending I-V curve). A voltage threshold of 20 mV was measured when biasing the RTD with $V_{DC} = 0.88$ V and using a pulse of 1 ns. When biasing the RTD in its valley voltage of $V_{DC} = 1.33$ V and using the corresponding descending current voltage characteristic, a voltage treshold of -50 mV was measured for pulse of 1 ns of width.

Chapter 6

Conclusions and Future Work

The objective of this dissertation was to study the neuromorphic properties of circuits based on resonant tunneling diodes (RTDs). It was found that the non-linear nature of its current voltage characteristic makes it a suitable for spike generation in spiking neural networks.

RTDs seem to present better stability when using the peak voltages than when using the valley voltages making them the better choice as operational points.

The valley voltages despite running on less electric power than the peaks, do not present stability with the scaling down of these RTDs provided by the ChipAi project, which is a major drawback for the development of this technology. The peaks as operational points presented promising results such as much lower refractory times, smaller than their period of oscillation, which is an indication that reducing even further the size of the device would present faster communication.

The simulation performed using the current voltage characteristics obtained via curve fit also reproduced what was measured experimentally: the RTDs oscillate when biased in their NDC regions and the properties of the oscillation can be related to the I-V curves and the values of capacitance and inductance, the amplitude and shape of the pulses is related to the orbit points of the I-V curves and the frequency of oscillation is related to the inductance and capacitance of the circuit. Smaller capacitance's i.e. smaller RTDs present higher frequencies of oscillation that are in the same order of magnitude of the ones measured experimentally. The results of the Matlab/Simulink simulation also indicate that the RTD circuits object of study should produce an excitable response to a positive disturbance pulse its peak region and a negative disturbance pulse in its valley region.

With the protocols of characterization that were developed in this dissertation such as the voltage threshold, the bias voltage analysis and the refractory time, one can characterize other circuits based on resonant tunneling diodes but where there is an RTD epilayer incorporating light sensitive layers, which allow its operation as a photodetector with built-gain which can work at much higher rates of communication and modulation this is viable because there is an interesting phenomenon that when one exposes the RTD to radiation the current voltage characteristic shifts, this could be used as the disturbance signal instead of sending electric pulses, a characterization of a circuit that exploits this occurrence would be a great way of continuing the activities that were carried out in this dissertation.

Another future work for this dissertation could consist in investigating other modes of spiking that the RTDs could produce such as bursting. By applying a disturbance pulse with a larger temporal width the RTD could produce more than one spike in that period.

Bibliography

- All-or-none law. All-or-none law/principle. https://en.wikipedia.org/wiki/All-or-none_law. [Online; accessed 1-August-2022].
- Biological Neuron Diagram. Biological Neuron Diagram. <https://www.shutterstock.com/pt/image-illustration/neuron-that-main-part-nervous-system-334761650>. [Online; accessed 19-August-2022].
- M. Bouvier, A. Valentian, T. Mesquida, F. Rummens, M. Reyboz, E. Vianello, and E. Beigne. Spiking neural networks hardware implementations and challenges: A survey. *ACM Journal on Emerging Technologies in Computing Systems (JETC)*, 15(2):1–35, 2019.
- Current transport mechanisms. Current transport mechanisms in the DBQW RTD. <https://www.intechopen.com/chapters/6779>. [Online; accessed 18-August-2022].
- DBQW under bias. Schematic of the band diagram of a DBQW under bias and the corresponding transmission probability. http://web.tiscali.it/decartes/phd_html/node3.html. [Online; accessed 15-August-2022].
- L. Esaki. Long journey into tunneling. *Science*, 183(4130):1149–1155, 1974.
- F. Galluppi, C. Denk, M. C. Meiner, T. C. Stewart, L. A. Plana, C. Eliasmith, S. Furber, and J. Conradt. Event-based neural computing on an autonomous mobile platform. In *2014 IEEE International Conference on Robotics and Automation (ICRA)*, pages 2862–2867. IEEE, 2014.
- S. Ghosh-Dastidar and H. Adeli. Spiking neural networks. *International journal of neural systems*, 19(04):295–308, 2009.
- W. Guo, M. E. Fouda, A. M. Eltawil, and K. N. Salama. Neural coding in spiking neural networks: A comparative study for robust neuromorphic systems. *Frontiers in Neuroscience*, 15:638474, 2021.
- M. Hänggi and L. O. Chua. Cellular neural networks based on resonant tunnelling diodes. *International Journal of Circuit Theory and Applications*, 29(5):487–504, 2001.
- M. Hejda, J. A. Alanis, I. Ortega-Piwonka, J. Lourenço, J. Figueiredo, J. Javaloyes, B. Romeira, and A. Hurtado. Resonant tunnelling diode nano-optoelectronic spiking nodes for neuromorphic information processing. *arXiv preprint arXiv:2107.06721*, 2021.
- S. Herculano-Houzel. Scaling of brain metabolism with a fixed energy budget per neuron: implications for neuronal activity, plasticity and evolution. *PloS one*, 6(3):e17514, 2011.
- G. E. Hinton and R. R. Salakhutdinov. Reducing the dimensionality of data with neural networks. *science*, 313(5786):504–507, 2006.

BIBLIOGRAPHY

- C. Ironside, J. Figueiredo, B. Romeira, T. Slight, L. Wang, and E. Wasige. Resonant tunneling diode-laser diode optoelectronic integrated circuit operating as a voltage controlled oscillator. In *Photonic Materials, Devices, and Applications III*, volume 7366, page 736614. International Society for Optics and Photonics, 2009.
- C. Ironside, B. Romeira, and J. Figueiredo. *Resonant Tunneling Diode Photonics*. IOP Publishing Limited, 2019.
- R. Izumi, S. Suzuki, and M. Asada. 1.98 thz resonant-tunneling-diode oscillator with reduced conduction loss by thick antenna electrode. In *2017 42nd International Conference on Infrared, Millimeter, and Terahertz Waves (IRMMW-THz)*, pages 1–2. IEEE, 2017.
- P. A. Merolla, J. V. Arthur, R. Alvarez-Icaza, A. S. Cassidy, J. Sawada, F. Akopyan, B. L. Jackson, N. Imam, C. Guo, Y. Nakamura, et al. A million spiking-neuron integrated circuit with a scalable communication network and interface. *Science*, 345(6197):668–673, 2014.
- R. A. Nawrocki, R. M. Voyles, and S. E. Shaheen. A mini review of neuromorphic architectures and implementations. *IEEE Transactions on Electron Devices*, 63(10):3819–3829, 2016.
- I. Ortega-Piwonka, O. Piro, J. Figueiredo, B. Romeira, and J. Javaloyes. Bursting and excitability in neuromorphic resonant tunneling diodes. *Physical Review Applied*, 15(3):034017, 2021.
- F. Ponulak and A. Kasinski. Introduction to spiking neural networks: Information processing, learning and applications. *Acta neurobiologiae experimentalis*, 71(4):409–433, 2011.
- J. Schulman, H. De Los Santos, and D. Chow. Physics-based rtd current-voltage equation. *IEEE Electron Device Letters*, 17(5):220–222, 1996.
- K. H. Srivastava, C. M. Holmes, M. Vellema, A. R. Pack, C. P. Elemans, I. Nemenman, and S. J. Sober. Motor control by precisely timed spike patterns. *Proceedings of the National Academy of Sciences*, 114(5):1171–1176, 2017.
- W. Stillwell. —membrane-associated diseases. *An introduction to biological membranes*, pages 499–519, 2016.
- F. Zeldenrust, W. J. Wadman, and B. Englitz. Neural coding with bursts—current state and future perspectives. *Frontiers in computational neuroscience*, 12:48, 2018.
- J. Zhu, T. Zhang, Y. Yang, and R. Huang. A comprehensive review on emerging artificial neuromorphic devices. *Applied Physics Reviews*, 7(1):011312, 2020.

Appendix A

Curve Fitting Results Plots

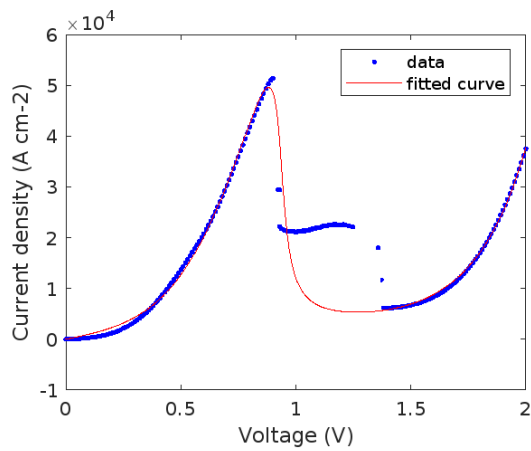


Figure A.1: Plot of the experimental data and curve fit of the $2.5 \mu\text{m}$ radius RTD current voltage curve when increasing forward bias is applied. The curve fitting coefficients are: $A = 1.187 \times 10^4 \text{ A} \cdot \text{cm}^{-2}$; $B = 0.04337 \text{ V}$; $C = 0.1418 \text{ V}$; $D = 0.004704 \text{ V}$; $H = 4.263 \text{ A} \cdot \text{cm}^{-2}$; $n_1 = 0.1515$; $n_2 = 0.1168$.

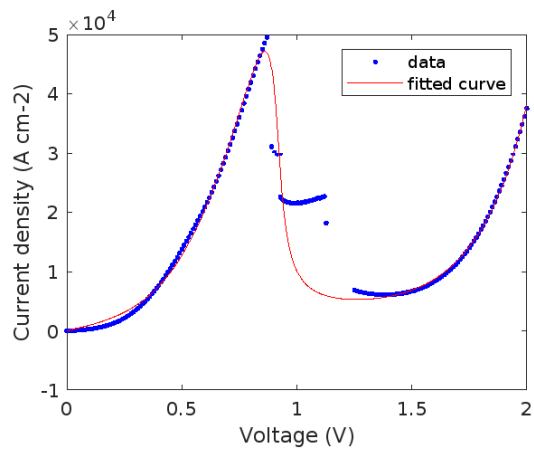


Figure A.2: Plot of the experimental data and curve fit of the $2.5 \mu\text{m}$ radius RTD current voltage curve when decreasing forward bias is applied. The curve fitting coefficients are: $A = 1.161 \times 10^4 \text{ A} \cdot \text{cm}^{-2}$; $B = 0.04263 \text{ V}$; $C = 0.1419 \text{ V}$; $D = 0.005081 \text{ V}$; $H = 3.514 \text{ A} \cdot \text{cm}^{-2}$; $n_1 = 0.155$; $n_2 = 0.1193$.

A. CURVE FITTING RESULTS PLOTS

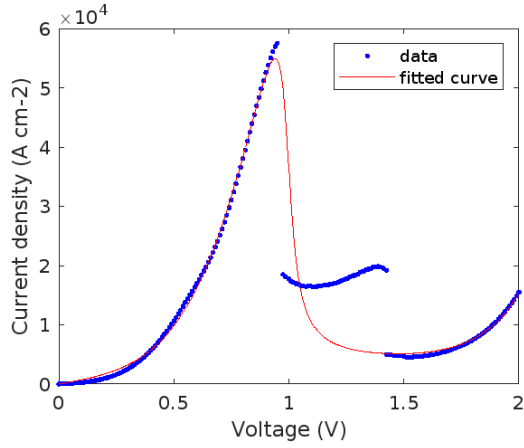


Figure A.3: Plot of the experimental data and curve fit of the $2.5 \mu\text{m}$ radius RTD current voltage curve when increasing reverse bias is applied. The curve fitting coefficients are: $A = 1.538 \times 10^4 \text{ A} \cdot \text{cm}^{-2}$; $B = 0.03642 \text{ V}$; $C = 0.1492 \text{ V}$; $D = 0.00506 \text{ V}$; $H = 0.1277 \text{ A} \cdot \text{cm}^{-2}$; $n_1 = 0.15$; $n_2 = 0.1478$.

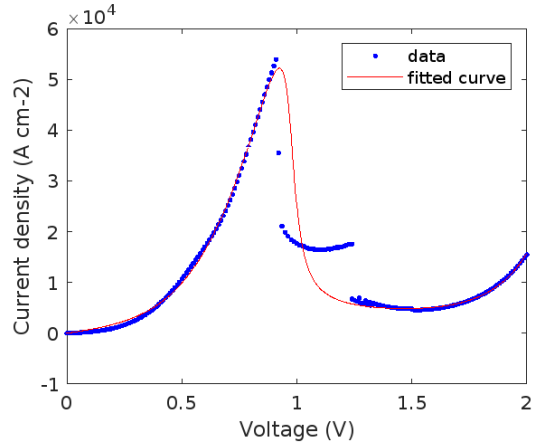


Figure A.4: Plot of the experimental data and curve fit of the $2.5 \mu\text{m}$ radius RTD current voltage curve when decreasing reverse bias is applied. The curve fitting coefficients are: $A = 1.557 \times 10^4 \text{ A} \cdot \text{cm}^{-2}$; $B = 0.03334 \text{ V}$; $C = 0.1461 \text{ V}$; $D = 0.005011 \text{ V}$; $H = 0.05918 \text{ A} \cdot \text{cm}^{-2}$; $n_1 = 0.1495$; $n_2 = 0.1583$.

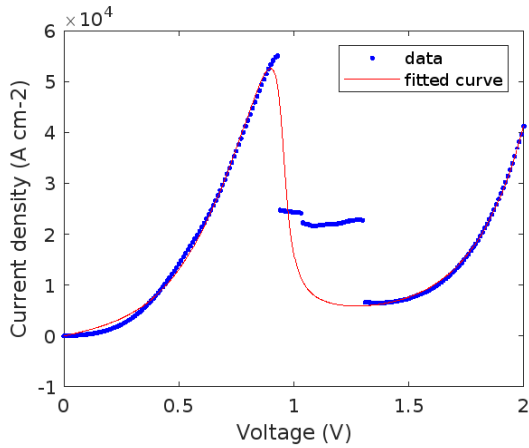


Figure A.5: Plot of the experimental data and curve fit of the $3.5 \mu\text{m}$ radius RTD current voltage curve when increasing forward bias is applied. The curve fitting coefficients are: $A = 1.309 \times 10^4 \text{ A} \cdot \text{cm}^{-2}$; $B = 0.04106 \text{ V}$; $C = 0.1382 \text{ V}$; $D = 0.004566 \text{ V}$; $H = 5.209 \text{ A} \cdot \text{cm}^{-2}$; $n_1 = 0.1448$; $n_2 = 1154$.

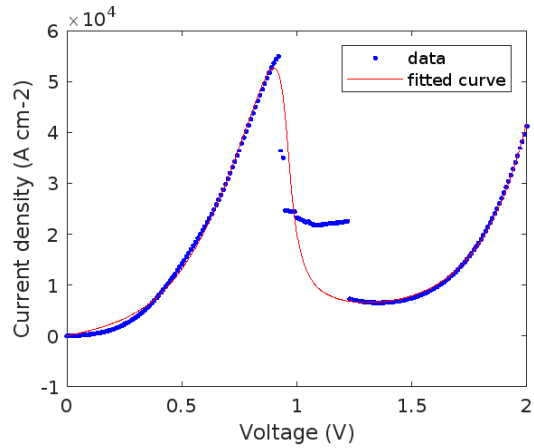


Figure A.6: Plot of the experimental data and curve fit of the $3.5 \mu\text{m}$ radius RTD current voltage curve when decreasing forward bias is applied. The curve fitting coefficients are: $A = 1.284 \times 10^4 \text{ A} \cdot \text{cm}^{-2}$; $B = 0.04379 \text{ V}$; $C = 0.1412 \text{ V}$; $D = 0.005513 \text{ V}$; $H = 3.264 \text{ A} \cdot \text{cm}^{-2}$; $n_1 = 0.1471$; $n_2 = 0.1214$.

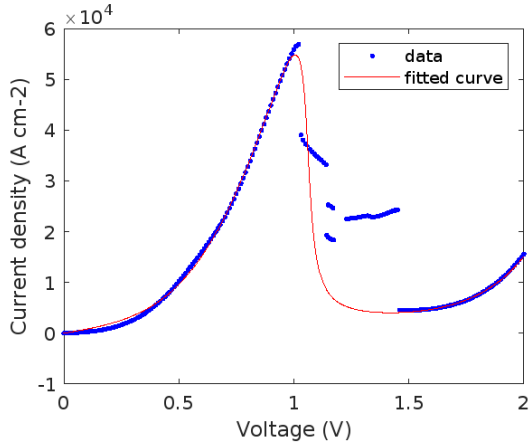


Figure A.7: Plot of the experimental data and curve fit of the $3.5 \mu\text{m}$ radius RTD current voltage curve when increasing reverse bias is applied. The curve fitting coefficients are: $A = 1.133 \times 10^4 \text{ A} \cdot \text{cm}^{-2}$; $B = 0.04902 \text{ V}$; $C = 0.1491 \text{ V}$; $D = 0.003558 \text{ V}$; $H = 1.675 \text{ A} \cdot \text{cm}^{-2}$; $n_1 = 0.1406$; $n_2 = 0.116$.

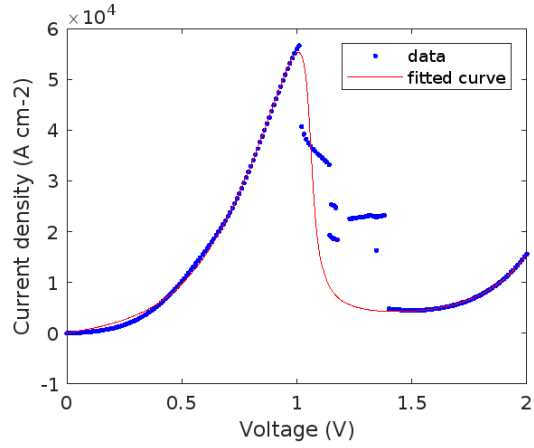


Figure A.8: Plot of the experimental data and curve fit of the $3.5 \mu\text{m}$ radius RTD current voltage curve when decreasing reverse bias is applied. The curve fitting coefficients are: $A = 1.326 \times 10^4 \text{ A} \cdot \text{cm}^{-2}$; $B = 0.04122 \text{ V}$; $C = 0.1425 \text{ V}$; $D = 0.003583 \text{ V}$; $H = 0.9916 \text{ A} \cdot \text{cm}^{-2}$; $n_1 = 0.1344$; $n_2 = 0.1229$.

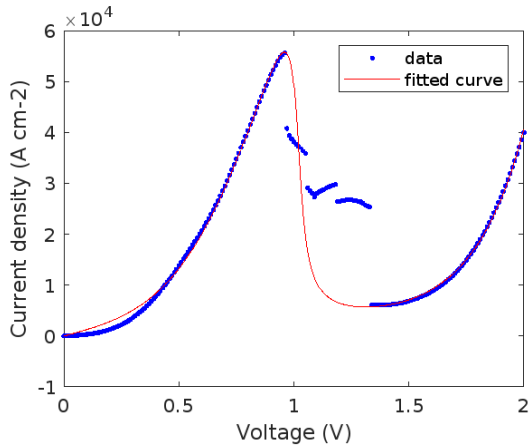


Figure A.9: Plot of the experimental data and curve fit of the $4 \mu\text{m}$ radius RTD current voltage curve when increasing forward bias is applied. The curve fitting coefficients are: $A = 1.171 \times 10^4 \text{ A} \cdot \text{cm}^{-2}$; $B = 0.04873 \text{ V}$; $C = 0.1369 \text{ V}$; $D = 0.003928 \text{ V}$; $H = 4.548 \text{ A} \cdot \text{cm}^{-2}$; $n_1 = 0.1343$; $n_2 = 0.1171$.

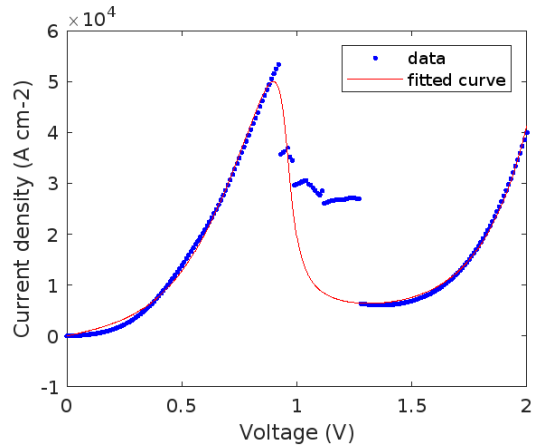


Figure A.10: Plot of the experimental data and curve fit of the $4 \mu\text{m}$ radius RTD current voltage curve when decreasing forward bias is applied. The curve fitting coefficients are: $A = 1.267 \times 10^4 \text{ A} \cdot \text{cm}^{-2}$; $B = 0.04209 \text{ V}$; $C = 0.1387 \text{ V}$; $D = 0.005668 \text{ V}$; $H = 2.296 \text{ A} \cdot \text{cm}^{-2}$; $n_1 = 0.1447$; $n_2 = 0.1257$.

A. CURVE FITTING RESULTS PLOTS

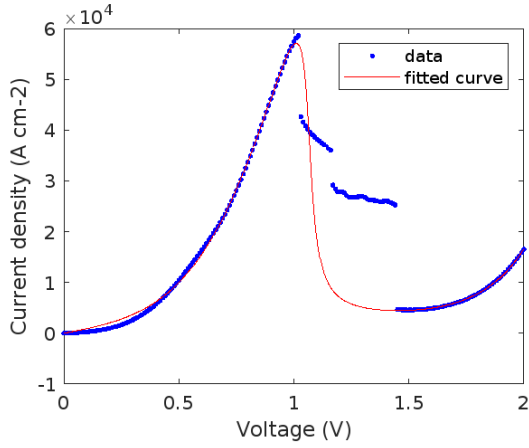


Figure A.11: Plot of the experimental data and curve fit of the $4 \mu\text{m}$ radius RTD current voltage curve when increasing reverse bias is applied. The curve fitting coefficients are: $A = 1.395 \times 10^4 \text{ A} \cdot \text{cm}^{-2}$; $B = 0.04061 \text{ V}$; $C = 0.1417 \text{ V}$; $D = 0.00373 \text{ V}$; $H = 0.4804 \text{ A} \cdot \text{cm}^{-2}$; $n_1 = 0.1329$; $n_2 = 0.1331$.

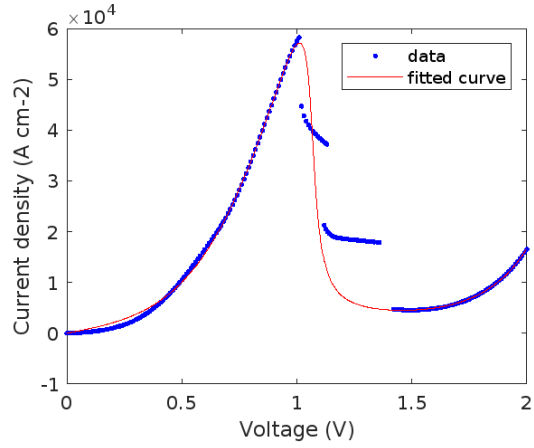


Figure A.12: Plot of the experimental data and curve fit of the $4 \mu\text{m}$ radius RTD current voltage curve when decreasing reverse bias is applied. The curve fitting coefficients are: $A = 1.398 \times 10^4 \text{ A} \cdot \text{cm}^{-2}$; $B = 0.04068 \text{ V}$; $C = 0.1415 \text{ V}$; $D = 0.003798 \text{ V}$; $H = 0.4274 \text{ A} \cdot \text{cm}^{-2}$; $n_1 = 0.1325$; $n_2 = 0.1346$.

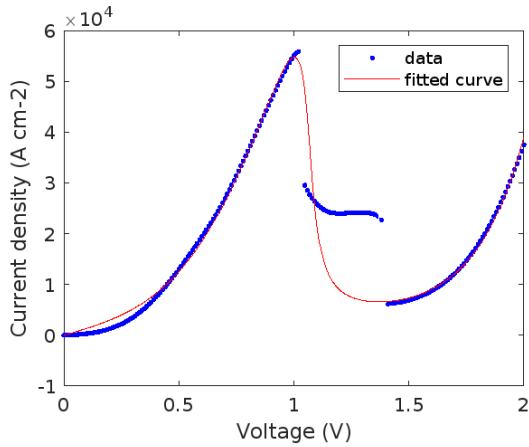


Figure A.13: Plot of the experimental data and curve fit of the $5 \mu\text{m}$ radius RTD current voltage curve when increasing forward bias is applied. The curve fitting coefficients are: $A = 1.323 \times 10^4 \text{ A} \cdot \text{cm}^{-2}$; $B = 0.04193 \text{ V}$; $C = 1281 \text{ V}$; $D = 0.004248 \text{ V}$; $H = 2.297 \text{ A} \cdot \text{cm}^{-2}$; $n_1 = 0.12$; $n_2 = 0.122$.

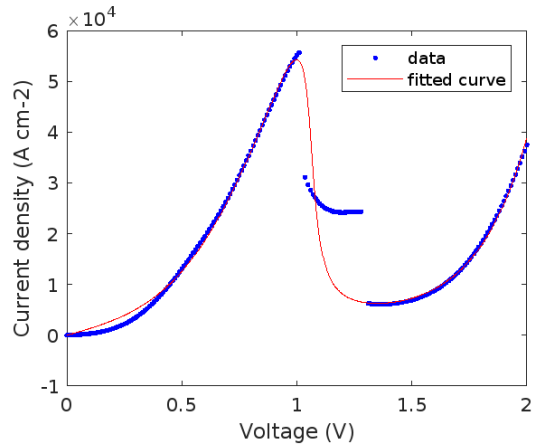


Figure A.14: Plot of the experimental data and curve fit of the $5 \mu\text{m}$ radius RTD current voltage curve when decreasing forward bias is applied. The curve fitting coefficients are: $A = 1.165 \times 10^4 \text{ A} \cdot \text{cm}^{-2}$; $B = 0.04776 \text{ V}$; $C = 0.1322 \text{ V}$; $D = 0.004076 \text{ V}$; $H = 4.577 \text{ A} \cdot \text{cm}^{-2}$; $n_1 = 0.1244$; $n_2 = 0.1163$.

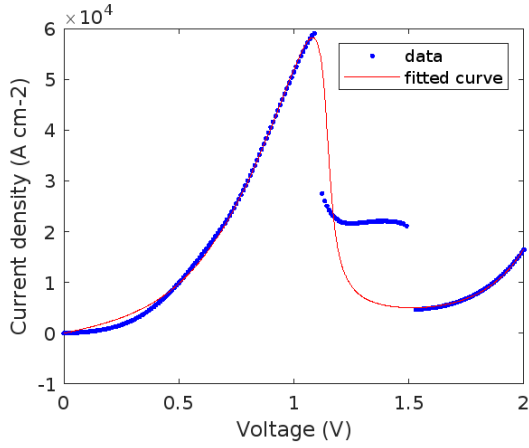


Figure A.15: Plot of the experimental data and curve fit of the $5 \mu\text{m}$ radius RTD current voltage curve when increasing reverse bias is applied. The curve fitting coefficients are: $A = 1.437 \times 10^4 \text{ A} \cdot \text{cm}^{-2}$; $B = 0.04014 \text{ V}$; $C = 0.1351 \text{ V}$; $D = 0.003739 \text{ V}$; $H = 0.2883 \text{ A} \cdot \text{cm}^{-2}$; $n_1 = 0.118$; $n_2 = 0.1395$.

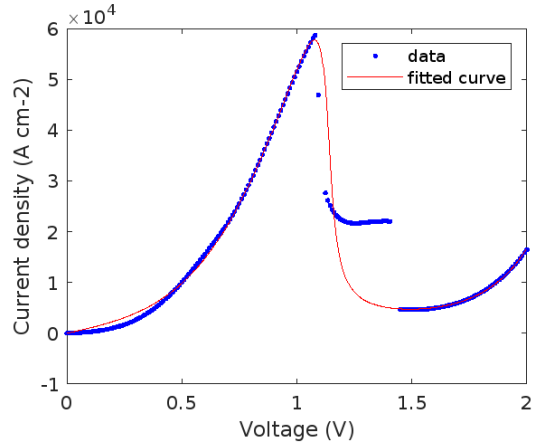


Figure A.16: Plot of the experimental data and curve fit of the $5 \mu\text{m}$ radius RTD current voltage curve when decreasing reverse bias is applied. The curve fitting coefficients are: $A = 1.384 \times 10^4 \text{ A} \cdot \text{cm}^{-2}$; $B = 0.041 \text{ V}$; $C = 0.1351 \text{ V}$; $D = 0.003463 \text{ V}$; $H = 0.5037 \text{ A} \cdot \text{cm}^{-2}$; $n_1 = 0.1187$; $n_2 = 0.1326$.

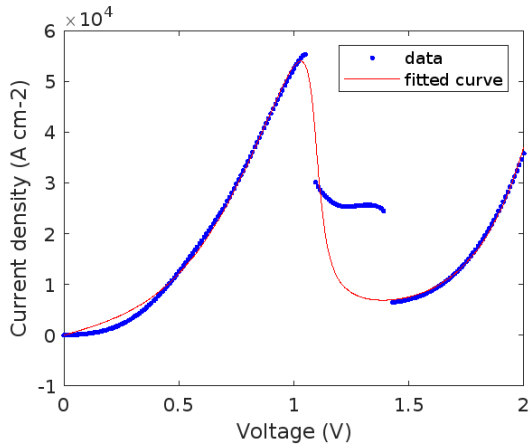


Figure A.17: Plot of the experimental data and curve fit of the $5.5 \mu\text{m}$ radius RTD current voltage curve when increasing forward bias is applied. The curve fitting coefficients are: $A = 1.238 \times 10^4 \text{ A} \cdot \text{cm}^{-2}$; $B = 0.04457 \text{ V}$; $C = 0.1278 \text{ V}$; $D = 0.004241 \text{ V}$; $H = 4.081 \text{ A} \cdot \text{cm}^{-2}$; $n_1 = 0.1164$; $n_2 = 0.117$.

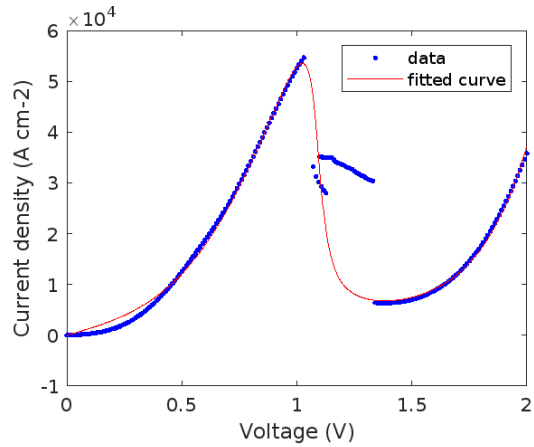


Figure A.18: Plot of the experimental data and curve fit of the $5.5 \mu\text{m}$ radius RTD current voltage curve when decreasing forward bias is applied. The curve fitting coefficients are: $A = 1.228 \times 10^4 \text{ A} \cdot \text{cm}^{-2}$; $B = 0.04459 \text{ V}$; $C = 0.1283 \text{ V}$; $D = 0.004258 \text{ V}$; $H = 3.968 \text{ A} \cdot \text{cm}^{-2}$; $n_1 = 0.1176$; $n_2 = 0.1175$.

A. CURVE FITTING RESULTS PLOTS

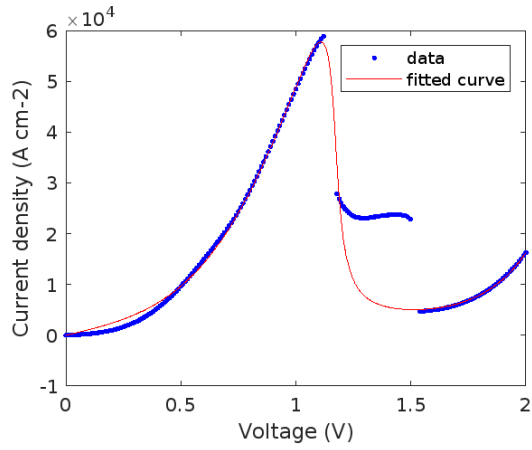


Figure A.19: Plot of the experimental data and curve fit of the $5.5 \mu\text{m}$ radius RTD current voltage curve when increasing reverse bias is applied. The curve fitting coefficients are: $A = 1.438 \times 10^4 \text{ A} \cdot \text{cm}^{-2}$; $B = 0.0389 \text{ V}$; $C = 0.1311 \text{ V}$; $D = 0.003384 \text{ V}$; $H = 0.6433 \text{ A} \cdot \text{cm}^{-2}$; $n_1 = 0.112$; $n_2 = 0.129$.

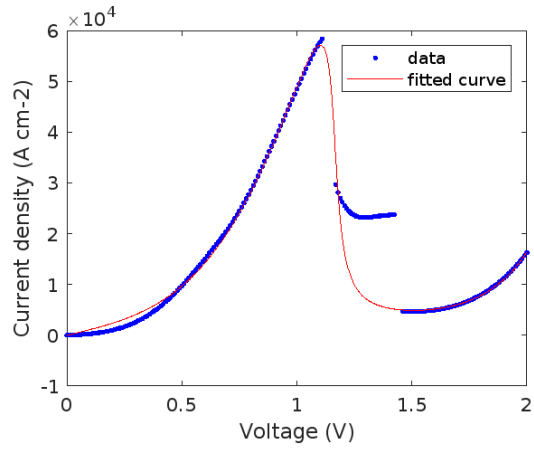


Figure A.20: Plot of the experimental data and curve fit of the $5.5 \mu\text{m}$ radius RTD current voltage curve when decreasing reverse bias is applied. The curve fitting coefficients are: $A = 1.467 \times 10^4 \text{ A} \cdot \text{cm}^{-2}$; $B = 0.03721 \text{ V}$; $C = 0.1297 \text{ V}$; $D = 0.003309 \text{ V}$; $H = 0.5417 \text{ A} \cdot \text{cm}^{-2}$; $n_1 = 0.1114$; $n_2 = 0.1314$.

Appendix B

Curve Fitting Model Peak and Valley Currents and Voltages

RTD Radius (μm)	$I_{Peak}(mA)$	$I_{Valley}(mA)$	PVCR	$V_{Peak}(V)$	V_{Valley}	Difference
forward Bias Ascend						
2.5	9.85	1.05	9.27	0.88	1.27	0.39
3.5	20.22	2.27	8.91	0.9	1.27	0.37
4	28.02	2.87	9.76	0.96	1.31	0.35
4.5	34.9	4.07	8.57	0.98	1.35	0.37
5	42.96	5.17	8.30	1	1.36	0.36
5.5	51.28	6.56	7.81	1.03	1.38	0.35
reverse Bias Ascend						
2.5	10.79	1.00	10.79	0.94	1.47	0.53
3.5	21.08	1.55	13.6	1.01	1.42	0.41
4	28.68	2.24	12.8	1.01	1.45	0.44
4.5	36.72	2.9	12.32	1.05	1.48	0.43
5	45.71	3.95	11.57	1.08	1.51	0.43
5.5	54.85	4.80	11.43	1.10	1.51	0.41
forward Bias Descend						
2.5	9.25	1.04	8.89	0.86	1.26	0.4
3.5	20.23	2.53	8	0.9	1.31	0.41
4	25.11	3.22	7.8	0.9	1.31	0.41
4.5	34.07	3.68	9.26	0.96	1.31	0.35
5	42.56	4.93	8.63	1	1.35	0.35
5.5	50.83	6.45	7.88	1.02	1.38	0.36
reverse Bias Descend						
2.5	10.24	0.95	10.77	0.92	1.47	0.55
3.5	21.26	1.64	12.96	1.01	1.43	0.42
4	28.69	2.27	12.64	1.01	1.46	0.45
4.5	36.72	2.95	12.45	1.04	1.47	0.43
5	45.33	3.72	12.19	1.08	1.49	0.41
5.5	54.23	4.65	11.66	1.10	1.51	0.41

Table B.1: Peak/valley currents and voltages obtained for each of the RTDs for the I-V curve obtained via curve fitting algorithm.

Appendix C

VCO Waveforms

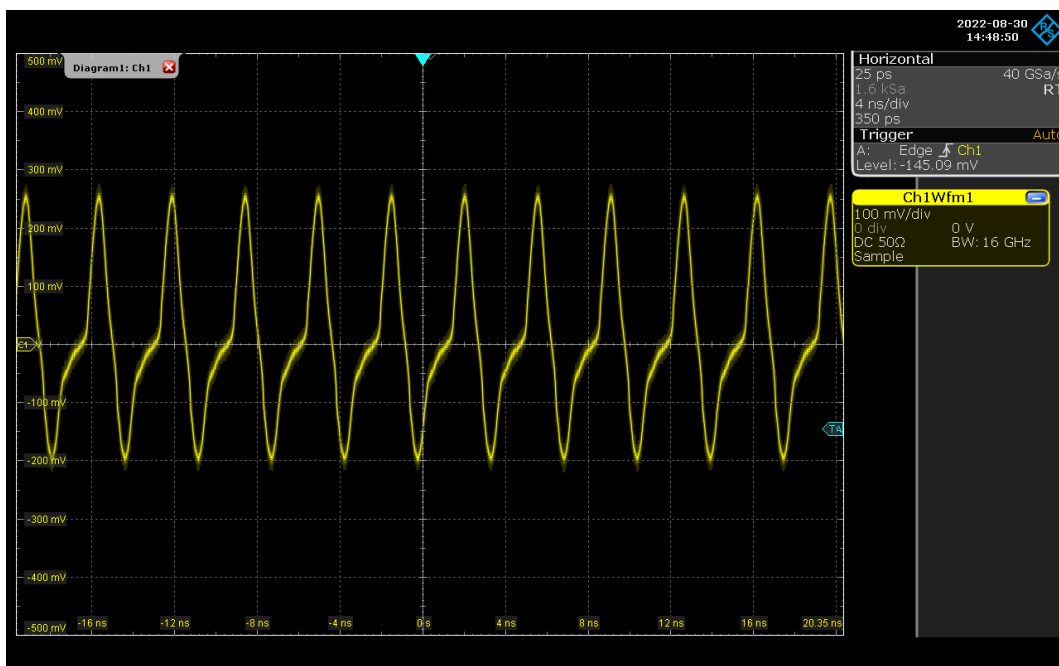


Figure C.1: Waveform of the 2.5 μm RTD under a 0.96 V bias voltage.

C. WAVEFORMS

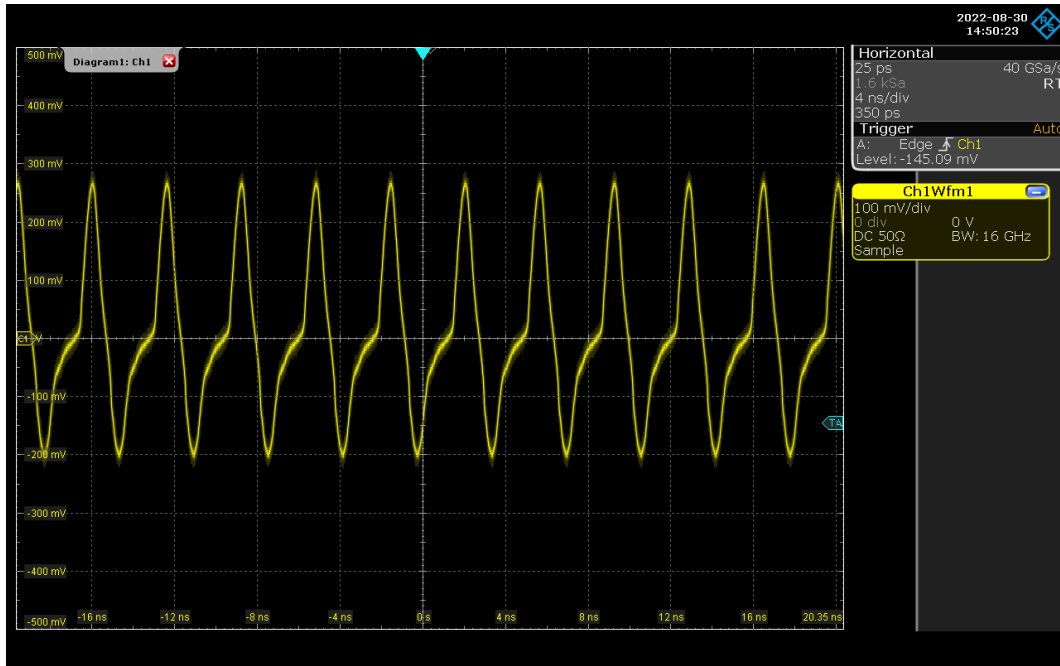


Figure C.2: Waveform of the 3.5 μm RTD under a 0.96 V bias voltage.

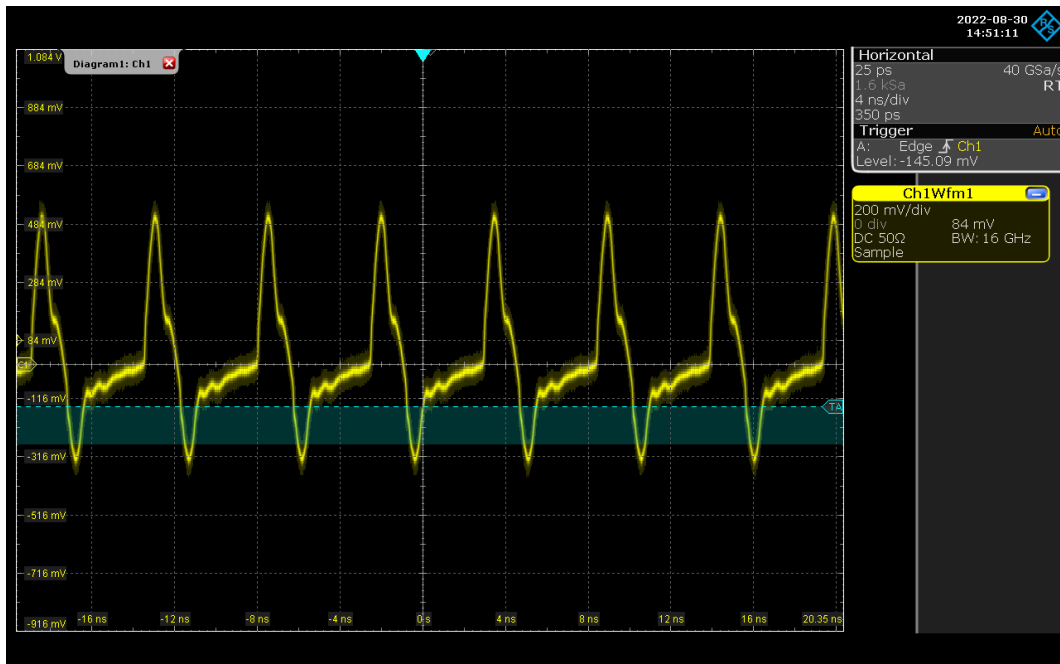


Figure C.3: Waveform of the 4 μm RTD under a 1.04 V bias voltage.

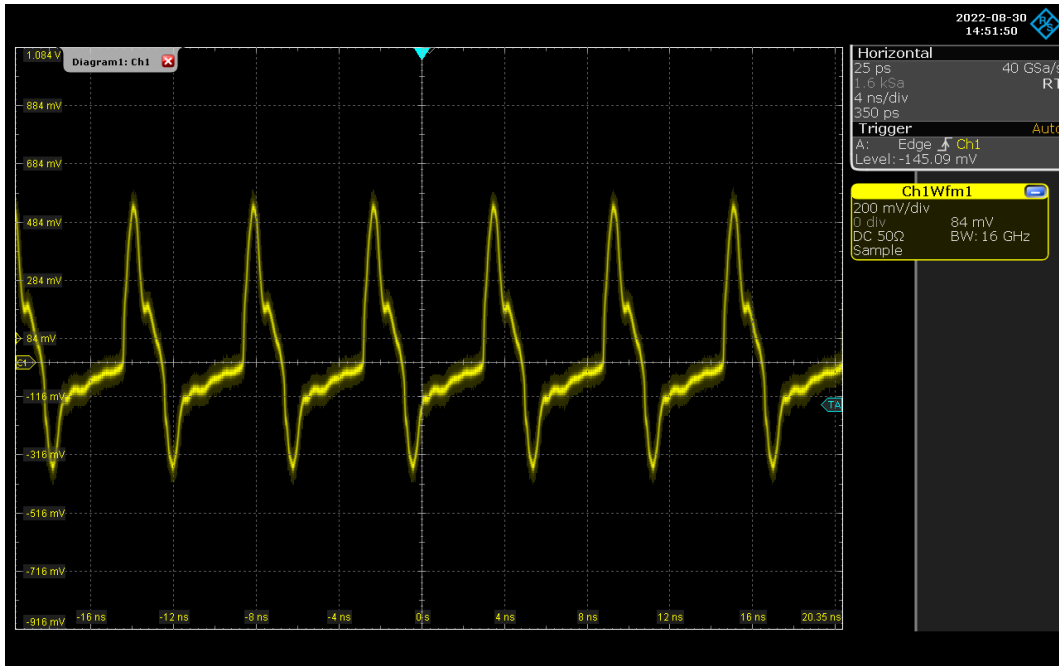


Figure C.4: Waveform of the 4.5 μm RTD under a 1.12 V bias voltage.

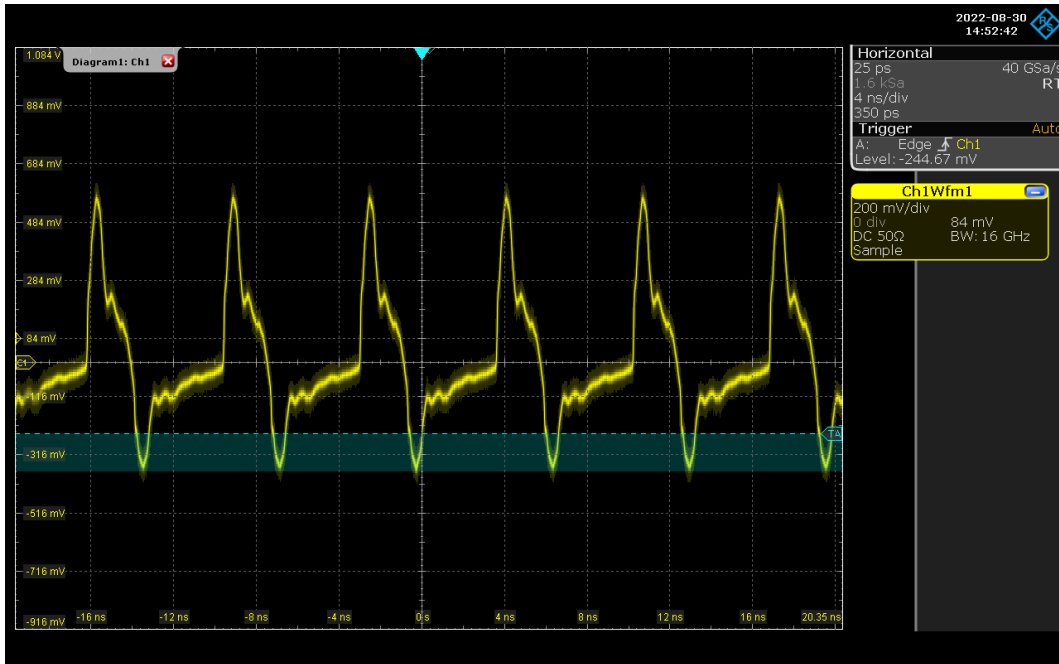


Figure C.5: Waveform of the 5 μm RTD under a 1.13 V bias voltage.

C. WAVEFORMS

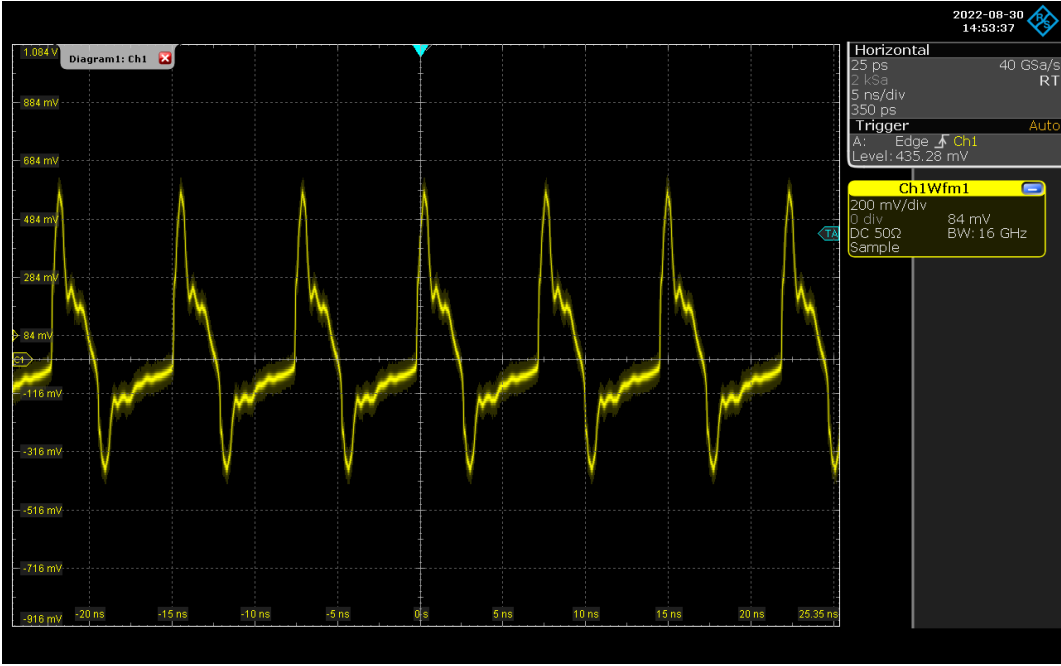


Figure C.6: Waveform of the 5.5 μm RTD under a 1.19 V bias voltage.

Appendix D

Spiking

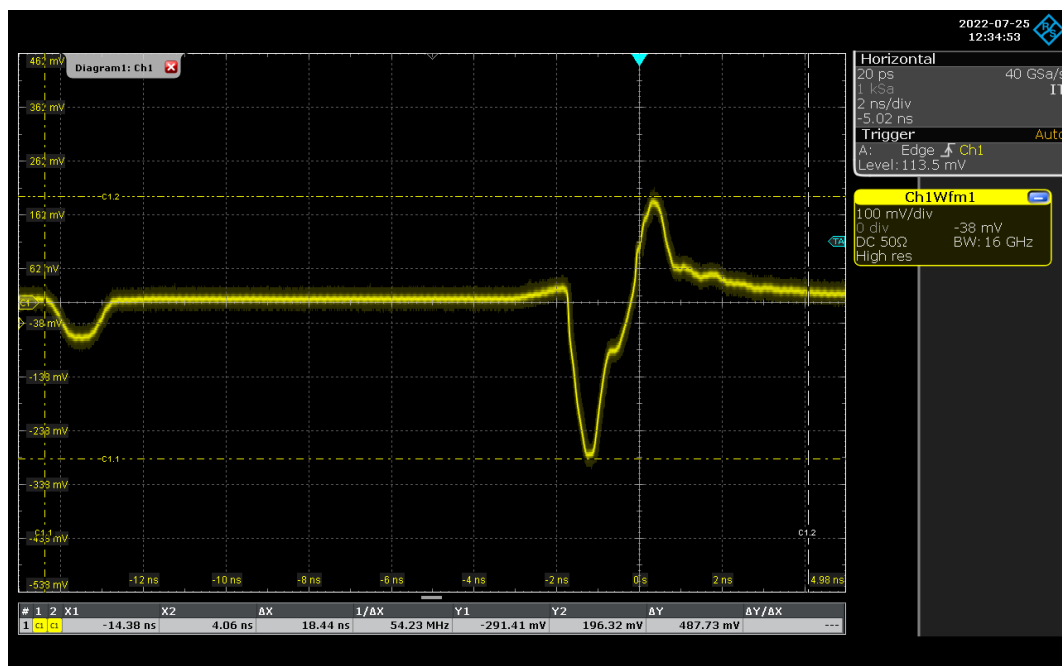


Figure D.1: Oscilloscope trace for the generated spike of the $4.5 \mu\text{m}$ RTD, when disturbed in its reverse peak voltage. The bias voltage was of -1.028 V and the pulse amplitude was of -75 mV and 1 ns width.

D. SPIKING



Figure D.2: Oscilloscope trace for the generated spike of the $4.5 \mu\text{m}$ RTD, when disturbed in its reverse valley voltage. The bias voltage was of -1.52 V and the pulse amplitude was of 350 mV and 1 ns width.